Optimisation of image reconstruction for Talbot-Lau x-ray phase-contrast imaging with regard to mechanical robustness

Masterarbeit aus der Physik

Vorgelegt von

Maria Seifert

25. Mai 2016

Erlangen Centre for Astroparticle Physics
Physikalisches Institut IV
Friedrich-Alexander-Universität Erlangen-Nürnberg

Betreuerin: Prof. Dr. Gisela Anton

Abstract

X-ray grating-based phase-contrast imaging opens new opportunities, inter alia, in medical imaging and non-destructive testing. This is due to the fact that information about the attenuation properties and about the refractive properties of an object are gained simultaneously. Thus, three different images can be achieved in one imaging process: the attenuation image showing the absorption properties of an object, the differential phase-contrast image showing edges in the object and the dark-field image showing the scattering properties of the object.
Talbot-Lau imaging requires the knowledge of a reference or free-field image. The long-term stability of a Talbot-Lau interferometer is related to the time span of the validity of a measured reference image. However, for example thermal and other long-term external influences result in drifting effects of the phase images. It is necessary to take reference/free-field images for calculating the differential phase-contrast image of an object. As the phases are shifting over time and the reference image is not valid for long-term measurements, artifacts occur in differential phase-contrast images. Due to the relatively small size of available gratings large images have to be scanned by multiple of partial images. This leads to long acquisition times for a whole image of an object. Thus, it is desirable to keep the validity of the reference image for such time scales. Even if the gratings are larger it would be advantageous to take a reference image just once a day or even once a week.
Firstly, in this thesis some efforts are shown to describe the phase-shift with the help of the temperature change of the gratings during the measurement.
Secondly, an algorithm is presented to determine the differential phase-contrast image with the help of just one calibration image, which is valid for a long time-period. With the help of this algorithm it is possible to save measurement-time, as it is not necessary to take a reference image for each measurement.
A further problem in Talbot-Lau imaging is the short-term stability of the setup. Transferring the interferometer technique from laboratory setups to conventional imaging systems the necessary rigidity of the system is difficult to achieve. Therefore, short-term effects like vibrations or distortions of the system lead to imperfections within the phase-stepping procedure. Given insufficient stability of the phase-step positions, up to now, artifacts in phase-contrast images occur, which lower the image quality. This is a problem with regard to the intended use of phase-contrast imaging for example in clinical routine or non-destructive testing.
In this thesis an algorithm used in the optics is applied to correct inaccurate phase-step positions with the help of a principal component analysis (PCA). Thus, it is possible to calculate the artifact-free differential phase-contrast image, dark-field

image and attenuation image.
Finally, this algorithm is tested with regard to image objects with large differences in absorption capacity.

Contents

Chapter 1

Introduction

In conventional x-ray imaging the attenuation image of an object is acquired, which implies a good bone-tissue contrast with regard to medical imaging. Thus, today x-ray imaging plays an essential role in medical diagnosis. Nevertheless, soft tissue contrast is hard to achieve with the help of conventional x-ray imaging. Zernike [61] proposed a method for optical experiments to get further information about an object in the beam path by observing the phase-shift caused by the object. Lohmann and Silva [34] used the optical Talbot-Lau effect to get the phase information of an object using a polychromatic light source. In the last years a new imaging technique based on this idea has been applied to x-ray imaging, the so called Talbot-Lau interferometry [19]. Using a Talbot-Lau interferometer [10, 19, 28, 32, 42, 45, 49, 50] further information about the phase-shift and the scattering properties of the object can be obtained simultaneously [33]. For this, three different imaging modalities can be gained during one imaging process:

- the conventional attenuation image: showing a good bone-tissue contrast,
- the differential phase-contrast image: emphasizing edges in the image, and
- the dark-field image: showing the scattering properties of an object and therefore depicting subpixeled structures.

Thus, in addition to the good bone-tissue contrast of the conventionally taken x-ray image a better soft tissue contrast is gained. Therefore, this technique is a very promising imaging modality in medical imaging [11, 23, 33, 38, 39, 45, 48] and non-destructive testing [45].
For example, it is possible to image micro calcifications in mammography [38, 48] and to depict lung tissue [11]. This might give the opportunity to diagnose breast tumors [38, 48] and lung diseases like emphysema [11] earlier.

However, the x-ray phase-contrast setup is sensitive to vibrations, thermal effects and mechanical inaccuracies of the grating positions [29,51]. These impacts can be differentiated on three time scales:

1. very short-term is the exposure time at a single phase-step position,
2. short-term is the time needed to acquire a phase-stepping curve, and
3. long-term is more than that.

Talbot-Lau imaging requires the knowledge of a reference or free-field image. Mainly the reference phase image is sensitive to the above mentioned impacts resulting in drift effects. The long-term stability of a Talbot-Lau interferometer is thus related to the time span of the validity of a measured reference image. Due to the relatively small size of available gratings large object have to be scanned by a multiple of partial images. The time needed to image, for instance, a human knee may lie in the order of hours. Accordingly, it is desirable to keep the validity of a reference image for at least a complete long-term measurement. It is expected that with large gratings the acquisition time will go down to seconds. But for clinical routine it would be desirable that one reference image is valid for a long term period like a day or a week. Especially, e.g. in fluoroscopy, the short validity of a reference image poses many problems as there is not enough time to take the required amount of reference images.
In this thesis, firstly, some efforts are shown to describe the phase-shift with the help of the temperature change of the gratings during the measurement. Secondly, an image reconstruction algorithm, subsequently called Phase-Plane-Fit (PPF) Method, is presented that provides the opportunity to reconstruct a phase-contrast image using just one reference image. Using the PPF method the influence of drifting effects on the phase image can be reduced or even removed. Thus, the setup has not to be recalibrated continuously. This is better compatible with clinical workflow as the image acquisition procedure becomes the same as in conventional x-ray imaging. The images gained in Talbot-Lau interferometry are usually reconstructed by Fourier-Analysis (FFT) [20] or least square fitting routine of the phase-stepping dataset. For both methods it is necessary to know the exact phase-step positions. These are well known for the interferometer mounted on a laboratory optical table. Transferring the technique to a conventional imaging system, vibrations and distortions during the acquisition procedure lead to artifacts in the obtained images if the conventional reconstruction methods are applied. To retrieve the information from unknown phase-step positions Vargas et.al. [53] proposed an algorithm based on principal component analysis (PCA) for optical light interferometry. This method was recently transferred to x-ray phase-imaging by Pelzer et.al. [43]. So far, only the reconstruction of the differential phase-contrast image was achieved with the help of the PCA

algorithm. In this work an advanced algorithm of Vargas et al. [54] is used to obtain the accurate phase-step positions and - combined with standard sine fit reconstruction - to obtain the attenuation and dark-field images as well. Finally, this algorithm is tested with regard to imaging thick, high absorbing objects like human knees.

Chapter 2

Physical fundamentals

In this chapter an overview about the fundamentals of x-ray imaging is given. In the first part of this chapter the generation of x-rays is explained. Thereafter, the mathematical background of propagation of x-rays is shortly mentioned. At the end of this chapter, the different interaction processes of x-rays with matter are shown.

2.1 Generation of x-rays

2.1.1 Basics of x-radiation

In November 1895 Wilhem-Conrad Röntgen discovered that it is possible to picture internal, internal structures of an object on behalf of the later called x-rays. In 1901 he got the first Nobel Prize in physics for his discovery [3].
X-rays used for typical diagnostic applications are electromagnetic waves with an energy between 20 keV and 150 keV [14]. In figure 2.1 the electromagnetic spectrum is shown. In figure 2.2 the different possibilities to use electromagnetic waves in medicine depending on the wavelength/the energy are shown.

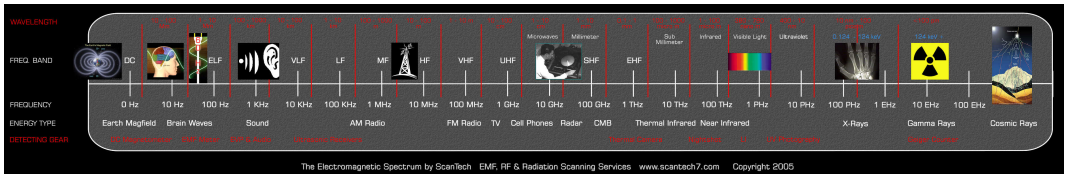

Figure 2.1: The electromagnetic spectrum. [2]

The generation of x-rays is due to several physical processes. The first process is the generation of electromagnetic waves because of the deceleration of an electron beam by an atom, called bremsstrahlung. The second process is the generation

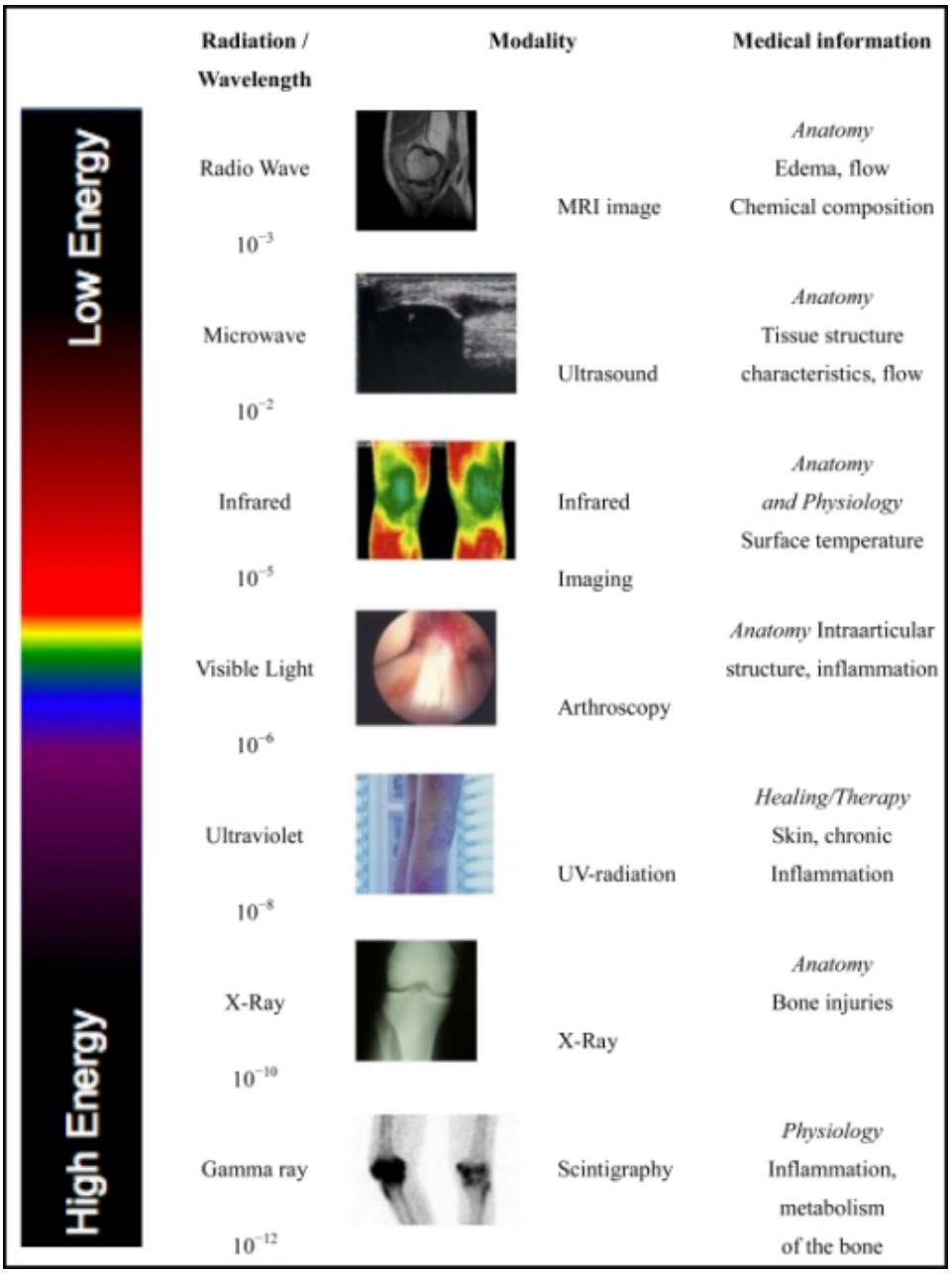

Figure 2.2: The electromagnetic spectrum with regard to medical use. [6]

of electromagnetic waves due to a relaxation process of an atom which has been excited by an electron, called characteristic radiation. In figure 2.3 the schematic spectrum of a x-ray tube is shown. The continuous part of the spectrum is caused by the bremsstrahlung whereas the peaks are caused by the characteristic radiation.

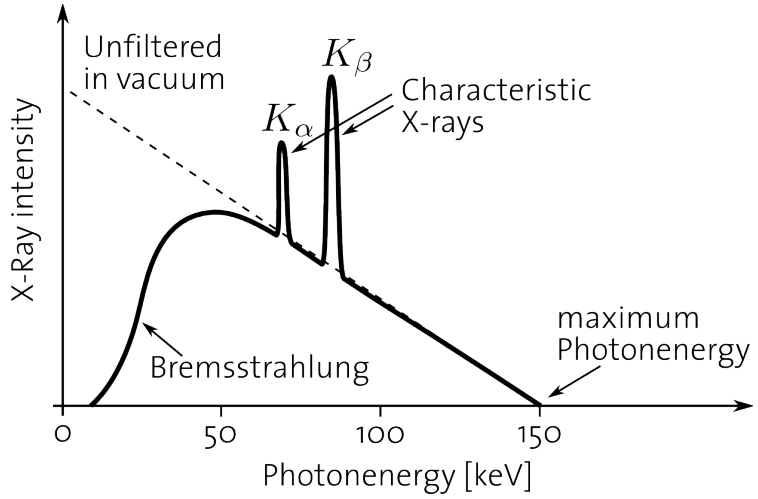

Figure 2.3: Schematic representation of the spectrum of an x-ray tube. [17]

2.1.2 Bremsstrahlung

An electron with a kinetic energy E_{kin1} which enters the Coulomb field of an atom is accelerated by the inelastic interaction of the Coulomb fields of the electron itself and the atom. Thus, it emits one part of its kinetic energy as a photon with an energy of $E_{\text{ph}} = h\nu$. After this interaction the scattered electron has a kinetic energy of $E_{\text{kin2}} = E_{\text{kin1}} - E_{\text{ph}}$ left [7, 14, 21]. Figure 2.4 schematically shows the generation of bremsstrahlung.

The emitted energy per path length can be calculated as following [7]:

$$-\frac{\mathrm{d}E_{\text{kin1}}}{\mathrm{d}x} = 4\alpha \mathrm{N_A} \frac{Z^2}{A} z^2 \left(\frac{1}{4\pi\epsilon_0} \frac{\mathrm{e}^2}{m\mathrm{c}^2}\right) E_{\text{kin1}} \ln\left(\frac{183}{Z^{\frac{1}{3}}}\right). \tag{2.1}$$

Thereby Z and A are the valency and the mass number of the atom. E_{kin1}, z and m are the energy, the electrical charge and the mass of the incoming electron. α, $\mathrm{N_A}$ and ϵ_0 are the finestructur constant, Avogadro constant and the dielectric constant of the vacuum.
The energy of the emitted photons correspond to a continuous spectrum (figure 2.5).

The ratio of the energy loss of the electron by production of bremsstrahlung and the energy loss by excitation and ionization of the atom can be calculated as following

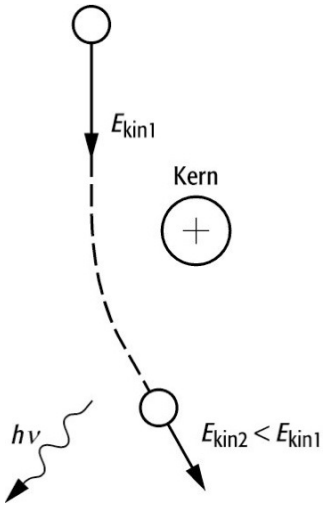

Figure 2.4: Schematic representation of the deceleration of an electron in the Coulomb field of an atom and of the emission of bremsstrahlung. [7]

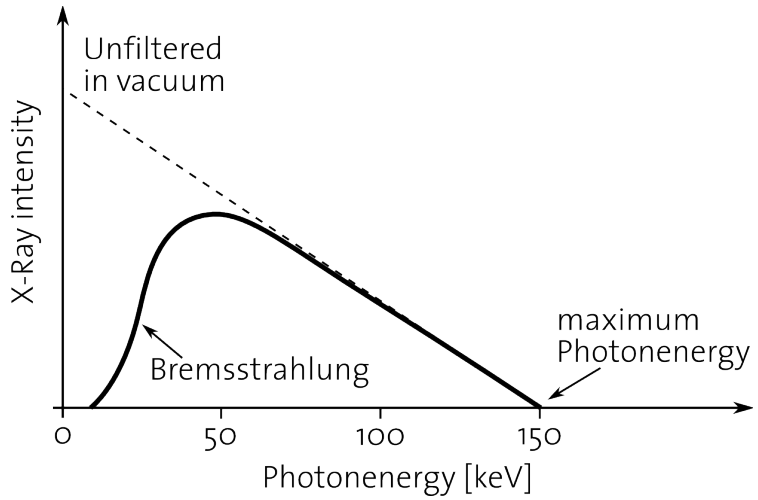

Figure 2.5: Schematic representation of the spectrum of the bremstrahlung. [18]

[14]:

$$\frac{\text{Bremsstrahlung}}{\text{Excitation and Ionization}} = \frac{E_{\text{kin1}} Z}{820}. \tag{2.2}$$

In this equation E_{kin1} is again the energy of the incident electron in MeV and Z is the atomic number of the interacting atom.

2.1.3 Characteristic radiation

Characteristic radiation is due to a relaxation process within the atom. In figure 2.6 a schematic representation of the generation of characteristic radiation is shown. An orbital electron of an inner orbit of the atom is removed for example by an incoming electron which is scattered by the interaction process. The missing electron is replaced by an electron of an orbit further away from the atomic nucleus than the orbit with the missing electron. As the binding energy of the electron is stronger near the nucleus energy is released in form of a photon by the electron which changes the orbit. The energy of the released photon corresponds to the energy difference between the orbit the electron originates from and the orbit the electron is moving to. The potentials of the different orbits are characteristic for the material. Thus, the potential differences are dependent on the material and therefore the energy of the emitted photon is characteristic of the material. The energy peaks are called with the letter of the inner orbit the electron is moving to. Thus, there occurs for example K- or L-radiation. Small Greek letters starting with α, β and so on describe the number of orbits the electron is moving. If the electron which is changing originates from an orbit just one orbit above the destination orbit (here orbit K) the radiation peak is called for example K_α. If it originates from an orbit two orbits above the destination orbit the radiation peak is called K_β and so on. [14, 21]

2.1.4 Functioning of a x-ray tube

The effects explained above are used to produce x-radiation. To get the electrons hitting the target a filament is heated. Due to the thermoelectric effect electrons are emitted by the filament. They are accelerated towards an anode which is made out of the target material. Within the target material x-radiation is produced due to the effects explained above. Between the filament and the anode the electron beam is focused by electrodes. The whole tube has to be cooled as much energy is lost in the form of heat. Figure 2.7 shows the principle components of a conventional x-ray tube.

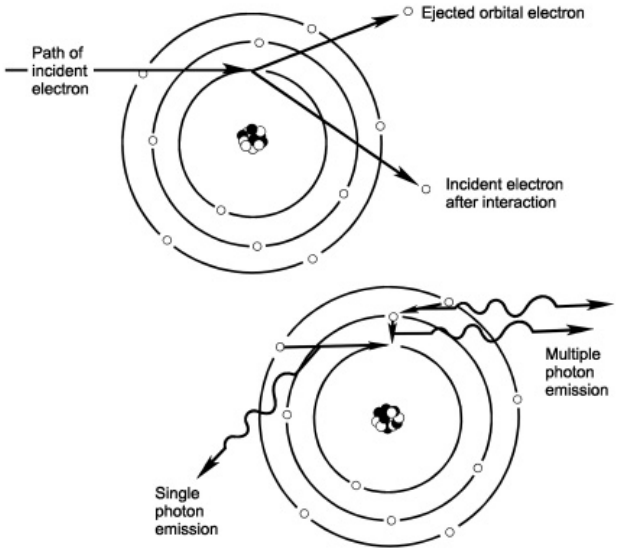

Figure 2.6: Schematic representation of the generation of characteristic radiation. [5]

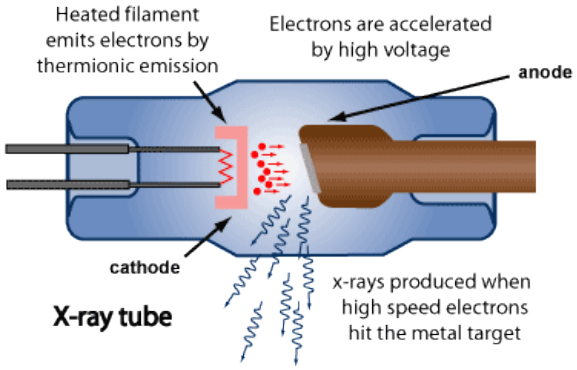

Figure 2.7: Functioning of a x-ray tube. [1]

2.2 Propagation of x-rays

The following derivations and explanations can be for example looked up in Born and Wolf [13], Kopitzki and Herzog [30], Griffith [25], Hecht [27] or Meschede [37].

Like for all electromagnetic waves, the propagation of x-rays can be explained with the help of the four Maxwell equations in matter:

$$\vec{\nabla}\vec{D}(\vec{r},t) = \rho(\vec{r},t), \tag{2.3}$$

$$\vec{\nabla}\vec{B}(\vec{r},t) = 0, \tag{2.4}$$

$$\vec{\nabla} \times \vec{E}(\vec{r},t) = -\frac{\partial}{\partial t}\vec{B}(\vec{r},t), \tag{2.5}$$

$$\vec{\nabla} \times \vec{H}(\vec{r},t) = \vec{j}(\vec{r},t) + \frac{\partial}{\partial t}\vec{D}(\vec{r},t), \tag{2.6}$$

whereas $\vec{D}$ is the electric flux density, $\vec{B}$ is the magnetic flux density, $\vec{E}$ is the electric field strength, $\vec{H}$ is the magnetic field strength, ρ is the charge density and $\vec{j}$ is the electric current density.
For isotropic matter without free currents ($\vec{j}(\vec{r},t) = 0$) and charges ($\rho(\vec{r},t) = 0$) holds:

$$\vec{D}(\vec{r},t) = \epsilon_0\epsilon_r\vec{E}(\vec{r},t) \tag{2.7}$$

and

$$\vec{B}(\vec{r},t) = \mu_0\mu_r\vec{H}(\vec{r},t) \tag{2.8}$$

with the dielectric constant ϵ_0, the relative permittivity of the material ϵ_r, the magnetic constant μ_0 and the relative permeability of the material μ_r. The speed of light in vacuum c_0 can be calculated as following:

$$c_0 = \frac{1}{\sqrt{\epsilon_0\mu_0}}. \tag{2.9}$$

For matter respectively holds:

$$c_{\text{matter}} = \frac{1}{\sqrt{\epsilon_0 \epsilon_r \mu_0 \mu_r}} = \frac{c_0}{\sqrt{\epsilon_r \mu_r}} = \frac{c_0}{n} \tag{2.10}$$

with $n = \sqrt{\epsilon_r \mu_r}$ being the refractive index of the matter. For non magnetic matter it can be assumed that $\mu_r \approx 1$. With the help of the Lorentz oscillator model it can be derived:

$$\epsilon_r(\omega) = 1 + \frac{\mathrm{e}^2 \rho_e}{\epsilon_0 m_\mathrm{e}} \frac{1}{\omega_0^2 - \frac{\mathrm{e}^2 \rho_\mathrm{e}}{3\epsilon_0 m_\mathrm{e}} - \omega^2 - \mathrm{i}\gamma\omega}. \tag{2.11}$$

There, m_e is the mass of an electron, e is the charge of an electron, ρ_e is the electron density, ω_0 is the natural frequency of the system and γ is the damping coefficient of the system. ω describes the angular frequency. For x-rays the second term ϵ' of $\epsilon_r = 1 + \epsilon'$ is much smaller than 1: $|\epsilon'| \ll 1$. Additionally, it can be assumed that $\omega^2 \gg \omega_0^2 - \frac{e^2 \rho_\mathrm{e}}{3\epsilon_0 m_\mathrm{e}}$. After performing a Taylor series and rounding the result because of the assumption for ω the refractive index can be calculated as:

$$n(\omega) = 1 - \delta_\omega + \mathrm{i}\beta_\omega \tag{2.12}$$

with $\delta_\omega = \frac{e^2 \rho_e}{2\epsilon_0 m_e} \frac{\omega^2}{\omega^4 + \gamma^2 \omega^2}$ and $\beta_\omega = \frac{e^2 \rho_e}{2\epsilon_0 m_e} \frac{\gamma\omega}{\omega^4 + \gamma^2 \omega^2}$.

With the equations 2.3 to 2.8 and the assumptions of $\vec{j}(\vec{r}, t) = 0$ and $\rho(\vec{r}, t) = 0$ the following wave-equations can be derived:

$$\left(\nabla^2 - \epsilon_0 \epsilon_r \mu_0 \mu_r \frac{\partial^2}{\partial t^2}\right) \vec{E}(\vec{r}, t) = 0 \tag{2.13}$$

and

$$\left(\nabla^2 - \epsilon_0 \epsilon_r \mu_0 \mu_r \frac{\partial^2}{\partial t^2}\right) \vec{B}(\vec{r}, t) = 0 \tag{2.14}$$

One solution of equation 2.13 for the electric field is:

$$\vec{E}(\vec{r}, t) = \vec{E}_0 \exp\left(\mathrm{i}\left(\vec{k}\vec{r} - \omega t\right)\right). \tag{2.15}$$

The wave vector $\vec{k}$ and the angular frequency ω are connected via the following dispersion relation

$$\vec{k}^2 = \epsilon_0 \epsilon_r \mu_0 \mu_r \omega^2 = \frac{n^2}{c^2} \omega^2. \tag{2.16}$$

In the following all calculations and explanations are performed for a plane wave. The direction of the propagation is chosen as z. Thus, equation 2.15 becomes (with $k_z = k$):

$$\vec{E}(z,t) = \vec{E}_0 \exp\left(\mathrm{i}\left(kz - \omega t\right)\right). \tag{2.17}$$

The angular frequency ω is the same in matter as in vacuum. The wave number k is affected by the matter as the propagation speed is not the same as in vacuum. Therefore, $k = nk_0$ with k_0 being the wave vector in vacuum. By substituting k in equation 2.17 it can be derived that

$$\begin{aligned} \vec{E}(z,t) &= \vec{E}_0 \exp\left(\mathrm{i}\left(nk_0 z - \omega t\right)\right) \\ &= \vec{E}_0 \exp\underbrace{\left(-\beta_\omega k_0 z\right)}_{\text{attenuation}} \exp(\mathrm{i}(\underbrace{(1-\delta_\omega)k_0 z}_{\text{phase-shift}} - \omega t)) \end{aligned} \tag{2.18}$$

It can be seen that the amplitude of an electromagnetic plane wave passing an object is attenuated and that the phase of the wave is shifted by the object. Those two observations are dependent on the material the wave passes.
Detecting the wave behind the object with a detector, just the intensity of the wave $I \propto |\vec{E}|^2$ can be measured. That means that after an object with thickness of $z = d$ the following intensity can be measured:

$$\begin{aligned} I &= |\vec{E}_0|^2 \exp\left(-2\beta_\omega k_0 d\right) \\ &= |\vec{E}_0|^2 \exp\left(-\mu d\right). \end{aligned} \tag{2.19}$$

μ is the material-specific attenuation coefficient. It is the sum of the attenuation coefficients of all interaction processes which contribute to the attenuation of the x-ray for medical x-ray imaging (see section 2.3) [14]

$$\mu = \mu_{\mathrm{PA}} + \mu_{\mathrm{CS}} \tag{2.20}$$

with μ_{PA} being the attenuation coefficient due to photoelectric absorption and μ_{CS} being the attenuation coefficient due to Compton scattering.

In equation 2.19 it can be seen that all information about the phase-shift of the plane wave within the object is lost by measuring the intensity of the wave behind the object. Thus, only attenuation processes during the propagation path of the wave

can be measured.

2.3 Interaction of x-rays with matter

The x-ray photons are passing matter which is in the beam path. Therefore, different interaction processes between x-ray and matter occur. In figure 2.8 the probabilities of the different interaction processes depending on the photon energy are shown. As above mentioned x-ray photons used in medical imaging have a maximal energy of about 150 keV. Thus in the following nuclear pair production and electron pair production can be neglected. Only photoelectric absorption (photoionization absorption or photo effect) and Compton scattering contribute to the interaction processes of x-rays with matter.

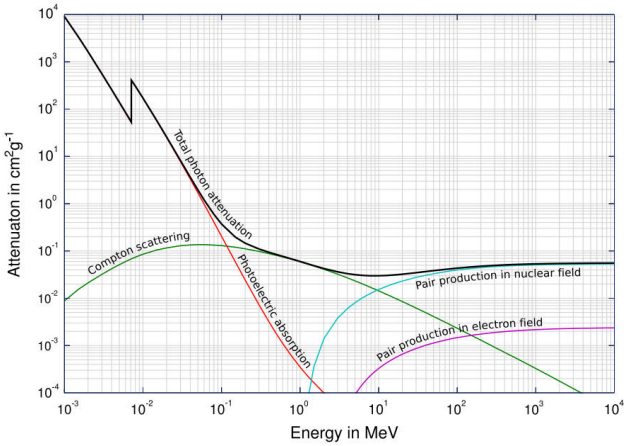

Figure 2.8: Probability of the different interaction processes of photons in matter depending on the photon energy. As the maximal energy of medical used x-rays is of about 150 keV, the only processes contributing to the interaction with matter are photoelectric absorption (photoionization absorption or photo effect) and Compton scattering. [4]

In figure 2.9 all interaction processes are shown schematically. Additionally to the photoelectric absorption (B) and to the Compton scattering (D) two further interaction possibilities are shown in the figure. There is firstly of course the case that no interaction happens because the photon is to far away from the atom (A). Secondly, there occurs Rayleigh scattering (C). This effect is not mentioned in figure 2.8 because no energy transfer happens.

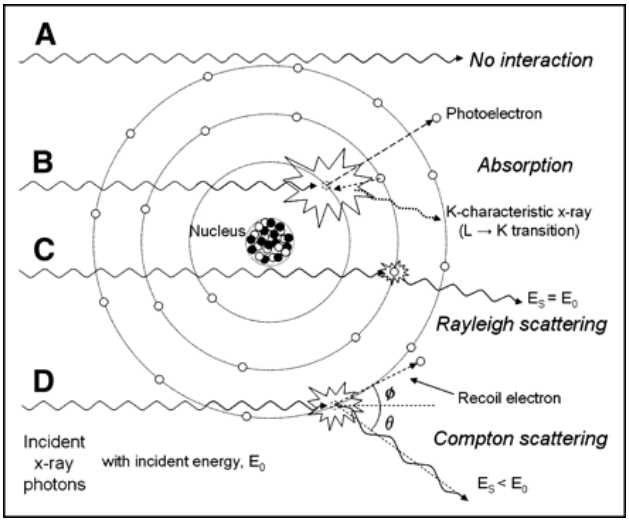

Figure 2.9: Schematic representation of the different interaction processes of photons with an atom at energies of medical used x-ray photons. Additionally to the photoelectric absorption and to the Compton scattering two further interaction possibilities are shown in the figure. Firstly, it might occur that no interaction happens because the photon is to far away from the atom. Secondly, there occurs Rayleigh scattering. [47]

2.3.1 Photoelectric absorption

For low photon energies up to around 100 keV photoelectric absorption is the dominant interaction process [4, 16].
During photoelectric absorption the incident photon interacts with an inner orbit electron of the atom. For this, the binding energy E_b of the electron has to be nearly equal but a little smaller than the energy of the incident photon. The photon is completely absorbed by the electron. Thus, all the energy of the photon E_ph is transferred to the electron. This electron leaves the atomic orbit with a kinetic energy $E_\mathrm{kin,e}$ which is the difference between the photon energy and the binding energy [14, 21, 47]:

$$E_\mathrm{kin,e} = E_\mathrm{ph} - E_\mathrm{b}. \tag{2.21}$$

The position of the missing electron in the orbit of the atom is filled with an electron of an outer orbit. As the binding energy of the electrons far away of the nucleus is smaller than the binding energy near the nucleus an x-ray photon is released during this process with the energy difference of both orbits. Thus, the emitted photoelectrons have a specific energy for each material. [14, 21, 47]
Compared to the incident photon the photo electron has low energy, thus, due to

this effect a strong attenuation affect of the x-rays can be measured.
The probability that photoelectric absorption happens is represented by the attenuation coefficient $\mu_{\mathrm{PA}}(E, Z)$. It is dependent on the atomic number Z and on the incident photon energy E_{ph} as following [31]:

$$\mu_{\mathrm{PA}}(E, Z) \propto \frac{Z^{n-1}}{E_{\mathrm{ph}}^3}. \tag{2.22}$$

For elements with small atomic numbers $n = 4.5$, for elements with large atomic numbers $n = 4$ holds true. Equation 2.22 is valid for photon energies below 511 keV. This is true for medical used x-rays.

2.3.2 Compton scattering

Compton scattering is an inelastic interaction between the incident photon of energy E_{ph} and an orbital electron of the atom. For this interaction the photon energy has to be much larger than the binding energy of the electron. Thus, the binding energy can be neglected and it can be assumed that the electron is unbound. The energy of the photon is transferred partially to the electron which leaves the atom with an angle ϕ ($> 0^\circ$ to $\sim 90^\circ$) relative to the trajectory of the incoming photon. The photon is scattered and moves on a trajectory with an angle θ (between 0° and 180°) relative to the incoming trajectory. It is of lower frequency than the incoming photon as a part of its energy is transferred to the electron [14, 21, 47]. The energy $E_{\mathrm{ph,\,s}}$ of the scattered photon can be calculated using the Klein-Nishina equation [47]:

$$E_{\mathrm{ph,\,s}} = E_{\mathrm{ph}} \frac{1}{1 + \frac{E_{\mathrm{ph}}}{511\,\mathrm{keV}}(1 - \cos\theta)} \tag{2.23}$$

Thus, the energy $E_{\mathrm{ph,\,s}}$ of the scattered photon becomes smaller as its scattering angle θ increases. For the scattering angle three divisions can be made depending on the energy of the incident photon: first, for photon energies of about 5 keV most of the photons are backscattered; second, for energies of about 20 keV the scattering directions are distributed isotropic; and third, for high photon energies of about 60 keV and higher, the photons are preferably scattered in forward direction [47]. As x-ray photons mainly contribute to the third group in this case mainly scattering in forward direction occurs.
Like for photoelectric absorption an attenuation coefficient μ_{CS} can be calculated [31]:

$$\mu_{\mathrm{CS}} \propto \frac{Z}{A} \frac{1}{E_{\mathrm{ph}}^n} \qquad \text{with } n = 0.5 \text{ to } 1. \tag{2.24}$$

In this equation Z is again the atomic number and A the mass number of the interacting atom.

2.3.3 Rayleigh scattering

Additionally to the inelastic processes described above, which lead to a loss of energy of the photons, an elastic scattering process can be observed. The incoming x-ray photon can interact with an orbital electron of the atom by elastic scattering. The electron is excited for a short time by absorbing the photon. Immediately after absorbing the photon the electron emits a photon with the same energy as the incoming one by returning to its previous energy level. The trajectory of this released photon is slightly different to the trajectory of the incident photon. This causes a phase-shift of the whole incoming wave. This phase-shift cannot be measured with conventional detection methods. The probability of Rayleigh scattering increases with increasing atomic number of the atom and decreasing x-ray energy [47]. As the energy of the photon does not change during this process no attenuation coefficient can be estimated for Rayleigh scattering. Thus, this effect does not contribute to the attenuation processes of x-rays in matter. However, the phase-shift caused by Rayleigh scattering contains information about scattering properties of the material the wave is passing. Thus, it is interesting to be able to measure this shift. In the following a method for measuring this shift is introduced.

Chapter 3

Tabot-Lau Interferometry

In this chapter a method is introduced to measure the attenuation of an electromagnetic wave, the information about the phase-shift of the wave and the scattering properties simultaneously. For this, the application of the Talbot- and the Lau-effect are combined to a so called Talbot-Lau interferometer. In the following both effects are explained separately and at the end of the chapter the functioning of a Talbot-Lau interferometer in toto is presented.

3.1 Talbot-effect

The Talbot-effect is named after H. F. Talbot [50] who was the first to observe self-images of a grating when illuminating it with a monochromatic coherent light source.
In figure 3.1 the experimental setup to observe the Talbot-effect is shown. A source (S) illuminates the grating G_1 with monochromatic, coherent radiation. Behind the grating an intensity pattern $I(x)$ can be observed. At determined distances of multiples of the so called Talbot distances z_T the intensity pattern has the same period as the grating. Such a Talbot pattern is shown in figure 3.2. It can be seen that at $z = z_\mathrm{T}$ the intensity pattern has the same periodicity as rightly behind the grating. At $z = 0.5 z_\mathrm{T}$ the frequency of the pattern is two times the frequency behind the grating. In figure 3.3 the Talbot pattern of the high-energy setup (see subsection 5.1.2) used to take the images presented in this thesis is shown. It is simulated for the design energy of the setup of 62 keV in the monoenergetic case.

The so called Talbot distances z_T can be calculated for an absorption grating with period g as [15, 46]:

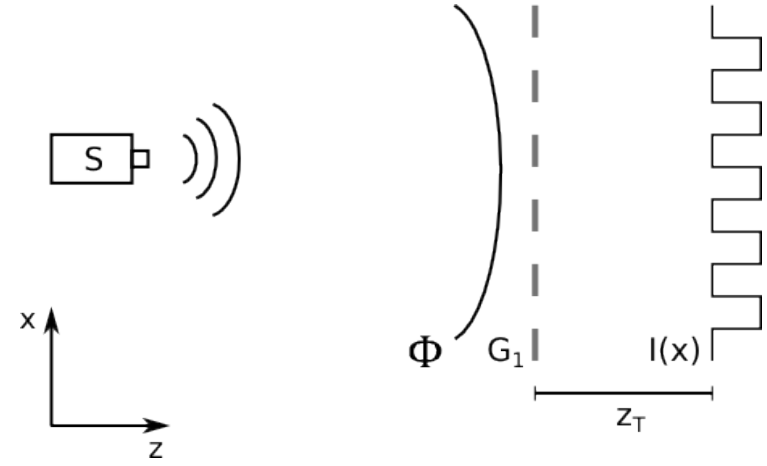

Figure 3.1: Setup for observing the Talbot-effect. S is a source emitting monochromatic, coherent radiation. G_1 is the periodic grating illuminated by the source. $I(x)$ is the intensity measured behind the grating. At distances of multiple of z_T behind G_1 self-images of the grating can be observed within the intensity pattern. (after [55])

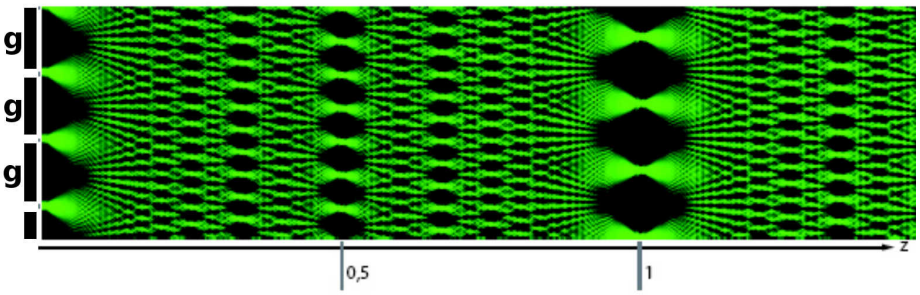

Figure 3.2: Ideal Talbot pattern behind a grating with grating period g. At $z = \frac{z_T}{2}$ a self-image of the grating with $\frac{g}{2}$ can be observed. At $z = z_T$ the pattern shows the same periodicity as the grating. (after [15])

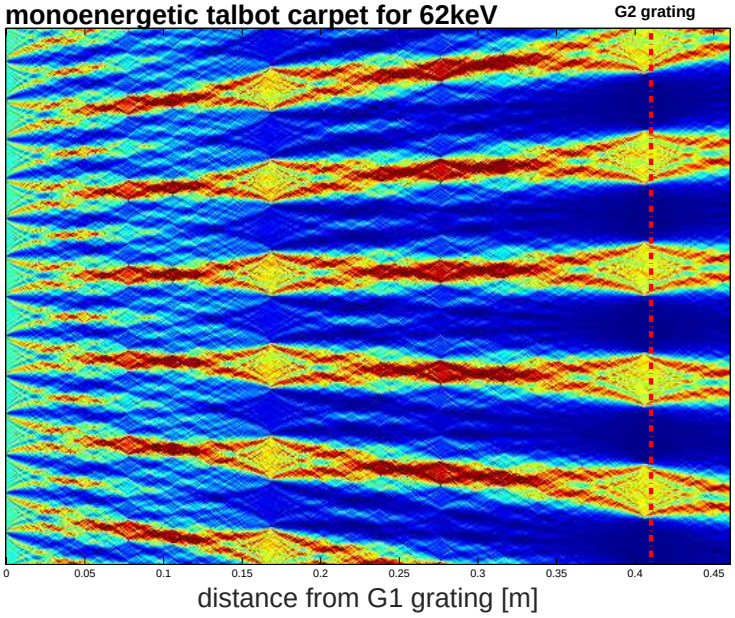

Figure 3.3: Talbot pattern for the high-energy setup used in this thesis (subsection 5.1.2).

$$z_T = 2n\frac{g^2}{\lambda} \qquad \text{with } n \in \{1,2,3,...\} \tag{3.1}$$

with λ being the wavelength of the incident plane wave.
In addition to the periodic pattern which shows the same frequency as the grating, further periodic structures can be observed at so called fractional Talbot distances. These structures can be seen at all rational multiples of z_T [12]. They show up a higher frequency than the grating. In figure 3.2 these fractal images can be seen. To measure this pattern a laser has been taken. Thus, figure 3.2 shows a Talbot pattern for a grating illuminated with nearly coherent radiation [15].
Putting a binary phase grating into the beam path the Talbot distances of the self-images of the grating differ from those of the absorption grating [35, 49]. The Talbot distances depend on the phase-shift implied by the grating and on the duty-cycle of the grating (that means the relation of the width of one grating bar to the distance between two grating bars). The general formula to calculate those fractional Talbot distances can be expressed as following [49]

$$z_T = \frac{(2M-1)}{2\eta}\frac{g^2}{\lambda} \qquad \text{with } M \in \{1,2,3,...\} \tag{3.2}$$

with

$$\begin{aligned} \eta = 1 \quad & \text{for a } \frac{\pi}{2}\text{-shifting grating with duty-cycle } 0.5 \\ \eta = 2 \quad & \text{for a } \pi\text{-shifting grating with duty-cycle } 0.25 \\ \eta = 4 \quad & \text{for a } \pi\text{-shifting grating with duty-cycle } 0.5 \end{aligned}$$

So far, it was assumed that the gratings are illuminated with a plane wave. In the setup a medical x-ray source is used, thus, the gratings are illuminated with a spherical wave. Henceforth, the magnification factor because of the diverging beam path has to be considered. The Talbot distances of a grating in front of a point-formed source are [56]

$$z_{\mathrm{T}}^{*} = \frac{L z_{\mathrm{T}}}{L - z_{\mathrm{T}}} \tag{3.3}$$

with L is the distance between the source and the grating.

3.2 Lau-Effect

Like the Talbot-effect the Lau-effect is named after its discoverer E. Lau [32].
As mentioned in section 3.1 the Talbot-effect can only be observed using spatially and temporally coherent monochromatic waves. This is only given for synchrotron radiation or micro-focus x-ray tubes. Conventional used x-ray sources have a large spotsize. Thus, the necessary spatial coherence of the emitted radiation is not given anymore [45].
But, with the help of the Lau-effect it is possible to observe a Talbot like effect even for spatially incoherent polychromatic radiation [28, 45].
In figure 3.4 the setup for observing the Lau-effect is shown. A source grating G_0 is placed in front of the source. This grating is illuminated with polychromatic incoherent radiation. Behind each slit of the grating the transmitted radiation is assumed to be spatial coherent. The radiation transmitting the single slits is mutually incoherent. The single coherent slit sources can be used to observe the Talbot-effect. Each slit source causes a Talbot-pattern of the phase grating G_1. The single Talbot-pattern have to be shifted laterally to each other so that they interfere constructively at the Talbot distance z_{T} behind G_1. Thus, the lateral offset of the Talbot patterns has to correspond with the period of the Talbot pattern g_2 at this Talbot distance [42].
The relation between the period g_0 of grating G_0 and of the period of the Talbot pattern g_2 can be calculated using the intercept theorem [45]:

$$\frac{g_0}{g_2} = \frac{l}{z_T}, \tag{3.4}$$

where l is the distance between the source grating G_0 and the phase grating G_1 and z_T is the Talbot distance.
Making use of the Lau-effect it is possible to use large polychromatic sources for Talbot-Lau interferometry.

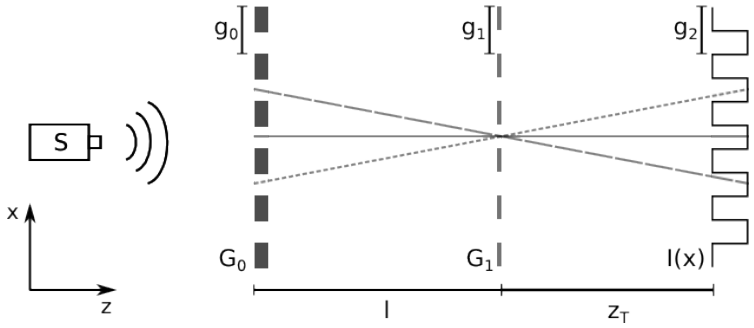

Figure 3.4: Setup for observing the Lau-effect. The grating G_0 is illuminated with incoherent polychromatic radiation. It causes single coherent slit sources. Those sources lead to Talbot patterns of G_1. These Talbot patterns have to be shifted to each other so that they interfere constructively. The dashed lines represent the exemplary beam paths. (after [55])

3.3 Talbot-Lau interferometry

In Talbot-Lau interferometry the Talbot- and the Lau-effect are used to get information about the phase-shift of an electromagnetic wave caused by an object in the beam path additionally to its attenuation properties. In 1971 Lohmann and Silva [34] used the optical Talbot-Lau effect to get phase information about an object using a polychromatic light source. They put the object between the source grating G_0 and the phase grating G_1. Thus, the phases of the waves transmitted by the different slit sources are shifted depending on the object properties. This results in distortions of the Talbot pattern behind G_1. These distortions due to the object influence on the wave can be observed and provide information about the phase-shifting and scattering properties of the object in the beam path. In 1979 Bartelt and Jahns refined and mathematically explained the Talbot-Lau setup.

In 1992 Clauser and Reinsch [19] proposed to use Talbot-Lau interferometry also for x-radiation. They introduced a setup with three gratings, which is shown in figure 3.5. In addition to the two gratings used to observe the Talbot-Lau-effect for incoherent polychromatic sources a third grating G_2 is placed downstream of the

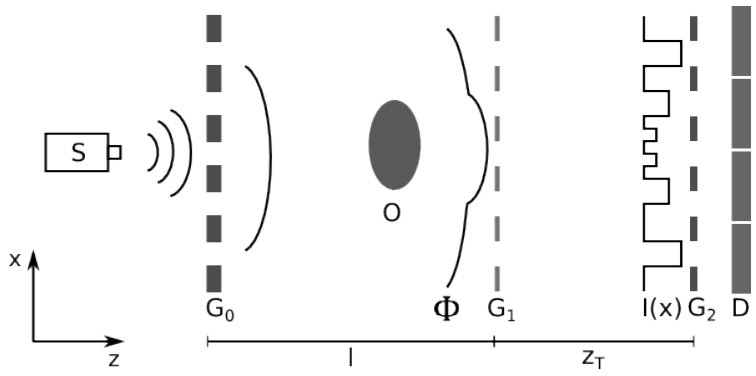

Figure 3.5: Setup of a Talbot-Lau interferometer. The object O deforms the wave front emitted by the source S. Because of the Lau-effect (due to the gratings G_0 and G_1) a periodic intensity pattern can be observed in a Talbot distance behind G_1. The period of the intensity pattern is small, compared to the size of the detector pixel. To be able to measure the pattern a phase-stepping is performed with a third grating G_2. It is used to sample the intensity pattern and has to be placed in the Talbot distance z_T downstream of G_1. l has to be determined using the ratio of equation 3.4. (after [55])

phase grating G_1. For x-rays the period of the self-image is much smaller than a detector pixel. With the help of grating G_2 it is possible to observe the self-image of the phase grating G_1 even for x-rays. Clauser and Reinsch proposed that the slit period of G_2 has to be equal to a rational multiple of the period of G_2. That means in the best case G_1 has open slits at the position of the self-image maxima of G_1 and closed slits elsewhere. G_2 has to be placed in a Talbot distance z_T behind G_1. The grating bars of all three gratings are aligned in parallel position (in figure 3.5 the grating bars are aligned in y-direction). By moving the grating G_2 perpendicular to its grating bars (in figure 3.5 in x-direction) the self-image pattern of G_1 can be sampled. Thus, even if the resolution of the detector is to low to detect the self-image it can be measured by moving the grating in front of the detector and by sampling the pattern. Though, it is no problem that the pixelsize of the detector is normally larger than the period of the intensity pattern behind G_1 for x-rays. Weikamp et al. [56] used a π-shifting grating G_1 and an absorption grating G_2. The distance between G_1 and G_2 should correspond to the Talbot distance of G_1. Due to equation 3.2 this means for a π-shifting grating with duty-cycle 0.5 [56]:

$$d_T = z_T = \left(M - \frac{1}{2}\right)\frac{g_1^2}{4\lambda} \quad \text{with } M \in \{1, 2, 3, ...\} \tag{3.5}$$

The period of G_2 should match the period of the self-image of G_1 in distance d_T. If the periods of the self-image and of G_2 do not fit perfectly, Moiré pattern can be seen in reference/free-fied images [56].

In conventional setups G_2 is moved a predefined number of equidistantly distributed steps over a predefined number of periods. The positions of G_2 are subsequently called phase-step positions.

An object placed in the beam path perturbs the pattern of the slit sources behind G_0. This leads to local displacement of the periodic pattern behind G_1. This displacement between the free-field measurement and the measurement with the object in the beam path can be measured with this phase-stepping method [56].

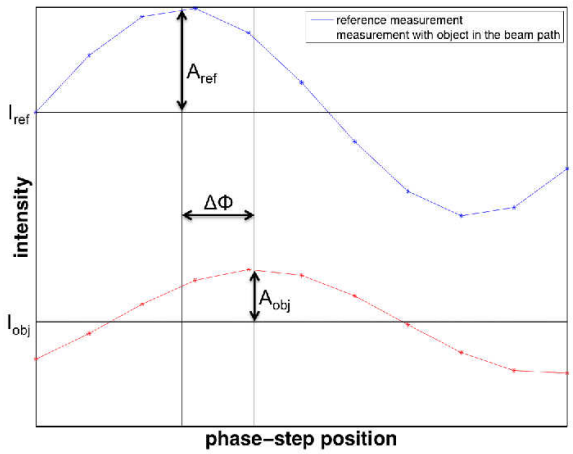

Figure 3.6: Schematic representation of two phase-stepping curves. The phase of the intensity curve with the object in the beam path is shifted, the offset is lowered and the relation between amplitude and offset change for the object in the beam path.

In figure 3.6 a schematic drawing of two sampled curves is shown. The blue curve shows the intensity distribution without an object in the beam path and the red curve with an object in the beam path. It can be observed that the phase ϕ, the offset I_0 and the ratio between offset and amplitude V might change by putting an object in the beam path. Thus, they can be used to calculate the image information (chapter 4). These three parameters can be calculated with a least square fit of a sinusoidal function for each phase-stepping curve (after [9]):

$$I(n) = I_0 \cdot \left(1 + V \cdot \sin\left(\frac{2\pi np}{N} + \phi\right)\right) \quad \text{with } n \in \{0, .., N-1\} \tag{3.6}$$

where I_0 is the offset of the sinusoidal curve, $V = \frac{A}{I_0}$ is the visibility (with A being the amplitude of the wave, see section 4.3), N is the number of phase-steps performed for the measurement, p is the number of periods sampled and ϕ is the phase-shift. To calculate the different parameters the position of the phase-steps has to be known

very precisely. Using the term $\frac{2\pi np}{N}$ an equidistant distribution of the phase-steps is assumed. In the conventional imaging process an equidistant phase-stepping is performed because it is easiest to handle. As the motor which moves the grating G_2 does not move as precisely as necessary, artifacts occur. The possibilities to remove or to avoid these artifacts are discussed in the following.

Chapter 4

Imaging modalities of a Talbot-Lau interferometer

In the following chapter the three different imaging modalities of a Talbot-Lau interferometer - the attenuation image, the differential phase-contrast image and the dark-field image - are presented. The formation of the image information and the principles of the mathematical background are explained.
To visualize the properties of the different effects in the three imaging modalities four prepared jelly babies are imaged (figure 4.1).

Figure 4.1: Photography of four jelly babies which are imaged in the following sections with a Talbot-Lau interferometer. From left to right: jelly baby not worked on, jelly baby with wooden skewer, jelly baby with metallic pin and jelly baby with PMMA beads of 6 µm diameter on the head. [60]

4.1 Attenuation Image

The most familiar imaging modality of Talbot-Lau imaging is the attenuation image. This is the image gained in many conventionally used setups like 2D x-ray imaging or CT setups. It contains information about the attenuation properties of the different materials of the object. Due to interaction with matter the intensity of an incoming wave is attenuated by passing an object. As described in chapter 2 the attenuation is due to photoelectric effect and Compton effect. The intensity of the wave with incoming intensity I_0 and propagation direction z after passing an object can be calculated using

$$I(z) = I_0 \exp\left(-\int_0^z \left(\mu_{\mathrm{PS}}(z') + \mu_{\mathrm{CS}}(z')\right) \mathrm{d}z'\right) \tag{4.1}$$

with $\mu_{\mathrm{PS}}(z')$ being the attenuation coefficient of photoelectric absorption and $\mu_{\mathrm{CS}}(z')$ being the attenuation coefficient of Compton scattering. In most materials the attenuation coefficients are not constant and may change continuously in space. An integral is performed over the propagation path.
The attenuation image shows the comparison of the intensity of the free-field measurement and of the object measurement.
It is calculated as following (after [9]):

$$T = -\ln\left(\frac{I_{\mathrm{obj}}}{I_{\mathrm{ref}}}\right) \tag{4.2}$$

where I_{ref} is the offset of the phase-stepping curve of a free-field/reference measurement and I_{obj} is the offset of the phase-stepping curve with the object in the beam path (see equation 3.6).

The contrast in the attenuation image depends on the attenuation coefficient of the different materials. As shown in section 2.3 the attenuation coefficients are dependent on the atomic number and on the mass number of the matter. Therefore, in medical attenuation images especially the bone-tissue contrast is shown as the differences of the atomic number and the mass number of bone (consists mainly out of calcium) and tissue (consists mainly out of water) are large. Thus, for example, the attenuation image is used in medicine to diagnose bone fractures.

In figure 4.2 the attenuation image of the jelly babies of figure 4.1 is shown. Because of the high attenuation coefficient of metal the pin can be seen well. The wooden skewer can just be seen outside the jelly baby. Inside the jelly baby the wooden

skewer is invisible because its attenuation coefficient is too low compared to the attenuation coefficient of the gelatine of the jelly babies. The PMMA beads are not visible at all.

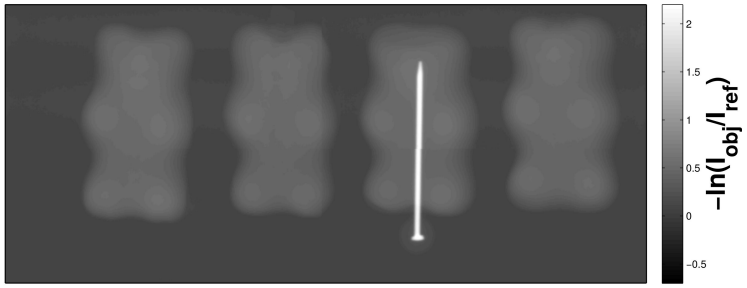

Figure 4.2: Attenuation image of the jelly babies. The pin can be seen well in the image. Neither the wooden skewer nor the PMMA beads can be seen. (after [60])

4.2 Differential Phase-Contrast Image

By performing phase-stepping it is possible to get information about the phase-shift of a wave after passing an object. The phase-shift is caused by different velocities of the wave in different matter. The wavefront is tilted by the angle α compared to the incoming wave (figure 4.3). This results in a phase difference $\Delta\Phi$ comparing the phase Φ_{ref} of a reference scan without perturbation with the phase Φ_{obj} with object in the beam path [9]:

$$\Delta\Phi = \Phi_{\text{obj}} - \Phi_{\text{ref}} \tag{4.3}$$

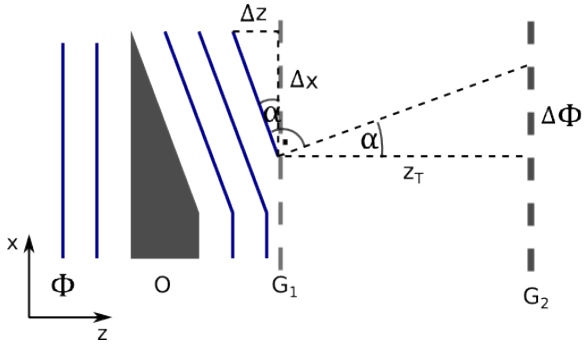

Figure 4.3: Passing an object the incoming plane wavefront is tilted by an angle α. As the wave is propagating between G_1 and G_2 a phase difference $\Delta\Phi$ between a not perturbed wave Φ_{ref}, which propagates straight forward and the perturbed wave Φ_{obj} can be measured. (after [8])

As it can be seen in figure 4.3 the difference can be expressed by

$$\Delta\Phi = z_{\mathrm{T}} \tan(\alpha) \tag{4.4}$$

with z_{T} the Talbot distance between G_1 and G_2.

The phase-shift can be expressed by:

$$\Delta\phi = k\Delta z = \frac{2\pi}{\lambda}\Delta z \tag{4.5}$$

where k is the wave number of the incoming wave and λ is the wavelength. Thus, $\tan(\alpha)$ can also be expressed by (after [45])

$$\tan(\alpha) = \frac{\Delta z}{\Delta x} = \frac{\lambda}{2\pi}\frac{\Delta\phi}{\Delta x}. \tag{4.6}$$

Equation 4.4 and equation 4.6 lead to [56]

$$\Delta\Phi = \Phi_{\mathrm{obj}} - \Phi_{\mathrm{ref}} = \frac{\lambda}{2\pi}\frac{\partial\phi}{\partial x} z_{\mathrm{T}}. \tag{4.7}$$

That means that the measured phase difference of the object phase and the reference phase is the deviation of the phase perpendicular to the grating bars. Thus, in differential phase-contrast images edges are seen most clearly. Additionally, the differential phase-contrast image is dependent on the direction of the grating bars. Only edges perpendicular to the grating bars can be imaged because of the deviation in x-direction.
According to equation 2.18 the phase-shift of a wave can be expressed by [40]:

$$\int_{\mathrm{detector}} \frac{\partial\phi}{\partial x}\mathrm{d}x = -\frac{2\pi}{\lambda}\int \delta_\omega(x,y,z)\mathrm{d}z \tag{4.8}$$

where $(1-\delta_\omega)$ is the real part of the diffraction index (equation 2.12). Thus, the absolute phase of an object contains information about the real part of its diffraction index.

In figure 4.4 the differential phase-contrast image of the jelly babies is shown. Again the pin inside the third jelly baby can be seen. In addition the wooden skewer is visible inside the second jelly baby and even the PMMA beads on the head of the forth jelly baby are slightly recognisable. This is due to the fact that in differential phase-contrast image edges are shown even if they are inside an object independent on the attenuation coefficients. Thus, it is possible to detect tiny structures and to

enhance soft-tissue contrast compared with attenuation imaging [41].
For example, in medicine it might be possible to diagnose ruptures of tendons in differential phase-contrast images. Additionally, margins as those of breast tumours can be better detected in the differential phase-contrast image [48].

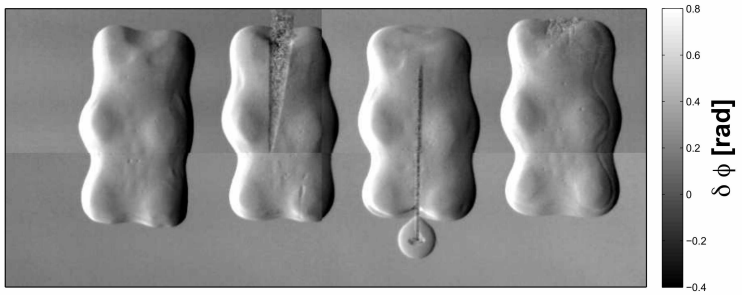

Figure 4.4: Differential phase-contrast image $\Delta\Phi$ of the jelly babies. The pin and the wooden skewer can be seen well in the image. Even the PMMA beads are slightly recognisable. (after [60])

4.3 Dark-field Image

In addition to attenuation image and differential phase-contrast image a third image type, the dark-field image, can be calculated using a Talbot-Lau interferometer. Coherent scattering within an object causes angular divergence of the incoming beam. This leads to a decrease of the amplitude of the self-image [36]. This effect can be used to get information about the scattering properties of an object and to image sub-micrometer structures [44].
The visibility V, which is necessary to calculate the dark-field image, can be calculated with the knowledge of the offset of the intensity I and the amplitude A of the wave after having passed an object [36]:

$$V = \frac{A}{I}. \tag{4.9}$$

For calculating the dark-field image the information measured with the object in the beam path V_{obj} is compared to the information of a reference scan V_{ref} [44]:

$$D = \frac{V_{\text{obj}}}{V_{\text{ref}}}. \tag{4.10}$$

This quotient contains the information about the scattering properties of an object. If the wave is scattered while passing the object the amplitude of the wave will decrease because of interference effects of the scattered waves [44, 57].

Scattering especially happens for very tiny particles or structures. Thus, in dark-field images such structures of sub-micrometer scale are visible even if they cannot be seen in attenuation and differential phase-contrast images [44]. But also sharp edges produce a dark-field signal [58]. No dark-field can be reconstructed if beam hardening occurs due to a high attenuation coefficient of the object [59].
For the sake of better comparability of the dark-field image and the attenuation image the dark-field image is shown as

$$D_{\ln} = -\ln\left(\frac{V_{\text{obj}}}{V_{\text{ref}}}\right) \tag{4.11}$$

In figure 4.5 the dark-field image $D_{\ln}$ of the jelly babies of figure 4.1 is shown. The wooden skewer can clearly be seen in jelly baby two. This is due to the fibrous structure of wood. This leads to massive scattering of the incoming wave and therefore a strong dark-field signal can be measured. The pin also gives a high dark-field signal. This is caused by beam hardening and the edge of the pin. In dark-field image even the PMMA beads can be seen. This shows an important feature of Talbot-Lau interferometry as it is possible to visualize structures which are smaller than a detector pixel.

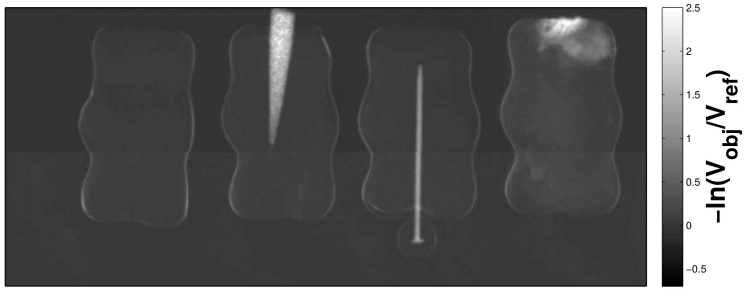

Figure 4.5: Dark-field image $D_{\ln}$ of the jelly babies. The wooden skewer and the pin can be seen well in the dark-field image. Even the PMMA cause show a change of the dark-field signal. (after [60])

The possibility to image sub-micrometer structures in dark-field images opens many new opportunities for non-destructive testing and especially for medical imaging. As it can be seen in figure 4.5 even the beads can be seen in dark-field images. Thus, dark-field imaging can be used to show up microcalcifications in mammography in an earlier stadium as it is possible with conventional attenuation mammography. To observe microcalcifications of a breast tumour in attenuation images, the calcification has to be large and compact enough to attenuate the incoming beam. At this stadium the tumour might be at an advanced state. As it is possible to depict tiny, scattering structures in dark-field images, tumours can be earlier diagnosed [24, 38, 48].

Also lung diseases might be diagnosed earlier using dark-field images. The lung consists of many very small pulmonary alveoli. These alveoli cause x-ray scattering. If there is an anomaly within the lung concerning the alveoli this can be seen in dark-field image because of the change of the scattering properties [11].

Chapter 5

Material and Methods

In the following chapter the setups used for data acquisition are characterized. Thereafter, the algorithms and methods developed during this master thesis are presented. All images shown in the following chapters have been taken during the work for this master thesis.

5.1 Talbot-Lau setups

5.1.1 Low-energy setup

All image data concerning the temperature drift effects (subsections 5.2.1 and 6.1.1) is acquired with a setup which has been designed for imaging mastectomy samples. The distances used in the setup and the properties of the gratings are shown in table 5.1 and table 5.2. For the design energy of 25 keV the analyzer grating G_2 is positioned in the third Talbot distance behind the phase grating G_1. The acceleration voltage can be varied between 40 kV and 125 kV. The x-ray tube of the setup is a Siemens MEGALIX Cat Plus 125. The detector is a Varian PaxScan 2520D with 127 µm pixelpitch. The field of view has a size of about 6 cm × 2 cm.

Table 5.1: Low-energy setup: distances between the components

source grating (G_0) - sample	143.8 cm
sample - phase grating (G_1)	6.4 cm
phase grating (G_1) - analyzer grating (G_2)	15.9 cm

Table 5.2: Low-energy setup: properties of the gratings

	G0	G1	G2
material	Au	Ni	Au
period [μm]	24.39	4.37	2.4
height of bars [μm]	150	8.7	110
duty cycle	0.5	0.5	0.5

5.1.2 High-energy setup

All image data not concerning the temperature drift effects (subsections 5.2.2, 5.3.1, 5.3.2, 6.1.2, 6.2.1 and 6.2.2) is acquired in a setup for x-ray grating-based Talbot-Lau imaging described in the following. A phase-shift of $\frac{\pi}{2}$ caused by the phase grating G_1 can be achieved at the design energy of 62.5 keV. It is possible to use acceleration voltages between 50 kV and 125 kV without lowering visibility too much. In the setup a Siemens MEGALIX Cat Plus 125/40/90-125GW is used as x-ray source. The detector is a PerkinElmer DEXELA 1512 with 75 μm pixelpitch. The field of view is of about 2.9 cm $\times$ 6.9 cm. [26]
Further properties of the setup are shown in table 5.3, table 5.4 and in the Master-Thesis of Hauke [26].

Table 5.3: High-energy setup: distances between the components [26]

source grating (G_0) - sample	59.3 cm
sample - phase grating (G_1)	41.1 cm
phase grating (G_1) - analyzer grating (G_2)	41.0 cm

Table 5.4: High-energy setup: properties of the gratings [26]

	G0	G1	G2
material	Au	Au	Au
period [μm]	11.54	3.39	4.8
height of bars [μm]	290	6.37	180
duty cycle	0.5	0.5	0.5

5.2 Long-term drift effects

In x-ray phase-contrast imaging the incident wave is diffracted by the object in the beam path. This diffraction leads to a lateral shift of the Talbot fringes in the plane of the analyzer grating. The size of the shift depends on the diffraction index of the object. It can be measured as the phase-shift $\phi(x, y)$ of the incident wave downstream

of the phase grating G_1 in each detector pixel (x, y). Ideally, it is assumed that the phase-map of a reference measurement is constant in time. But, measurements show that the phase-shift is time-dependent $\phi(x, y, t)$. This time dependency can be due to thermal effects in the imaging system. Figure 5.1 shows the time dependency of a phase-map (reference phase) $\phi(x, y, t)$ after unwrapping the measured phase.

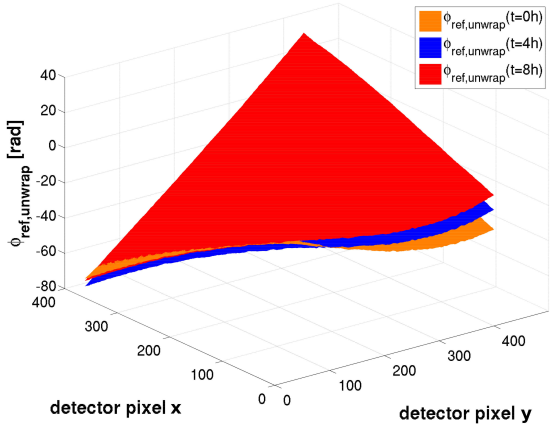

Figure 5.1: Reference phase image taken at three different times: plot of unwrapped reference phase images: $\phi_{\text{ref,unwrap}}(t = 0\,\text{h})$ (orange), $\phi_{\text{ref,unwrap}}(t = 4\,\text{h})$ (blue) and $\phi_{\text{ref,unwrap}}(t = 8\,\text{h})$ (red).

To extract the information about the object using the phase $\phi_{\text{obj}}(x, y, t_{\text{obj}})$ with the object in place, it is necessary to substract the phase of the free-field $\phi_{\text{ref}}(x, y, t_{\text{ref}})$. Due to the time dependency of the phase it would be advantageous to measure the object phase $\phi_{\text{obj}}(x, y, t_{\text{obj}})$ and the reference phase $\phi_{\text{ref}}(x, y, t_{\text{ref}})$ rightly consecutively, with $\Delta t = t_{\text{obj}} - t_{\text{ref}}$ as small as possible. In the (medical) workflow it is often not possible to perform a measurement under these conditions. There, the patient needs some time to be positioned or there is not enough time to take a reference image for each patient. Also in non-destructive testing it may not be possible to take reference images as often as it would be necessary to achieve artifact free images. Because of the limited field of view due to the size of our analyzer grating it may be necessary to tile the image in many partial images depending on the object size. Figure 5.2 shows the reconstructed differential phase-contrast image of a human hand (ex-vivo) using just one reference phase image taken at the beginning of the measurement. Structural information of the object is superimposed by artifacts which are caused by phase drifting effects.

In figure 5.3 a reference image taken for the image of the human hand (figure 5.2) is shown. Due to grating imperfections and not perfectly aligned gratings the reference phases vary from pixel to pixel within $[0, 2\pi[$. To smoothen the reference phase

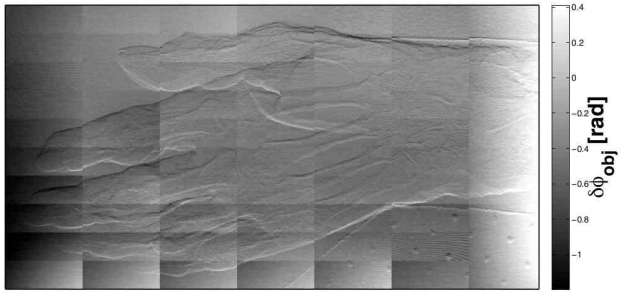

Figure 5.2: Differential phase-contrast image of a human hand, reconstructed using just one reference phase image, taken at the beginning of the measurement. Structural information of the hand is superimposed by artifacts, caused by drift of the phase. (Measurement parameters: tube voltage: 75 kV, tube current: 15 mA, minimal dose in one tile: 0.17 mGy air kerma, maximal dose in one tile: 0.49 mGy air kerma)

image an unwrapping algorithm is performed (Figure 5.4). After performing the unwrapping algorithm the phase-map can be modeled by a polynomial [22]. Thus, a 2D 5^{th} degree polynomial is fitted in the measured and unwrapped phase image (figure 5.5).

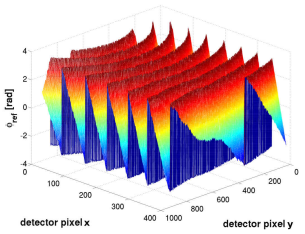

Figure 5.3: Reference phase image ϕ_{ref} in the field of view.

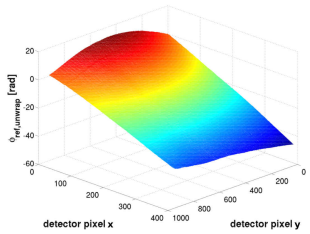

Figure 5.4: Reference phase image after applying an unwrapping algorithm ($\phi_{\text{ref,unwrap}}$).

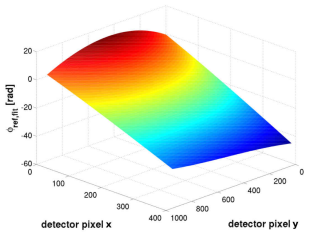

Figure 5.5: Fit of a 2D polynomial of 5^{th} degree in the unwrapped reference phase image ($\phi_{\text{ref,fit}}$).

After performing the fit algorithm the residuals between the measured phase and the fit polynomial are calculated, using $\phi_{\text{res}}(x,y,t) = \phi_{\text{unwrap}}(x,y,t) - \phi_{\text{fit}}(x,y,t)$.

Figures 5.6, 5.7 and 5.8 show that the time-dependence of the residuals $\phi_{\text{res}}(x,y,t)$ is small [22] with a root mean square of $\langle\sqrt{(\phi_{\text{res}}(x,y,t_1) - \phi_{\text{res}}(x,y,t_2))^2}\rangle_{x,y} = 0.0036\,\text{rad}$, so $\phi_{\text{res}}(x,y,t) \simeq \phi_{\text{res}}(x,y)$. This can be explained by the fact that the residuals result from inhomogeneities of the gratings with the assumption that all drift effects are represented by the polynomial. These inhomogeneities are time-independent. In figure 5.9 it can be seen that the difference of the residuals taken at the beginning of the measurement ($t = 0\,\text{h}$) and after 22 hours ($t = 22\,\text{h}$) are

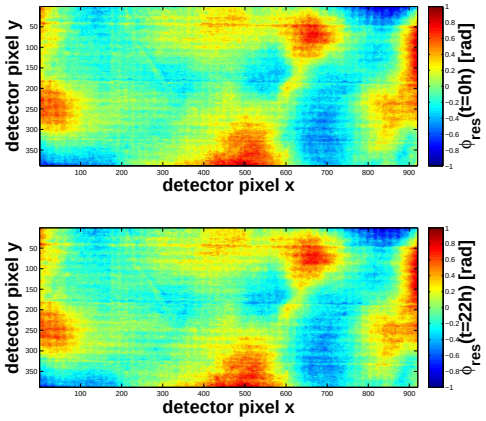

Figure 5.6: Graphic representation of the residuals $\phi_{\mathrm{res}}(x,y,t) = \phi_{\mathrm{unwrap}}(x,y,t) - \phi_{\mathrm{fit}}(x,y,t)$ taken at the beginning of the measurement ($t = 0\,\mathrm{h}$) (top) and after 22 hours ($t = 22\,\mathrm{h}$) (bottom).

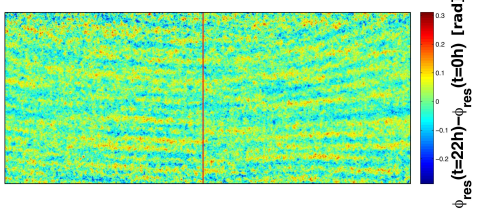

Figure 5.7: Difference of the residuals shown in Figure 5.6 which are taken at $t = 0\,\mathrm{h}$ and $t = 22\,\mathrm{h}$. $\phi_{\mathrm{res}}(t = 22\,\mathrm{h}) - \phi_{\mathrm{res}}(t = 0\,\mathrm{h})$. The red line shows the position of the line plot in figure 5.8.

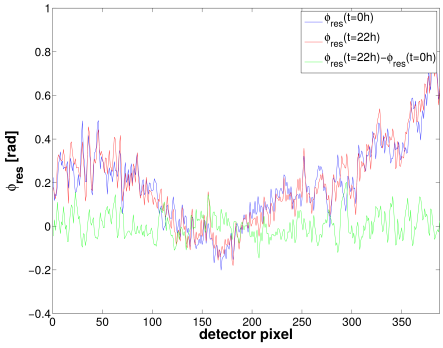

Figure 5.8: Lineplot of the residuals shown in Figure 5.6 which are taken at $t = 0\,\mathrm{h}$ (blue) and $t = 22\,\mathrm{h}$ (red) and of the difference of these residuals $\phi_{\mathrm{res}}(t = 22\,\mathrm{h}) - \phi_{\mathrm{res}}(t = 0\,\mathrm{h})$ (green).

distributed with a Gaussian distribution around zero ($\mu = -2.24 \cdot 10^{-13}$ rad $\simeq 0$ rad and $\sigma = 0.06$ rad). In the following it is assumed that the residuals are time-independent and the slight variations over time are neglected.

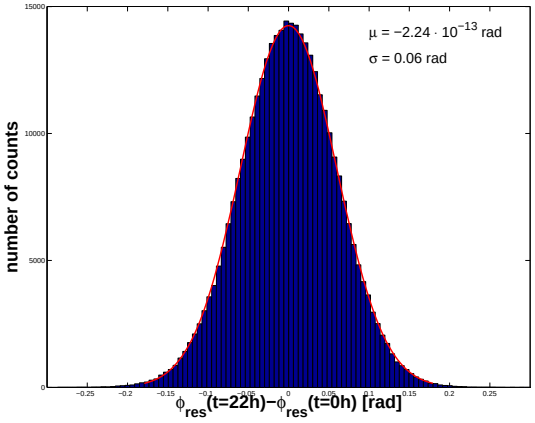

Figure 5.9: Histogram of the difference of the residuals taken at the beginning of the measurement ($t = 0$ h) and after 22 hours ($t = 22$ h). It can be seen that the difference can be described by a Gaussian distribution around zero (red).

5.2.1 Temperature drift effects

The first approach to explain the phase-drifts has been the observation of the change of the temperature during the measurement. Due to long measurement periods the x-ray tube gets very hot. This leads to a warming up of the gratings and of the whole setup. This causes a phase-shift of the reference phase-map depending on the temperature of the components of the setup. To verify this assumption temperature sensors are mounted on the source grating G_0, on the analyzer grating G_2, on the tube and on the detector of the low energy setup described in section 5.1.1. As temperature sensors are used air sensors type K (NiCr-Ni) with a measurement range between -50°C and 1000°C (Conrad 120756) which have been connected with a Sensor-CASSY 2, Leybold 524013 to read out the information.
To detect all temperature drifts and to observe if a steady state can be reached the measurement took a long time period of 8 h. A reference measurement and a measurement with a PMMA wedge in the beam path have been performed alternately. Within the 8 h about 150 reference measurements and 150 measurements with the PMMA wedge in the beam path have been performed.
Afterwards, a 5^{th} degree polynomial is fitted in each unwrapped reference phase scan and the fit factors (the offsets, x-gradient, y-gradient and factors of higher order) are compared to the temperature change of the components of the setup. As

the gradients of higher order are around zero, just the analysis of the offset, the x-gradient and the y-gradient are shown in detail in this thesis. The analysis of the gradients of second order is briefly shown as an example for the gradients of higher order. In figure 5.10 the temperatures are plotted in comparison with the offset (A), the x-gradient (B) and the y-gradient (C) calculated by performing a least square fit.

It can be observed that the course of the offset and of the x-gradient can be best described with the help of the temperature of G_2 (tables 5.5 and 5.6, figure 5.11 A, B). It is possible to describe the offset and the x-gradient using the temperature of G_2 just by applying a linear fit: $\phi_i(T_{G_2}) = a_i \cdot T_{G_2} + b_i$ with $\phi_i(T_{G_2})$ being the offset or the x-gradient, T_{G_2} being the temperature of G_2 and a and b are fit-factors.

The offset and the x-gradient calculated with the help of the G_2 temperature will be used in the following to calculate the differential phase-contrast images of the wedge.

Table 5.5: Goodness of fit of the offset and the different temperatures/the mean

parameters to calculate the χ^2 value	χ^2
temperature of the detector	1.06
temperature of G_2	0.06
temperature of G_0	6.45
temperature of the x-ray tube	3.78
mean value over all measured values	3.74
mean value starting with measurement values after 2 h 40 min	4.00

Table 5.6: Goodness of fit of the x-gradient and the different temperatures/the mean

parameters to calculate the χ^2 value	χ^2
temperature of the detector	$1.68 \cdot 10^{-4}$
temperature of G_2	$1.12 \cdot 10^{-5}$
temperature of G_0	$1.90 \cdot 10^{-4}$
temperature of the x-ray tube	$1.10 \cdot 10^{-3}$
mean value over all measured values	$2.00 \cdot 10^{-3}$
mean value starting with measurement values after 2 h 40 min	$3.63 \cdot 10^{-4}$

The gradient in y-direction is not affected by the temperature changes of the gratings (table 5.7, figure 5.10 C) especially of the analyzer grating G_2 as the grating bars are parallel to the y-direction. As can be seen in equation 4.7 the measured phase is just dependent on the phase-shift in x-direction. As the y-gradient varies statistically in a low range the mean of the calculated y-gradients will be taken to reconstruct the differential phase-contrast images of the wedge (figure 5.11 C). The setup has to be

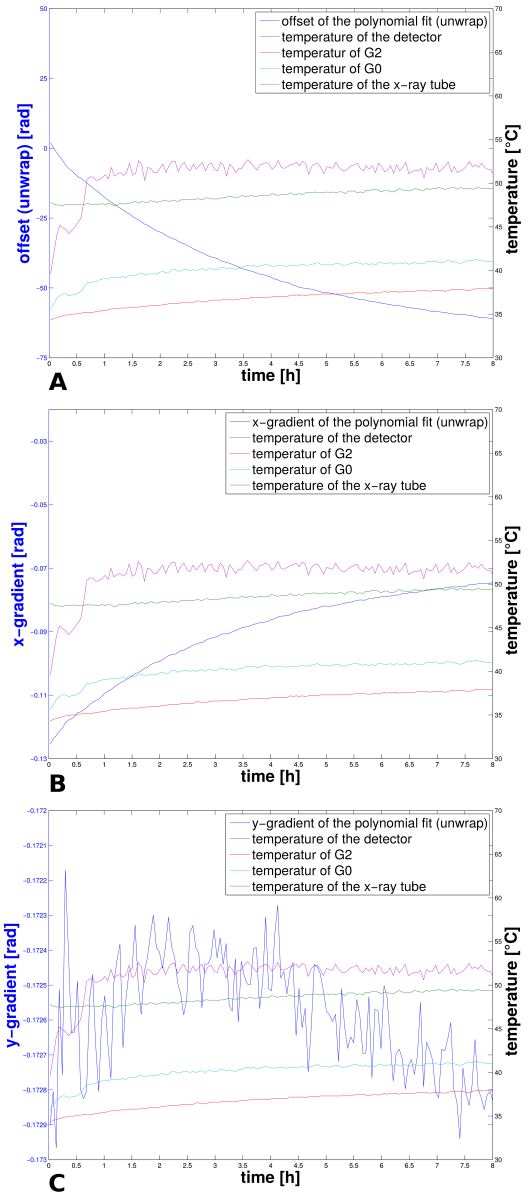

Figure 5.10: Temperature of the tube (purple), G_0 (greenish blue), G_2 (red) and the detector (green) in comparison with the offset (A, blue), the x-gradient (B, blue) and the y-gradient (C, blue).

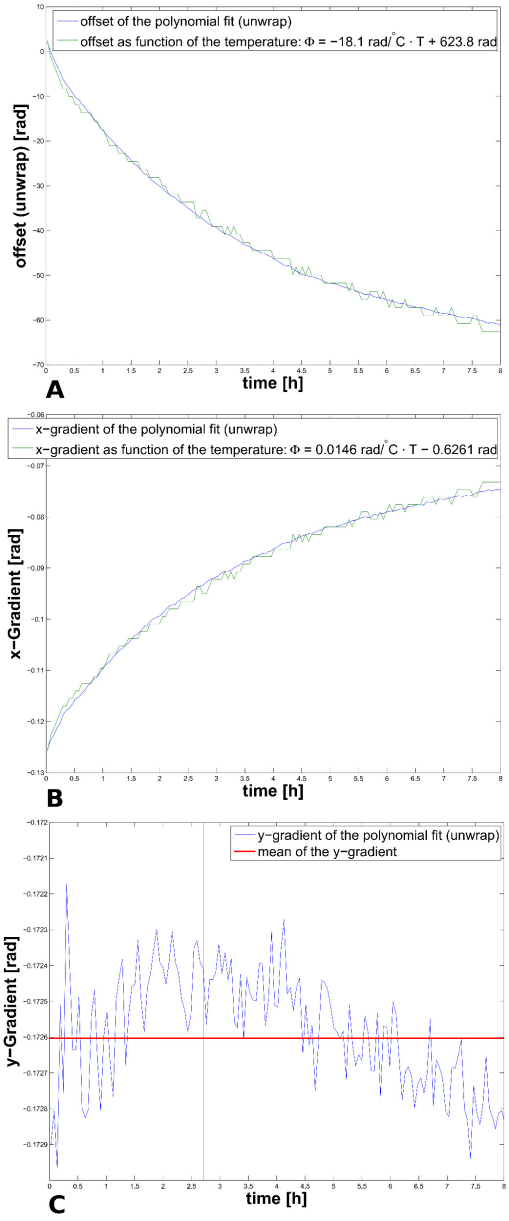

Figure 5.11: Fit of the temperature of G_2 (green) in the parameters for the offset (A, blue) and of the x-gradient (B, blue) calculated by the least square fit of a 5^{th} polynomial. Y-gradient (C, blue) and the mean of the y-gradient (red) after 2 h 40 min.

in steady state to make a general statement about the mean of the y-gradient. The gradient is never constant that means that no steady state is achieved. Nevertheless, in figure 5.10 can be seen that the changes of the offset and of the x-gradient decrease in the course of time. In the following, it is assumed that the changes after 2 h 40 min are small and a steady state can be assumed. After this time period all warm-up processes should be finished. Therefore, for calculating the mean value only gradients measured after this time point are taken into account. The chosen time of 2 h 40 min is a compromise between, on the one hand, the need of preparation time before starting measuring which should be as short as possible and, on the other hand, the difficulty to observe changes of the parameters which are as small as possible.

Table 5.7: Goodness of fit of the y-gradient and the different temperatures/the mean

parameters to calculate the χ^2 value	χ^2
temperature of the detector	$1.24 \cdot 10^{-7}$
temperature of G_2	$1.38 \cdot 10^{-7}$
temperature of G_0	$1.48 \cdot 10^{-7}$
temperature of the x-ray tube	$1.44 \cdot 10^{-7}$
mean value over all measured values	$1.49 \cdot 10^{-7}$
mean value starting with measurement values after 2 h 40 min	$1.8 \cdot 10^{-7}$

For the factors of higher order of the polynomial also the mean value of the parameters after 2 h 40 min is taken. In figure 5.12 and tables 5.8, 5.9 and 5.10 the fit-factors of second order are exemplarily shown. It can be observed in figure 5.12 that the course of the factors over time resembles also the course of the G_2 temperature. It might be advisable to also describe the course of the factors of higher order with the help of the G_2 temperature. Nevertheless, the factors of second order range on a very small scale of about 10^{-5} rad. Due to the inaccuracies of the fit it does not improve the reconstruction quality to describe factors of higher order with the help of G_2 temperature. In tables 5.8, 5.9 and 5.10 it can be seen that the goodness of fit is not much better or even worse than the χ^2 calculated with the mean value after 2 h 40 min.

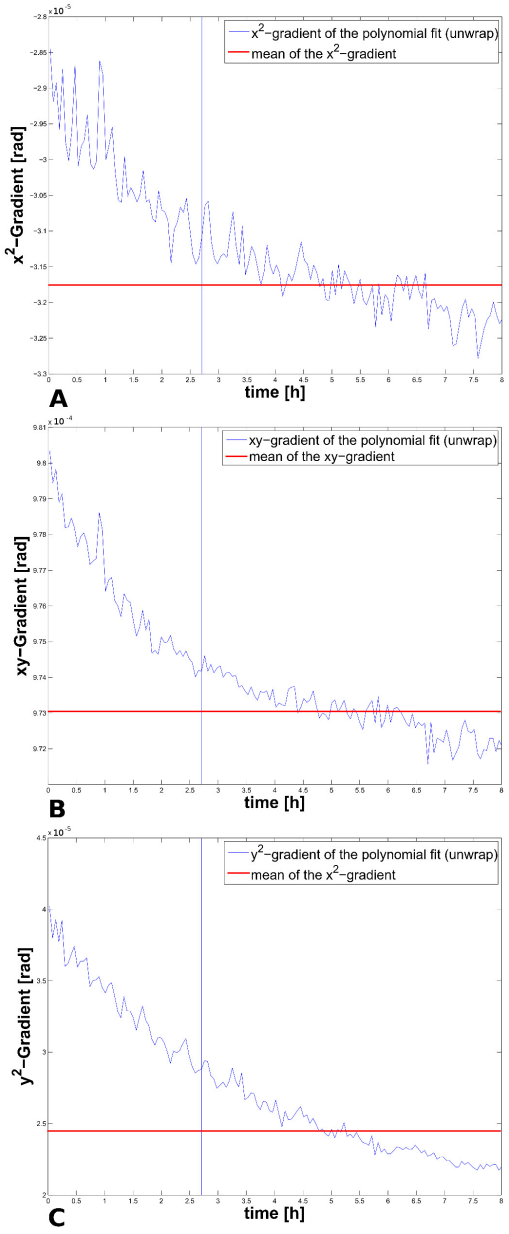

Figure 5.12: Mean values (red) of the x^2-gradient (A, blue), of the xy-gradient (B, blue) and of the y^2-gradient (C, blue). For calculating the mean value just the values measured after more than 2 h 40 min are taken into account as it is assumed that the setup is heated up after this time period.

Table 5.8: Goodness of fit of the x^2-gradient and the different temperatures/the mean

parameters to calculate the χ^2 value	χ^2
temperature of the detector	$1.20 \cdot 10^{-8}$
temperature of G_2	$6.03 \cdot 10^{-8}$
temperature of G_0	$5.34 \cdot 10^{-8}$
temperature of the x-ray tube	$1.07 \cdot 10^{-7}$
mean value over all measured values	$2.76 \cdot 10^{-8}$
mean value starting with measurement values after 2 h 40 min	$5.60 \cdot 10^{-9}$

Table 5.9: Goodness of fit of the xy-gradient and the different temperatures/the mean

parameters to calculate the χ^2 value	χ^2
temperature of the detector	$1.60 \cdot 10^{-9}$
temperature of G_2	$1.68 \cdot 10^{-9}$
temperature of G_0	$1.93 \cdot 10^{-9}$
temperature of the x-ray tube	$4.20 \cdot 10^{-9}$
mean value over all measured values	$3.89 \cdot 10^{-9}$
mean value starting with measurement values after 2 h 40 min	$4.89 \cdot 10^{-10}$

Table 5.10: Goodness of fit of the y^2-gradient and the different temperatures/the mean

parameters to calculate the χ^2 value	χ^2
temperature of the detector	$8.19 \cdot 10^{-8}$
temperature of G_2	$3.45 \cdot 10^{-8}$
temperature of G_0	$1.20 \cdot 10^{-7}$
temperature of the x-ray tube	$6.95 \cdot 10^{-7}$
mean value over all measured values	$8.57 \cdot 10^{-7}$
mean value starting with measurement values after 2 h 40 min	$1.81 \cdot 10^{-7}$

For reconstructing the phase images of the wedge, it is assumed that just one reference image is taken after 2 h 40 min. Just the temperature of G_2 is known to calculate the offset and the x-gradient of the polynomial describing the reference phase-map. Additionally, it is assumed that the mean values of the y-gradient and of the factors of higher order are constant over time to calculate the polynomial of the reference phase. Furthermore, the residuals have to be added to the polynomial as they are assumed to be constant over time. The reference phase-map calculated in this way is subtracted from the phase-map measured with the PMMA wedge in the beam path to achieve the differential phase-contrast image of the wedge.

5.2.2 Compensation of long-term drift effects in general

A more general approach to describe the long-term drifting effects is made in the following.
Again the general form of the phase-map is described by a polynomial fit. Additionally, it is presumed that a polynomial, fitted in the phase image and measured with an object in the beam is almost the same as a polynomial, fitted in the free-field phase and measured at the same time. Thus, it is supposed that the object information is mainly formed by high spatial frequencies. It can be assumed that the influences of the object on the phase do not affect the general form of the polynomial as long as the object does not shift the phase of the complete field of view in just one direction. The information about the object is predominantly contained in the residuals between the measured object phase and the polynomial fit $\phi_{\text{res,obj}}(x,y,t) = \phi_{\text{obj,unwrap}}(x,y,t) - \phi_{\text{obj,fit}}(x,y,t)$. That means that the residuals $\phi_{\text{res,obj}}(x,y,t)$ include the object information and the information about the inhomogeneities of the setup. Since the information about the inhomogeneity of the setup is time-independent, the object information can be calculated by subtracting the residuals of a reference phase measurement taken at any time: $\delta\phi_{\text{obj}}(x,y) = \phi_{\text{res,obj}}(x,y) - \phi_{\text{res,ref}}(x,y)$. Equation 5.1 summarizes the whole procedure.

$$\delta\phi_{\text{obj}}(x,y) = \phi_{\text{obj,unwrap}}(x,y,t) - \phi_{\text{obj,fit}}(x,y,t) - \phi_{\text{res,ref}}(x,y) \tag{5.1}$$

This method of calculating the object information without taking continuously new reference images will be referred to as Plane-Phase-Fit Method (PPF).

Applying the PPF, slow temporal changes of the object phase might be absorbed by the fitted polynomial. Since the information described by the polynomial is not considered for calculating the object information, low spatial frequency properties of the object are not reproduced. Thus, the PPF method acts like a high-pass filter. Edges in the phase-contrast image are pronounced and will be more easily recognizable.

5.3 Short-term drift effects

5.3.1 Correction algorithm for compensating short-term drift effects

To get information about the phase and visibility in each pixel, a phase-stepping is performed. Applying standard reconstruction, a sinusoidal curve is fitted in the

measured intensities of each detector pixel. In order to extract the correct phase, amplitude and offset of the sine, the phase-step positions $\kappa(n)$ of G_2 have to be known precisely. Reconstructing an image assuming wrong phase-step positions leads to artifacts in all three reconstructed imaging modalities. These artifacts are visible as a Moiré pattern. The Moiré pattern is caused by superposition of two periodical structures [52]. As the phase-step positions are not the same for each image, the superposing periodical structures differ between the images. Thus, the Moiré pattern is not stable and it is not the same in reference and object phase image. For this reason it does not cancel out, calculating the differential phase-contrast image. Hence, it is still visible in reconstructed phase images. This can be avoided by the knowledge of the accurate phase-step positions.
In general, it is assumed that all phase-step positions are distributed equidistantly over a predefined number of grating periods. During the imaging process vibrations, distortions and thermal influences on the setup lead to inaccuracies of these phase-step positions. Consequently, the assumption of equidistantly distributed phase-step positions is not valid anymore. Vargas et al. [53,54] proposed to perform a principal component analysis (PCA) of the measured intensities $I(n)$ in each pixel (x,y) to extract the phase information from randomly distributed interferograms. Pelzer et al. [43] transferred this algorithm to differential phase-contrast imaging in Talbot-Lau interferometry. The following assumptions and calculations are taken from the publications by Vargas et al. [53,54]:
The intensity $I(x,y,n)$ measured at each phase-step $n \in \{1,...,N\}$ in each detector pixel (x,y) can be described by

$$I(x,y,n) = a(x,y) + b(x,y)\cos(\phi(x,y) + \kappa(n)) \tag{5.2}$$

where $a(x,y)$ is the background intensity, $b(x,y)$ and $\phi(x,y)$ describe the periodic modulation of the intensity pattern and $\kappa(n)$ describes the phase-step position. Vargas et al. rewrite this equation as

$$I(x,y,n) = a(x,y) + b(x,y)\left[\cos(\phi(x,y))\cos(\kappa(n)) - \sin(\phi(x,y))\sin(\kappa(n))\right] \tag{5.3}$$

and group the terms as:

$$I(x,y,n) = a(x,y) + \alpha(n)I_c(x,y) + \beta(n)I_s(x,y) \tag{5.4}$$

with $\alpha(n) = \cos(\kappa(n))$, $\beta(n) = -\sin(\kappa(n))$, $I_c(x,y) = b\cos(\phi(x,y))$ and $I_s(x,y) = b\sin(\phi(x,y))$. In the following, Vargas et al. subtract the background intensity and

assume that $a(x,y) \simeq \frac{1}{N}\sum_{n=1}^{N} a(x,y,n)$ is the mean background intensity over all phase-steps. The PCA is performed with the background filtered intensity

$$\begin{aligned} I'(x,y,n) &= I(x,y,n) - a(x,y) \\ &= \alpha(n) I_c(x,y) + \beta(n) I_s(x,y). \end{aligned} \tag{5.5}$$

Therefore, the signal can be expressed as a linear combination of two signals. Vargas et al. assume that $I_c(x,y)$ and $I_s(x,y)$ are nearly linear independent if there is more than one Moiré fringe in the image. With the help of the PCA a coordinate transformation is performed to find the proper linear independent solution of this problem.
Regarding image reconstruction Vargas et al. propose to rewrite the matrix $I(x,y,n)$ of size $N_x \times N_y \times N$ into a two dimensional vector $I(z,n)$ of size $N_x \cdot N_y \times N$. The first step of the algorithm requires the covariance matrix C, which is calculated by

$$C(I(z,n),N) = \left(I(z,n) - \frac{1}{N}\sum_{n=1}^{N} I(z,n) \right) \left(I(z,n) - \frac{1}{N}\sum_{n=1}^{N} I(z,n) \right)^T. \tag{5.6}$$

In a second step, the diagonalisation of C is calculated numerically. Therefore, a singular-value-decomposition algorithm providing the transformation-matrix A is used.

$$\begin{aligned} D &= ACA^T \\ &= A \left(I(z,n) - \frac{1}{N}\sum_{n=1}^{N} I(z,n) \right) \left(I(z,n) - \frac{1}{N}\sum_{n=1}^{N} I(z,n) \right)^T A^T \\ &= YY^T \end{aligned} \tag{5.7}$$

The transformation matrix A rotates the measured intensity vectors in a new coordinate system with orthogonal axes, the principal components Y_i (with $i \in \{1, ..., \text{number of principal components}\}$).

Vargas et al. [54] also propose a possibility to calculate the phase-step positions from the principal components Y. It is assumed that, after reshaping the vector of intensities $I(n)$ and the vector of principal components Y to matrices $I(x,y,n)$ and $Y_i(x,y)$ of size $N_x \times N_y \times N$ and $N_x \times N_y$, new factors for linear combination can be calculated as follows

$$\begin{aligned}\alpha^*(x,y,n) &= \langle I(x,y,n), Y_1(x,y)\rangle \\ &= \sum_{x=1}^{N_x}\sum_{y=1}^{N_y} Y_1(x,y)I(x,y,n)\end{aligned} \tag{5.8}$$

and

$$\begin{aligned}\beta^*(x,y,n) &= \langle I(x,y,n), Y_2(x,y)\rangle \\ &= \sum_{x=1}^{N_x}\sum_{y=1}^{N_y} Y_2(x,y)I(x,y,n).\end{aligned} \tag{5.9}$$

$Y_1(x,y)$ and $Y_2(x,y)$ are the first two principal components of $Y_i(x,y)$. Using equations 5.8 and 5.9 the optimized and denoised intensity without the background intensity can be calculated as

$$I'^*(x,y,n) = \alpha^*(x,y,n)Y_1(x,y) + \beta^*(x,y,n)Y_2(x,y). \tag{5.10}$$

As it was defined that $\alpha(n) = \cos(\kappa(n))$, $\beta(n) = -\sin(\kappa(n))$, the new, optimized phase-step positions can be calculated with

$$\kappa^*(n) = \tan^{-1}\left(\frac{-\beta^*(n)}{\alpha^*(n)}\right). \tag{5.11}$$

Vargas et al. further optimize the phase-step positions by a least square minimization. In a first step, they assume that for each phase-step position the new, optimized intensity $I'^*(x,y,n)$ should be the same as the measured intensity $I'(x,y,n)$. Calculating the difference between measured and calculated intensity Vargas et al. also consider the DC-term $a^*(x,y)$.

$$\begin{aligned}S(x,y) &= \sum_{n=1}^{N}\left(a^*(x,y) + I'^*(x,y,n) - I'(x,y,n)\right)^2 \\ &= \sum_{n=1}^{N}\left(a^*(x,y) + \alpha^*(n)Y_1(x,y) + \beta^*(n)Y_2(x,y) - I'(x,y,n)\right)^2\end{aligned} \tag{5.12}$$

The least square minimization is performed by assuming that

$$\frac{\partial S(x,y)}{\partial a^*(x,y)} = 0, \qquad \frac{\partial S(x,y)}{\partial Y_1(x,y)} = 0, \qquad \frac{\partial S(x,y)}{\partial Y_2(x,y)} = 0. \tag{5.13}$$

Performing the minimization algorithm $Y_1(x,y)$ and $Y_2(x,y)$ can be optimized. With the help of these optimized principal components Vargas et al. also assume that the measured intensity $I'(x,y,n)$ in each pixel (x,y) should be the same as the the optimized intensity $I'^*(x,y,n)$. A second least square minimization is performed to optimize $\alpha^*(n)$ and $\beta^*(n)$.

$$\begin{aligned} S(n) &= \sum_{i=1}^{N_x \times N_y} \left(a^*(n) + I'^*(x,y,n) - I'(x,y,n)\right)^2 \\ &= \sum_{i=1}^{N_x \times N_y} \left(a^*(n) + \alpha^*(n)Y_1(x,y) + \beta^*(n)Y_2(x,y) - I'(x,y,n)\right)^2 \end{aligned} \tag{5.14}$$

with

$$\frac{\partial S(n)}{\partial a^*(n)} = 0, \qquad \frac{\partial S(n)}{\partial \alpha^*(n)} = 0, \qquad \frac{\partial S(n)}{\partial \beta^*(n)} = 0. \tag{5.15}$$

As $\alpha^*(n)$ and $\beta^*(n)$ are improved by this method new $\kappa^*(n)$ can be calculated. These two minimization algorithms are performed iteratively until the phase-step positions $\kappa_k^*(n)$ converge (with $k \in \{1, .., \text{maximal number of iterations}\}$). The convergence criterion of Vargas et al. is announced as

$$\max_n \mid \kappa_k^*(n) - \kappa_{k-1}^*(n) \mid < \epsilon. \tag{5.16}$$

with $\epsilon = 10^{-2}$ rad.

Henceforth, we use the described algorithm of Vargas et al. to reduce artifacts in the imaging modalities. For further reconstruction of phase, amplitude and offset the sinusoidal-fit is performed.

Calculating the principal components the order of the first two principal components Y_1 and Y_2 is random. Both components have the same weight calculating the signal as they represent the sine and the cosine component of the signal. This results in random phase-shift offsets of π between the single reconstructions of the phase image. As large objects are imaged with the help of a tiling-procedure it might happen that adjacent tiles of the phase-contrast image have different signs or even that the sign of the phase of the reference image differ from the sign of the phase of the object image. To reconstruct the phase-contrast image the residuals of one reference phase $\phi_{\text{res,ref}}$, as described in the paragraph 5.2, can be used. As these residuals are independent in time they should be the same in each tile of the reference measurement. Hence, the residuals $\phi_{\text{res,ref(m)}}$ (with $m \in \{1, ..., \text{number of reference images}\}$)

of each reference tile are calculated and compared to the residuals of a first reference tile $\phi_{\text{res,ref(1)}}$ by calculating the standard deviation over all pixel in the FoV of $\sigma^- = \text{std}\left(\phi_{\text{res,ref(m)}} - \phi_{\text{res,ref(1)}}\right)$ and $\sigma^+ = \text{std}\left(\phi_{\text{res,ref(m)}} + \phi_{\text{res,ref(1)}}\right)$. If $\sigma^+ < \sigma^-$ holds true, $\phi_{\text{ref(m)}}$ is multiplied by -1.

The analogue approach is used to examine the sign between object- and reference-phase. The standard deviation of $\sigma^-_{\Delta\phi} = \text{std}\left(\phi_{\text{obj(n)}} - \phi_{\text{ref(n)}}\right)$ and $\sigma^+_{\Delta\phi} = \text{std}\left(\phi_{\text{obj(n)}} + \Phi_{\text{ref(n)}}\right)$ are calculated. If $\sigma^+_{\Delta\phi} < \sigma^-_{\Delta\phi}$ holds true, $\phi_{\text{obj(n)}}$ is multiplied by -1.

5.3.2 Evaluation of the correction algorithm for high absorbing objects

To apply the PCA algorithm explained in subsection 5.3.1 it is necessary to be able to observe a Moiré pattern overlaying all image structures. With the help of this Moiré pattern it is possible to sort the phase-steps and to calculate the correct phase-step positions by using the PCA minimization algorithm. At edges of high absorbing objects the necessary Moiré pattern is superimposed by the sharp edge in the absorption. Thus, it is not possible for the algorithm to calculate the phase-step positions correctly.
In figure 5.13 A it can be seen that for nearly homogeneous absorption the superimposed Moiré frequency is apparent over the whole detector matrix even if the Moiré pattern is not homogeneous. In this case the interferometer is aligned. Two peaks of the Moiré pattern are recognizable. The right peak shows higher intesities than the left peak. This is due to inhomogneities of the setup. Nevertheless, the frequency of the Moiré pattern can be detected. Whereas for objects with large differences in absorption the Moiré pattern is superimposed by the edge (figure 5.13 C). In this case the superimposed Moiré frequency is almost not visible. The increase of the intensities in figure 5.13 C is due to the differences in absorption capacity of the object. The Moiré pattern should have the same frequency as in figure 5.13 A because the gratings of the interferometer are not moved between both acquisitions. It can be seen that the increase of the intensities due to the Moiré pattern in figure 5.13 A is nearly the same as increase of the intensities due to the superimposed edge in figure 5.13 C. Thus, the frequency of the Moiré pattern cannot be detected for the aligned interferometer. Therefore, the PCA minimization algorithm does not perfectly work.
By misaligning the interferometer the frequency of the Moiré pattern increases. For this, the grating G_1 is moved out of its optimal position. In figure 5.13 B and D G_1 is moved $-2\,\text{mm}$ out of its aligned position. In figure 5.13 B the same situation has been taken as in figure 5.13 A. The Moiré pattern is well recognizable and homogeneous over the whole detector matrix. Again the slight increase in the intensities on the right side due to inhomogeneities of the setup can be observed. In figure 5.13 D

the same object as in figure 5.13 C is placed in the beam path. In this case the Moiré pattern is well recognizable as it has not the same frequency as the edge. Therefore, it is not superimposed by the edge. Thus, the PCA minimization algorithm should work well in this case.

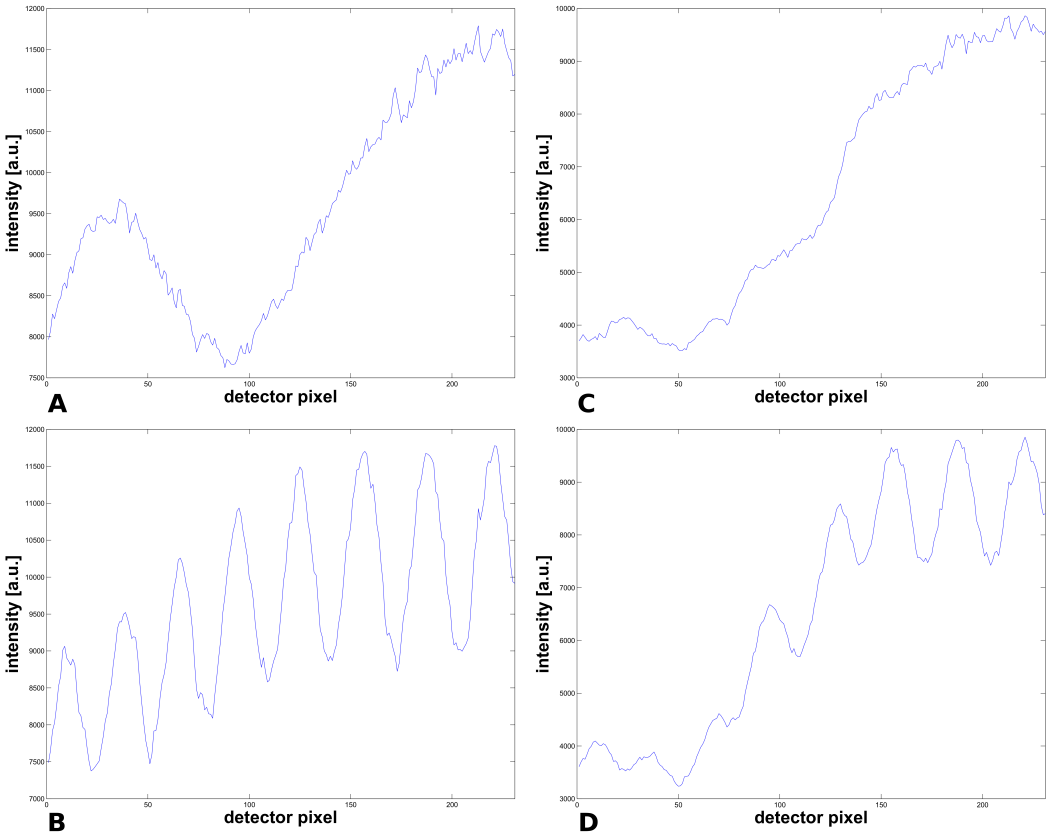

Figure 5.13: Lineplots of one phase-step over one detector row. A: Reference image taken with an adjusted interferometer. B: Reference image taken with a misaligned interferometer. G_1 is -2 mm out of the aligned position. C: Image taken with an adjusted interferometer with an object in the beam path causing an edge in the intensities around pixel 100. The Moiré pattern is superimposed by the edge. D: Image taken with a misaligned interferometer with an object in the beam path causing an edge in the intensities around pixel 100. G_1 is -2 mm out of the aligned position. Nevertheless, the Moiré pattern is visible due to the high frequency.

In this subsection it is investigated how to even reconstruct objects with edges with large differences in absorption using the PCA minimization algorithm. For this, a human vertebra is imaged in the high-energy setup. At the beginning of the measurement the Talbot-Lau interferometer is optimally adjusted. That means that the G_1 position is chosen with the aim to find the Moiré pattern with the lowest frequency, yielding the best visibility. In the theoretical case there would be one G_1 position for which no Moiré pattern would occur at all. This is not possible in reality

because of grating inhomogeneities and other external impacts. This low frequency Moiré pattern is superimposed by the edges of the vertebra. In the following G_1 is moved out of its optimal position in both directions in steps of 0.5 mm up to 2 mm. By moving G_1 the Moiré pattern becomes of higher frequency. The different Moiré pattern depending on the G_1 position can be seen in figure 5.14.

For all G_1 positions the conventionally reconstructed image using equidistantly distributed phase-steps and the image reconstructed using the PCA minimization algorithm are calculated. These images are evaluated visually concerning the image artifacts.
Nearly artifact free images using the PCA minimization algorithm can be achieved if G_1 is moved ± 1 mm and more out of its optimal position. This is due to the fact that the Moiré pattern gets more and more uniform moving G_1 out of its optimal position (see figure 5.14). In figures 5.15, 5.16 and 5.17 the images taken with an aligned interferometer and taken after moving G_1 out of its optimal position are shown. The images are reconstructed applying the conventional sine-fitting algorithm and applying the PCA minimization algorithm. It is not calculated the logarithm of the attenuation images and of the dark-field images. Thus, artifacts are shown more obviously. For the adjusted interferometer (figure 5.15) the conventional sine-fitting algorithm is better then the PCA minimization algorithm. This is due to the inhomogeneous, low frequency Moiré pattern which can be seen in figure 5.14 A. In this case the PCA minimization algorithm does not work correctly. In the images taken with the detuned interferometer (figure 5.16 and 5.17) no obvious additional artifacts can be observed in the images reconstructed with the PCA minimization algorithm. Artifacts which can be seen in the images reconstructed using the conventional sine fitting algorithm can be reduced or even removed by applying the PCA minimization algorithm. For best image reconstruction of objects with large differences in absorption the Moiré frequency has to be as uniform as possible over the detector matrix. It should be taken into account that the difference of the misaligned G_1 position to the optimal G_1 position should be as small as possible because visibility decreases by detuning the interferometer (figure 5.18 and 5.19).

In the following it is investigated if the image sensitivity especially of the dark-field image is lowered by detuning the interferometer compared to a conventionally reconstructed image taken with an adjusted interferometer. The visibilities of the a reference measurement are shown in figures 5.18 for the conventional sine-fitting reconstruction and 5.19 for the PCA minimization reconstruction. It can be seen that for the inhomogeneous Moiré pattern the visibility reconstructed with the PCA minimization algorithm shows artifacts. Especially for the adjusted interferometer

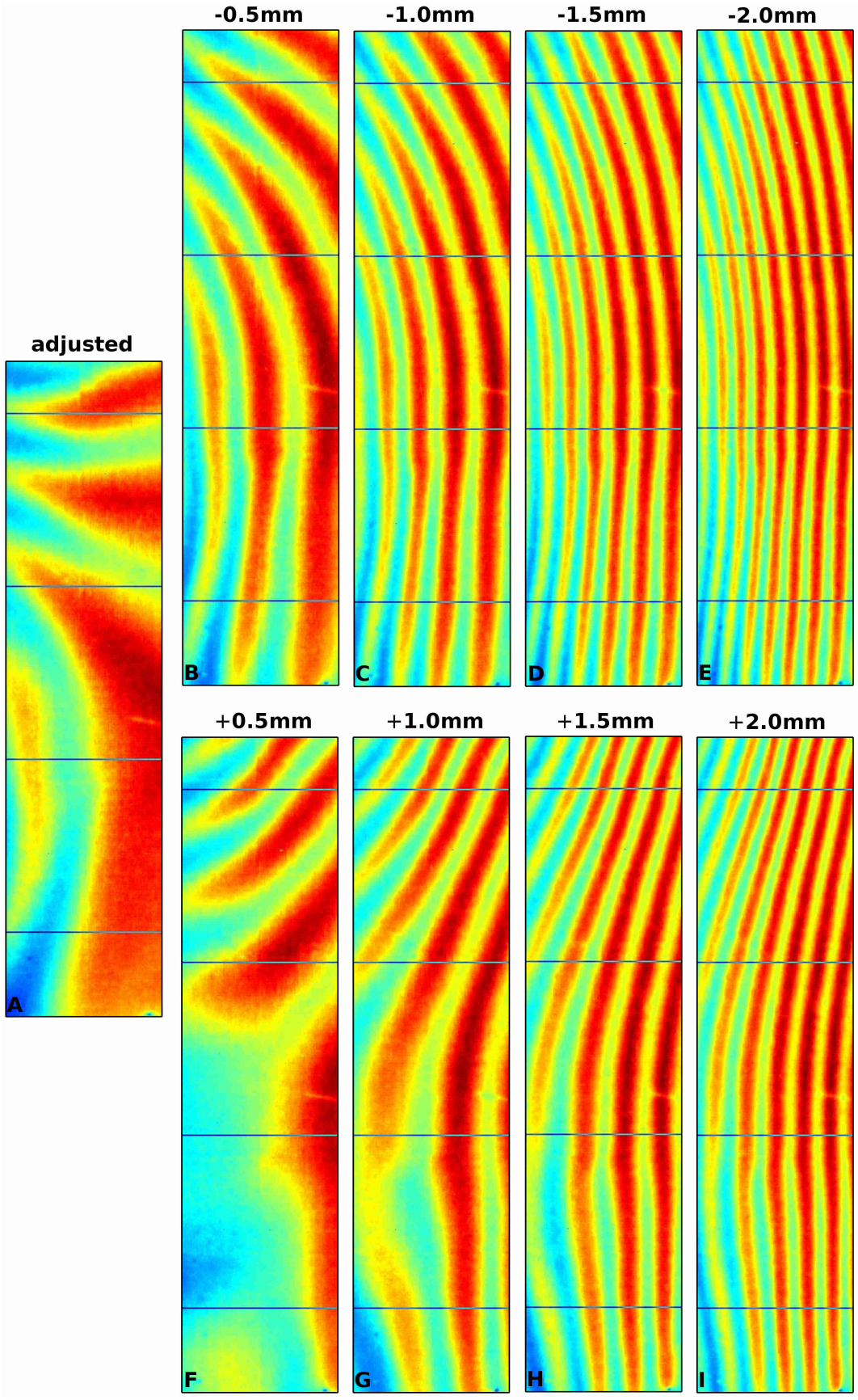

Figure 5.14: Moiré pattern at different G_1 positions. A: Adjusted interferometer. B: G_1 is -0.5 mm out of the aligned position. C: G_1 is -1.0 mm out of the aligned position. D: G_1 is -1.5 mm out of the aligned position. E: G_1 is -2.0 mm out of the aligned position. F: G_1 is $+0.5$ mm out of the aligned position. G: G_1 is $+1.0$ mm out of the aligned position. H: G_1 is $+1.5$ mm out of the aligned position. I: G_1 is $+2.0$ mm out of the aligned position

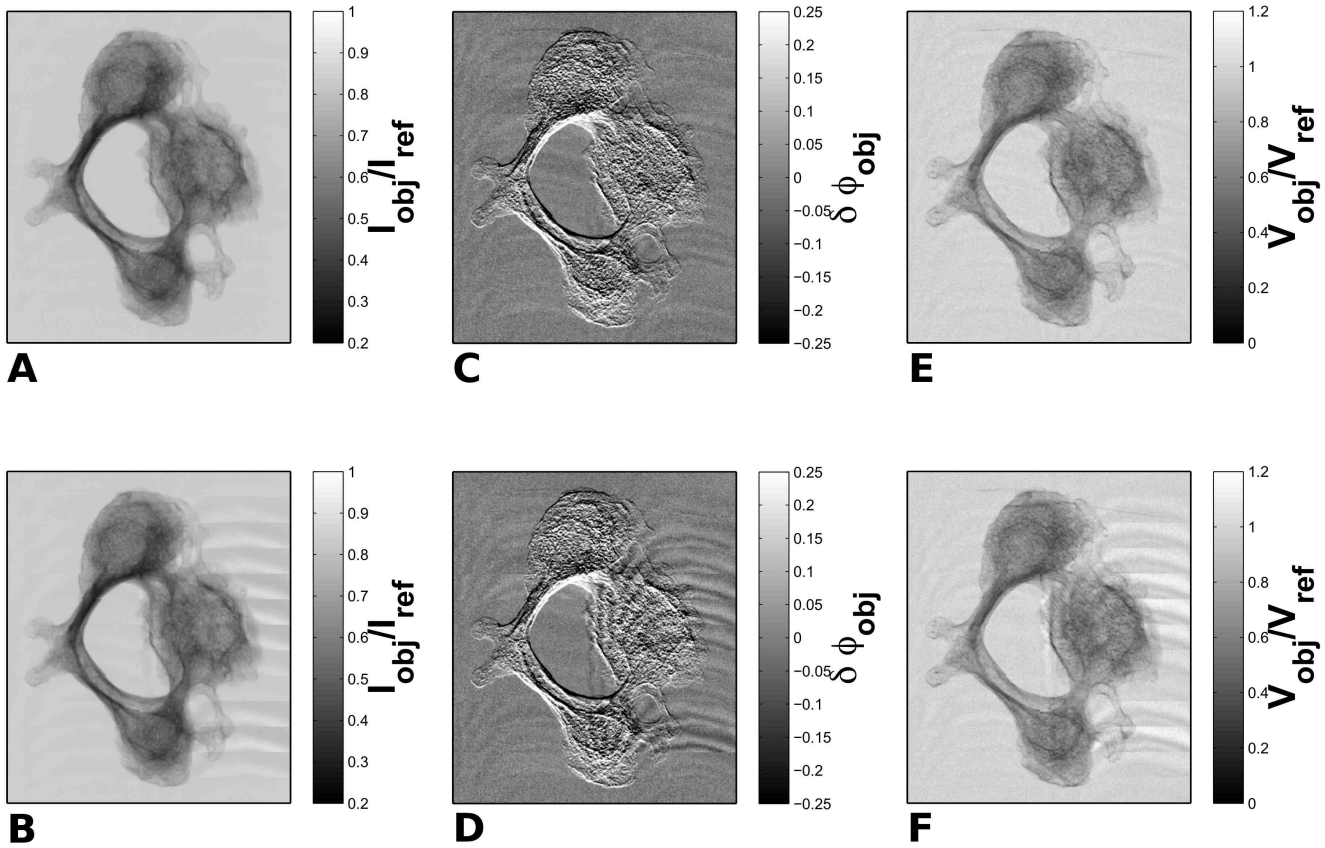

Figure 5.15: Attenuation image (A, B) without calculating logarithm to see the artifacts more clearly, differential phase-contrast image (C, D) and dark-field image (E, F) also without calculating logarithm for better visualization of the artifacts. The images on top of the figure (A, C, E) are reconstructed with the help of the conventional sine-fitting algorithm. The images on the bottom of the figure (B, D, F) are reconstructed using the PCA minimization algorithm. The images are taken with an adjusted interferometer. (Measurement parameters: tube voltage: 75 kV, tube current: 26 mA)

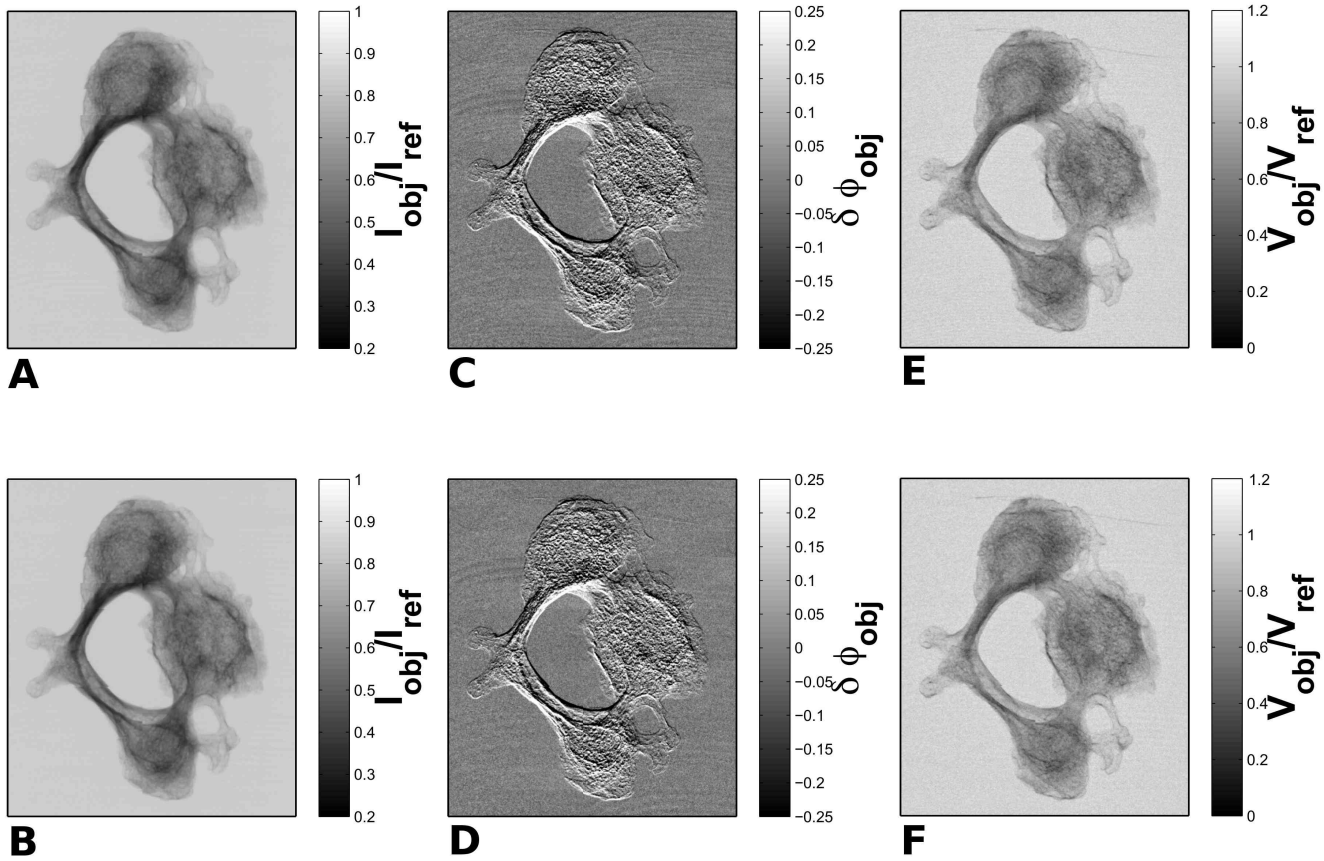

Figure 5.16: Attenuation image (A, B) without calculating logarithm to see the artifacts more clearly, differential phase-contrast image (C, D) and dark-field image (E, F) also without calculating logarithm for better visualization of the artifacts. The images on top of the figure (A, C, E) are reconstructed with the help of the conventional sine-fitting algorithm. The images on the bottom of the figure (B, D, F) are reconstructed using the PCA minimization algorithm. The images are taken with a detuned interferometer. $textrmG_1$ was moved -1 mm out of its optimal, adjusted position. (Measurement parameters: tube voltage: 75 kV, tube current: 26 mA)

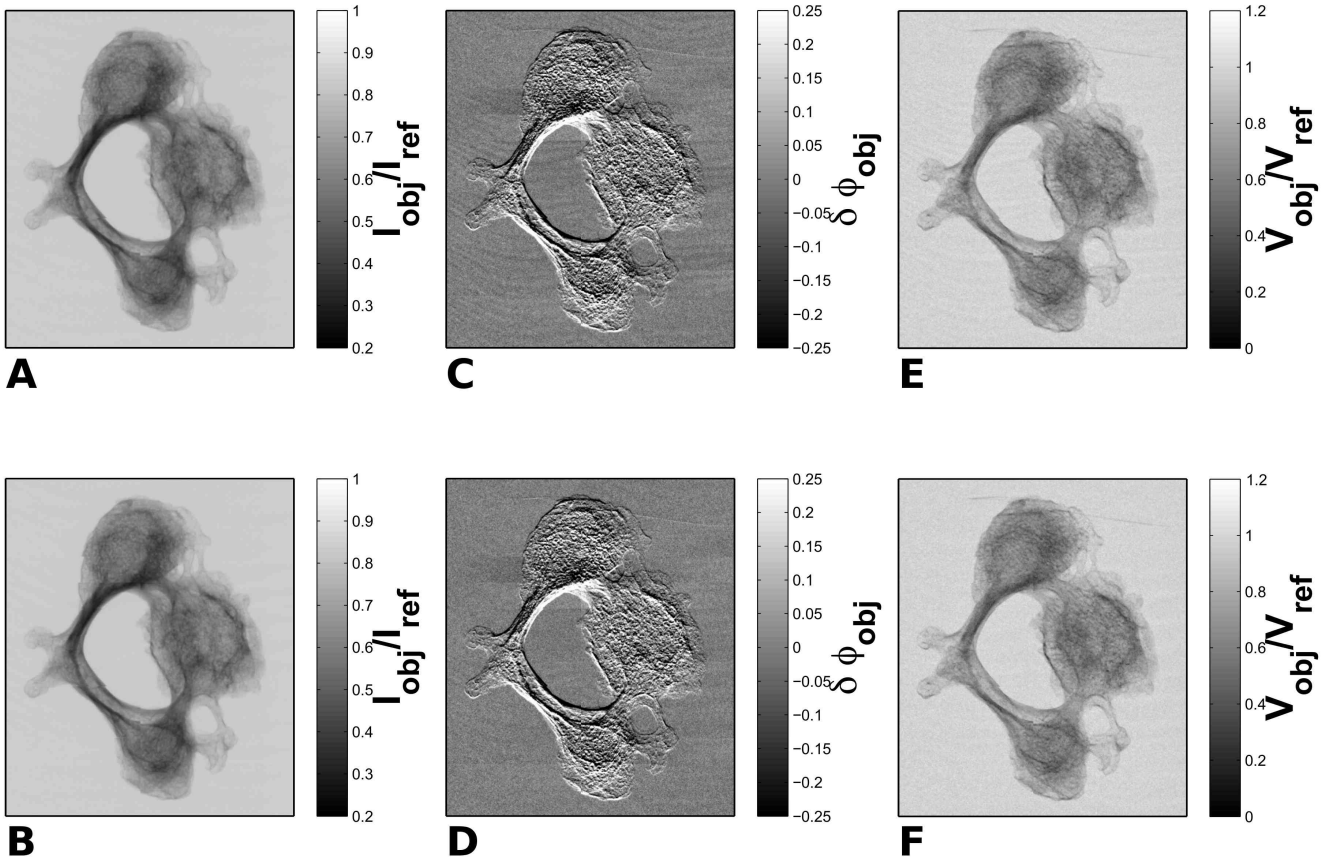

Figure 5.17: Attenuation image (A, B) without calculating logarithm to see the artifacts more clearly, differential phase-contrast image (C, D) and dark-field image (E, F) also without calculating logarithm for better visualization of the artifacts. The images on top of the figure (A, C, E) are reconstructed with the help of the conventional sine-fitting algorithm. The images on the bottom of the figure (B, D, F) are reconstructed using the PCA minimization algorithm. The images are taken with a detuned interferometer. $textrmG_1$ was moved $+1$ mm out of its optimal, adjusted position. (Measurement parameters: tube voltage: 75 kV, tube current: 26 mA)

(figure 5.19 A) and for the case that G_1 is moved $+0.5\,\text{mm}$ out of its optimal position (figure 5.19 F). In figure 5.14 A and F it can be seen that especially in these cases the Moiré pattern is completely inhomogeneous. Thus, the visibility cannot be reconstructed correctly with the help of the PCA minimization algorithm even if there is no object overlaying the Moiré pattern. In these cases the PCA minimization algorithm cannot detect the frequency of the Moiré pattern even for reference images. This leads to severe artifacts in the reconstructed images as can be seen in figure 5.15 reconstructing the images with the help of the PCA minimization algorithm. The maximum and the mean visibility is nearly always the same for both reconstruction techniques. By detuning the interferometer the visibility drops. Moving G_1 $\pm 1\,\text{mm}$ out of its optimal position, as it is necessary to be able to reconstruct useful images applying the PCA minimization algorithm, the mean visibility drops about 1%. The maximal loss in this case is about 3%. This may lead to a lower sensibility of the dark-field image. Thus, it might be that even if the dark-field image which is reconstructed with the PCA minimization algorithm and taken with the detuned interferometer shows less artifacts than the conventionally taken image, the sensitivity of the image might be too low to detect tiny lesions due to the loss in visibility by detuning the interferometer.

To assess the sensitivity loss caused by detuning the interferometer the conventionally taken image is compared to the image taken with the detuned interferometer and reconstructed using the PCA minimzation algorithm. Therefore, the quotient of the dark-field images taken with the detuned interferometer and reconstructed with the PCA minimization algorithm (figures 5.16 F and 5.17 F; associated visibility map in figure 5.19 C and G) and of the dark-field image taken with the aligned interferometer and reconstructed using the sine-fitting algorithm (figure 5.15 E; associated visibility map in figure 5.18 A) are calculated (figure 5.20 B: G_1 position moved by $-1\,\text{mm}$ and C: G_1 position moved by $+1\,\text{mm}$). The dark-field image shows the scattering properties of an object. Scattering is a randomized process. Thus, two dark-field images of an object are never exactly the same. Because of that, the quotient is not always 1 (figure 5.20). To be able to differentiate noise in the quotient due to statistical noise and noise due to the loss in sensitivity the quotient of two images taken with the adjusted interferometer and reconstructed with the conventional sine-fitting algorithm is shown in figure 5.20 A. All three images are nearly the same. No strutures are visible in figure 5.20 B and C. Thus, it can be assumed that all structural information of the dark-field image is measured even if the interferometer is detuned.

In table 5.11 the mean and the standard deviation of the images in figure 5.20 is shown. It can be seen that the mean and the standard deviation are nearly the same for all three images images. Thus, it assumed that the sensitivity loss by detuning

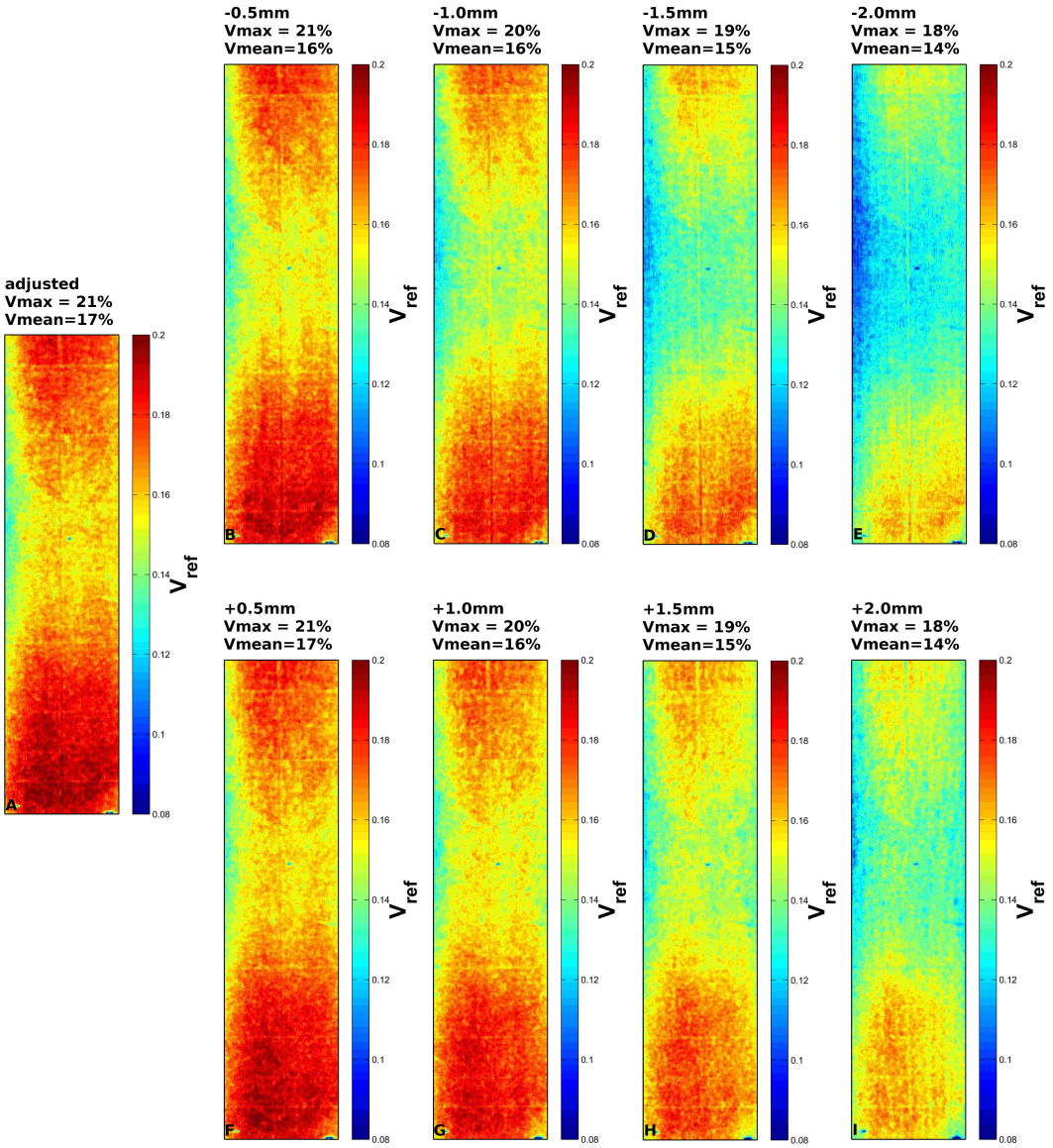

Figure 5.18: Visibilities of a reference measurement at different G_1 positions. The visibilities are reconstructed with the help of the sine-fitting algorithm. A: Adjusted interferometer. B: G_1 is -0.5 mm out of the aligned position. C: G_1 is -1.0 mm out of the aligned position. D: G_1 is -1.5 mm out of the aligned position. E: G_1 is -2.0 mm out of the aligned position. F: G_1 is $+0.5$ mm out of the aligned position. G: G_1 is $+1.0$ mm out of the aligned position. H: G_1 is $+1.5$ mm out of the aligned position. I: G_1 is $+2.0$ mm out of the aligned position

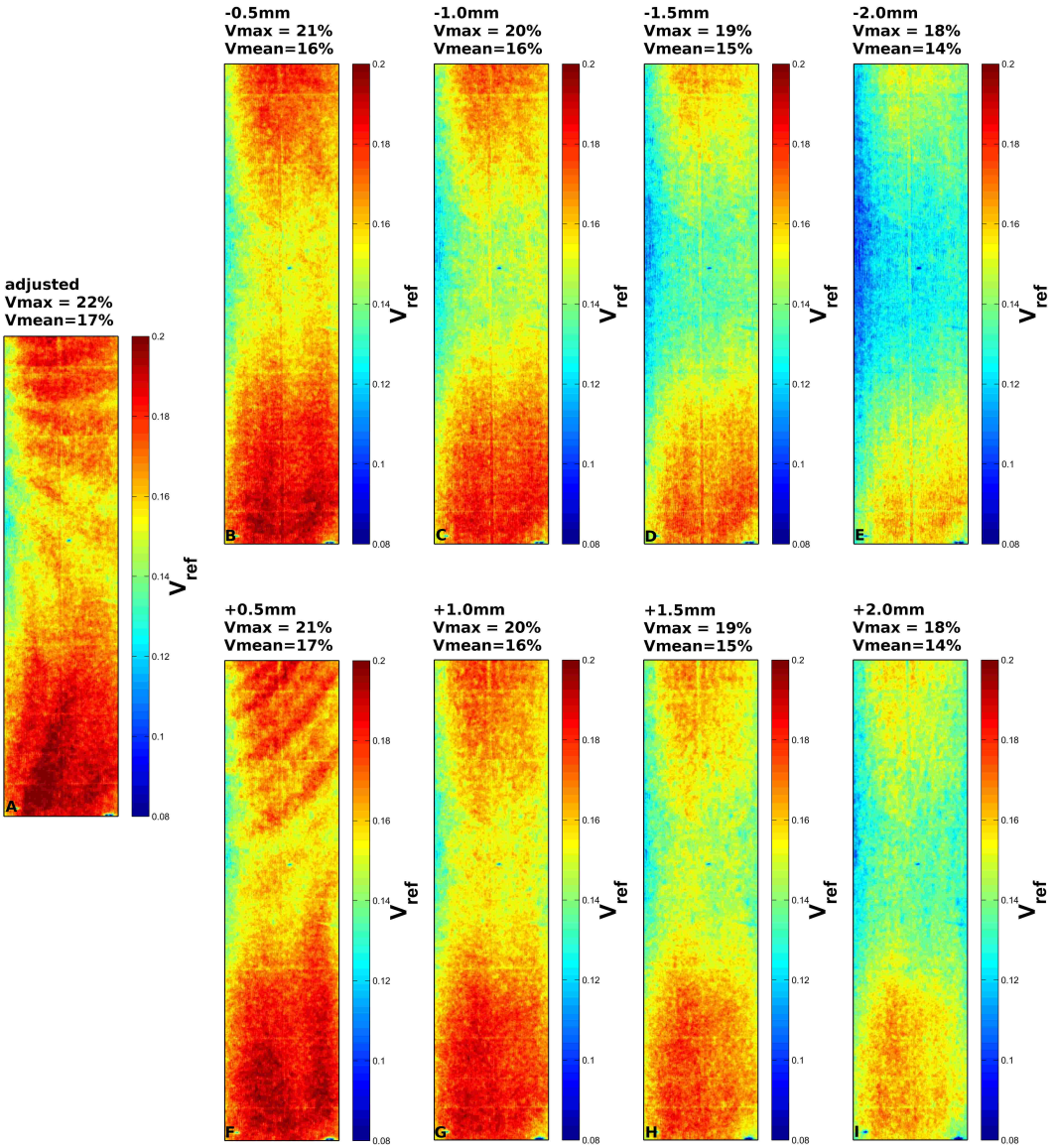

Figure 5.19: Visibilities of a reference measurement at different G_1 positions. The visibilities are reconstructed with the help of the PCA minimization algorithm. A: Adjusted interferometer. B: G_1 is -0.5 mm out of the aligned position. C: G_1 is -1.0 mm out of the aligned position. D: G_1 is -1.5 mm out of the aligned position. E: G_1 is -2.0 mm out of the aligned position. F: G_1 is $+0.5$ mm out of the aligned position. G: G_1 is $+1.0$ mm out of the aligned position. H: G_1 is $+1.5$ mm out of the aligned position. I: G_1 is $+2.0$ mm out of the aligned position

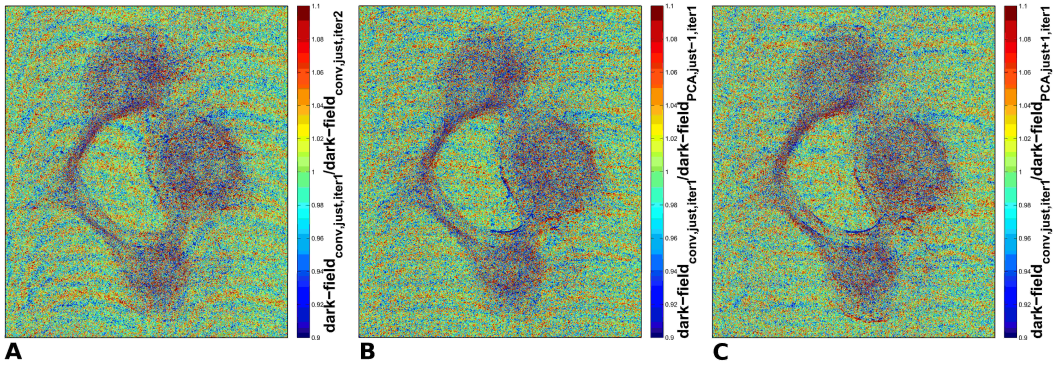

Figure 5.20: Assessment of the sensitivity of the interferometer after detuning it. A: Quotient of two dark-field images taken with the adjusted interferometer and reconstructed with the sine-fitting algorithm. B and C: Quotient of a dark-field image taken with the adjusted interferometer and reconstructed with the sine-fitting algorithm and of a dark-field image taken with an interferometer where G_1 is moved -1 mm (B) and $+1$ mm (C) out of its optimal position and reconstructed with the help of the PCA minimization algorithm.

the interferometer is not as severe as the artifacts caused by mechanical instabilities which can be removed by applying the PCA minimization algorithm.

Table 5.11: Mean and standard deviation of the quotient images in figure 5.20

	mean	standard deviation
figure 5.20 A	1.002	0.058
figure 5.20 B	1.001	0.059
figure 5.20 C	1.002	0.058

Chapter 6

Results

In the following the results of the four methods are presented. In the first part of this section the results concerning the long-term drift effects are shown. In the second part the results of the PCA minimization algorithm to compensate short-term drift effects are presented.

6.1 Long-term drift effects

6.1.1 Temperature drift effects

To evaluate the quality of the images reconstructed with the temperature dependent reconstruction algorithm (subsection 5.2.1) (figure 6.1 B, D and F) the conventionally reconstructed images are shown in figure 6.1 A, C, and E in comparison. To calculate these images the reference phase image taken right before taking the phase image of the PMMA wedge is subtracted from the phase image of the PMMA wedge. In figure 6.1 the reconstructed images after 2.75 h (A, B), 5.5 h (C, D) and 8 h (E, F) are shown. The structure of the differential phase-contrast image of the wedge can be explained by the high absorption inside the wedge. Thus, a large shift of the periodicity of the wavefront can be measured behind the wedge. Therefore, the values of the differential phase-contrast image do not only range between 0 and 2π and phase wrapping can be observed. This is the explanation for the structure which can be seen in the differential phase-contrast image behind the wedge. Nevertheless, the homogeneous background can be reconstructed.

It can be seen that the differential phase-contrast image of the wedge can be reconstructed with the help of the G_2 temperature and the mean values. Nevertheless, strong artifacts can be observed by using this reconstruction method. The free-field phase next to the wedge should be around zero, as it can be seen in the conven-

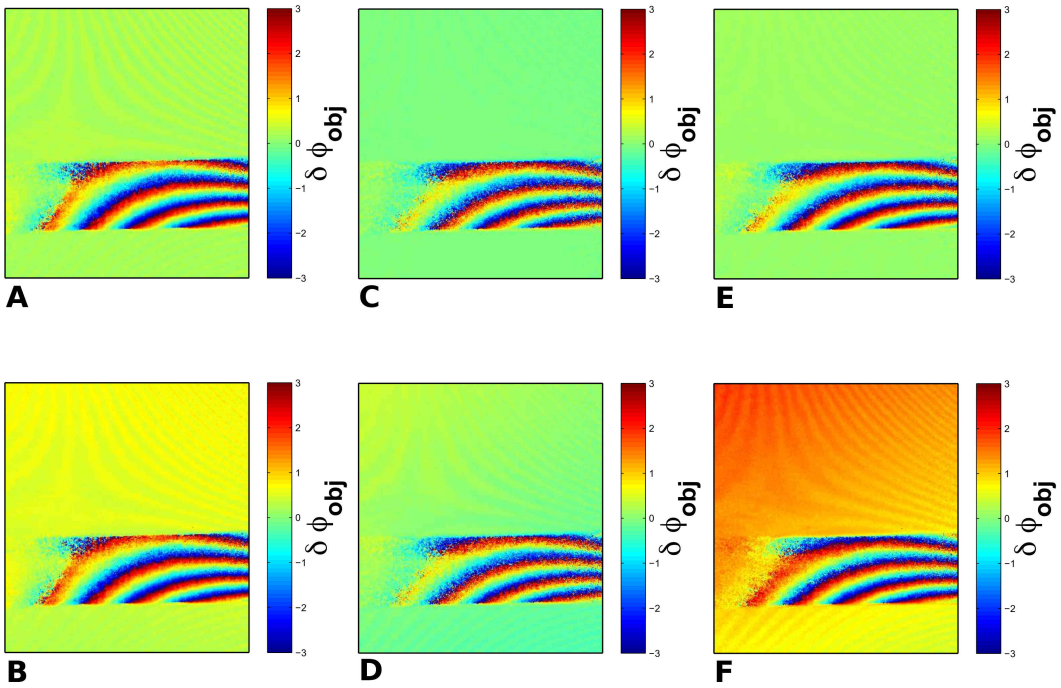

Figure 6.1: Differential phase-contrast images of the PMMA wedge taken 2.75 h (A,B), 5.5 h (C,D) and 8 h (E,F) after the measurement started. On top (A,C,E) the reference phase-map measured just before measuring the object phase-map is used to reconstruct the differential phase-contrast image. On the bottom (B,D,F) the reference phase-map is calculated using the temperature of G_2 and the mean value of the y-gradient and of the factors of higher order. (Measurement parameters: tube voltage: 40 kV, tube current: 50 mA)

tionally reconstructed images on top of figure 6.1. But the free-field phase of the differential phase-contrast images on the bottom of 6.1 is shifted and a gradient in the free-field phase can be observed. This is due to the deviations between the offset/the x-gradient calculated by the least square fit of the polynomial and of the offset/the x-gradient described by the temperature of G_2 (figure 5.11 A, B). Additionally, the mean values of the y-gradient and of the fit parameters of higher order do not describe the polynomial of the phase-map properly (figure 5.11 C). It has to be taken into account that even small deviations of the gradients in the order of 10^{-4} rad per pixel sum up over the whole detector matrix and lead to strong artifacts like gradients in the reference phase and to an inhomogeneous background over the whole image as they can be seen in figure 6.1 B, D and F. Furthermore, the Moiré artifacts are stronger in the differential phase-contrast image reconstructed using the temperature description, as can be especially seen in figures 6.1 B and F. Moiré fringes occur by superposing different periodical structures [52]. If the periodical structure of the reference phase is wrong and does not fit the measured periodical structure of the differential phase image with the object in the beam path, Moiré fringes can be observed in the resulting differential phase-contrast image. Thus, it seems that the temporal drifts of the reference phase are obviously not modeled sufficiently by the temperature.
Thus, it is not possible to reconstruct artifact free images using the presented method.

6.1.2 Compensation of long-term drift effects in general

To visualize and compare the results of the different reconstruction techniques the image of a human hand consisting of 70 tiles is taken. The PPF method was carried out to reconstruct the image with just one reference image. Without this reconstruction algorithm it is necessary to move the object repeatedly out of the beam during the measurement to take a reference image. In case of the presented measurement ten reference images were taken. The phase-contrast image of the human hand reconstructed using just one reference image is shown in figure 6.2 A. In this case object information is superimposed by phase drifting effects and tiny structures cannot be observed. For the differential phase-contrast image shown in figure 6.2 B the reference image has always been renewed after taking one row of (seven) object tiles. Hence, ten reference images were taken during the measurement. Figure 6.2 C shows the reconstruction of the same data set with the help of the PPF algorithm by using just one reference image. Thus, the measuring effort for the image in figure 6.2 C is the same as for the image in figure 6.2 A. But by using the PPF method no drifting artifacts are visible anymore. To investigate the difference between the results of both reconstruction algorithms, the quotient between the image reconstructed using the PPF method and the image reconstructed using the

standard sine fit method and ten reference images is calculated, which can be seen in figure 6.3. Dividing both images, structures which are the same in both images cancel out. Thus, only structures which are different in the images are preserved in figure 6.3. It can be observed that tiny structures like the bones in the metacarpus cancel out, dividing both reconstruction modalities as they are represented in both images. However, hard edges are still visible after dividing the images. This is due to the high-pass filtering effect of the PPF method. Large spacial frequency properties of the object are not represented in the image reconstructed using the PPF algorithm. Therefore, hard edges are pronounced using the PPF algorithm. This can be seen, comparing the images in figure 6.2.

To analyse the Moiré pattern in the images of figure 6.2 B and C, which appear as an indicator for the image quality, a Fast-Fourier-Transformation is performed (figure 6.4). The diagram on top of figure 6.4 shows the frequencies of the image reconstructed with the conventional sine-fitting algorithm. The diagram on the bottom of figure 6.4 shows the frequencies represented in the image which is reconstructed using the PPF algorithm. In both images the two peaks next to the central peak around the y-frequency of about $1500\,\frac{1}{\text{pixel}}$ and $-1500\,\frac{1}{\text{pixel}}$ can be identified as the frequencies of the Moiré pattern. It can be seen that the peaks caused by the frequencies of the Moiré pattern are less dominant in the PPF reconstructed images as in the frequency spectrum of the conventional reconstructed image. This is due to the fact that the Moiré pattern of the reference phase influences the differential phase image. The only components causing a Moiré pattern using the PPF reconstruction algorithm are the Moiré pattern of the object phase and the Moiré pattern of the residuals. Thus, there are less components which cause an amplification of the Moiré pattern. Instead, the PPF algorithm produces different, smaller frequency peaks. A grid-like pattern can be observed, in the FFT of the image calculated with the PPF method. This pattern can be explained by slight vibrations of the setup which causes vibrations of the residuals. As the residuals are caused inter alia by artifacts of the gratings, vibrations of these residuals lead to periodic, grid-like artifacts in the FFT image. These vibrations have been neglected in the PPF algorithm. The resulting artifacts might mainly be observed as noise in the images. With the help of a gauss filter the artifacts can be reduced as they are of high frequency. Such kind of image cleaning is not considered in this paper. Even in the FFT of the conventional reconstructed image the artifacts of the gratings can be seen as slight, vertical lines. These slight lines can be explained by imprecise phase-step positions as they can be reduced by applying the PCA minimization algorithm (see subsection 6.2.1).

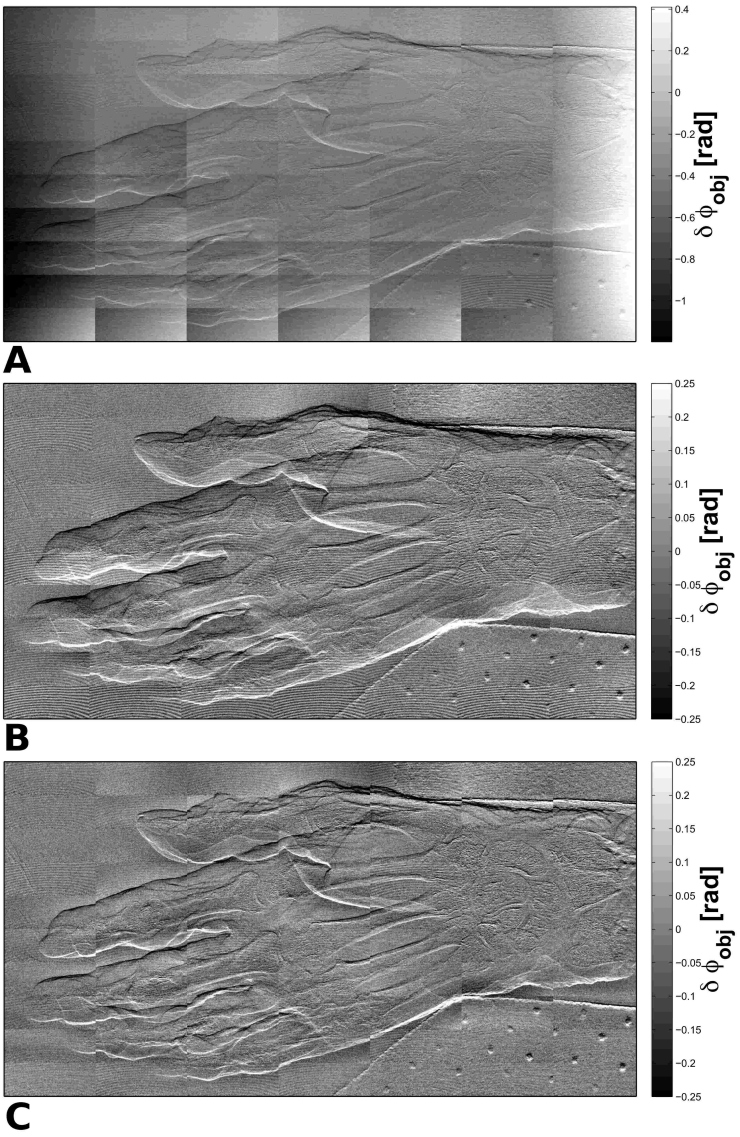

Figure 6.2: A: Differential phase-contrast image of a human hand reconstructed using just one reference image taken at the beginning of the measurement. B: Differential phase-contrast image of a human hand reconstructed with the sine fit method and 10 free field measurements. C: Differential phase-contrast image reconstructed with the help of the PPF algorithm (C). Like for image (A) just one free field measurement is necessary to reconstruct this image. The dotted structure in the bottom right corner of the images is caused by a sponge which has been used to fix the hand. (Measurement parameters: tube voltage: 75 kV, tube current: 15 mA, minimal dose in one tile: 0.17 mGy air kerma, maximal dose in one tile: 0.49 mGy air kerma)

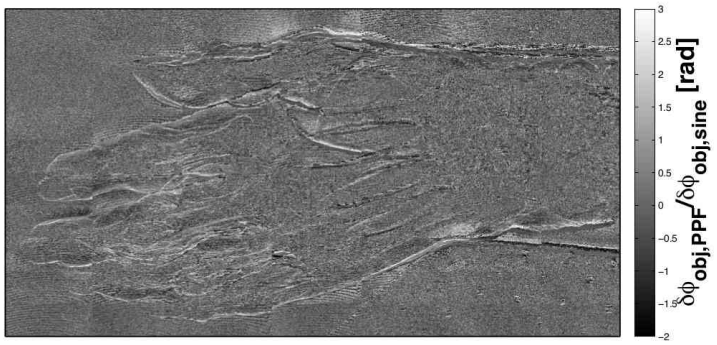

Figure 6.3: Differential phase-contrast image reconstructed with the help of the PPF algorithm (figure 6.2, bottom) divided by differential phase-contrast image of a human hand reconstructed with the sine fit method and 10 free field measurements (figure 6.2, top). (Measurement parameters: tube voltage: 75 kV, tube current: 15 mA, minimal dose in one tile: 0.17 mGy air kerma, maximal dose in one tile: 0.49 mGy air kerma)

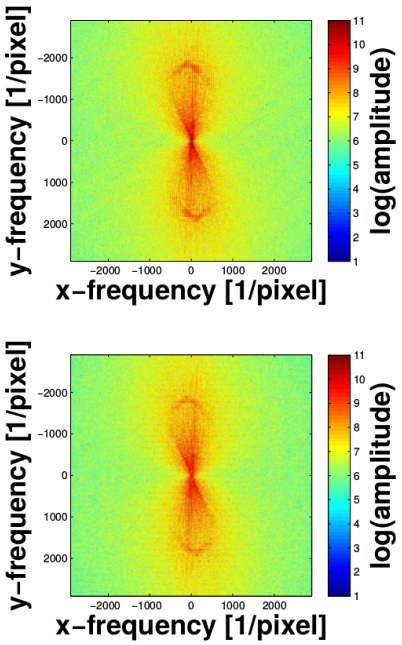

Figure 6.4: 2D FFT of the differential phase-contrast images of figure 6.2. Top: reconstruction with the help of the conventional sine-fitting reconstruction with ten reference images used. Bottom: reconstruction using the PPF algorithm with only one reference image used.

6.2 Short-term drift effects

6.2.1 Correction algorithm for compensating short-term drift effects

To analyze the effects of the PCA minimization algorithm the single phase-step positions are examined. As acquisition parameters eleven phase-steps have been chosen, equidistantly distributed over two periods (4π). These parameters have turned out as a good compromise between as short measurement times as possible on the one hand and the necessity to take many measurements to achieve a good image quality on the other hand. As the PCA algorithm arranges the phase-steps over 2π (figure 6.6) an unwrapping algorithm has been performed for better comparability of the two distributions of the phase-step positions. The phase-step positions reconstructed by applying the PCA minimization algorithm are not equidistantly distributed as it is shown in figure 6.5 A. To clarify the deviations a line fit has been performed. The red dots are not distributed on a straight line over the phase-step numbers. For example phase-steps number 8, 9 and 10 are no longer in line. Furthermore, instead of increasing phase-step positions the phase-step positions decrease after applying the PCA-minimization algorithm. The different stepping directions only affect the phase of the measured phase-stepping curves. They will be displaced relative to each other by 2π. The amplitude and the mean value of the curve do not change because of this shift. Hence, there is no effect on dark-field and attenuation images. The effect on the phase is caused by interchanging the first two principal components Y_1 und Y_2. How to handle the phase-shift of π is described in the subsection 5.3.1. For the sake of better comparability of the phase-step positions, in figure 6.5 B the phase-step directions of the two curves are adapted to each other by multiplying the PCA-phase-steps by -1. Again an unwrapping of the phase-step positions calculated using the PCA algorithm has been performed. The offset between the two curves in figure 6.5 B is caused by the definition of the zero point. In the standard reconstruction the first phase-step position is set as zero point. In PCA reconstruction the zero point is set randomly. As the choice of the zero point is the same for all pixel for one reconstruction method and just the differences between the values of each pixel are important, the choice of the zero point does not affect the resulting image.
In figure 6.5 C even the offset is corrected to be able to compare the deviations of both phase-stepping curves. By default the phase-stepping grating G_2 should have been moved by $\frac{4\pi}{11}$. It is obvious that after performing the PCA-minimization algorithm it is assumed that the grating is not moved in equidistant steps. The moved distances are sometimes smaller and sometimes larger than the predefined $\frac{4\pi}{11}$. These differences can be explained either by an imperfect positioning of the G_2 positioning system (blue positions) or by an imperfect reconstruction of the PCA method (red

positions). By calculating the χ^2 of the sine-fit in both phase-step positions, it can be observed that the mean of χ^2 is always smaller for the PCA reconstructed phase-step positions than for the equidistantly distributed phase-step positions. For the ten reference images the following χ^2 values (in arbitrary units) can be calculated: $\langle \chi^2_{\text{ref, PCA}} \rangle = 5.8 \pm 3.1$ and $\langle \chi^2_{\text{ref, equi.dist.}} \rangle = 11.7 \pm 5.7$. For the 70 object tiles the χ^2 (in arbitrary units) is: $\langle \chi^2_{\text{obj, PCA}} \rangle = 5.5 \pm 3.1$ and $\langle \chi^2_{\text{obj, equi.dist.}} \rangle = 6.5 \pm 3.5$. Thus, the mean quality of the fit is better for the PCA reconstructed phase-step positions than for the assumed equidistant phase-step positions.

In figure 6.6 it can be seen that the curve of the detector intensities over the phase-step positions is shifted by applying the PCA minimization algorithm. This is due to the different choice of the zero points. Using the PCA all curves are shifted the same compared to the standard reconstruction. Thus the shift is not visible in the resulting differential phase-contrast image. Nevertheless, for the sake of better comparability in figure 6.6 C the phase-stepping curve is offset corrected, multiplied by -1 and unwrapped. Thus, the deviations between both curves are best recognizable. No systematic mistake of the deviations can be observed. The deviations of both curves seem to be random.

Figure 6.7 shows the three imaging modalities of a chili. The image consists of only one tile. The images on top of the figure (A, C, E) are reconstructed using the standard reconstruction method. The images on the bottom (B, D, F) are reconstructed with the help of the PCA algorithm. The attenuation image is nearly the same for each reconstruction method. But in the differential phase-contrast image and the dark-field image it is obvious that the Moiré pattern in the images can be reduced by applying the PCA reconstruction algorithm. This can be most obviously seen in the top right corner of the differential-phase contrast and the dark-field image.

Figure 6.8 shows comparisons between the conventional sine-fitting reconstruction and the PCA minimization reconstruction for all three imaging modalities of a human hand. The image has been tiled and therefore, the acquisition time has been quite longer than for the chili. To be able to show more detail, the figures show a crop depicting the metacarpus of a human hand. Figures 6.8 A,C & E show the images reconstructed using the sine-fitting algorithm, figures 6.8 B, D & F the images reconstructed using the PCA minimization algorithm. The attenuation images do not differ between both reconstruction techniques. The offset of the fitted sine is obviously not heavily dependent on the different phase-step positions. But in the differential phase-contrast image and in the dark-field image the Moiré pattern is nearly completely removed. just one tile on the top right corner in the dark-field image still shows the Moiré pattern. This is caused by the different reasons the

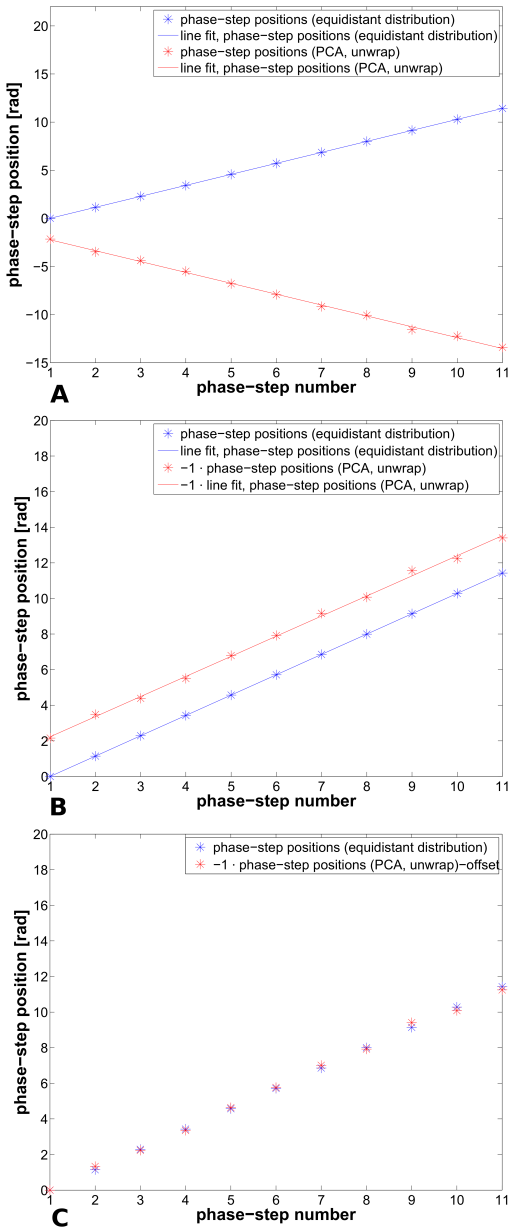

Figure 6.5: Phase-step positions as function of the number of phase-steps. Predefined phase-step positions over 4π (blue), reconstructed phase-step positions from the PCA minimization algorithm (red). A, B: A line fit has been performed to illustrate the derivation of an equidistant distribution of the phase-steps after applying the PCA algorithm. B: For better comparability the phase-step positions calculated using the PCA algorithm have been multiplied by -1. C: For better comparability the phase-step positions calculated using the PCA algorithm have been multiplied by -1 and corrected by the offset.

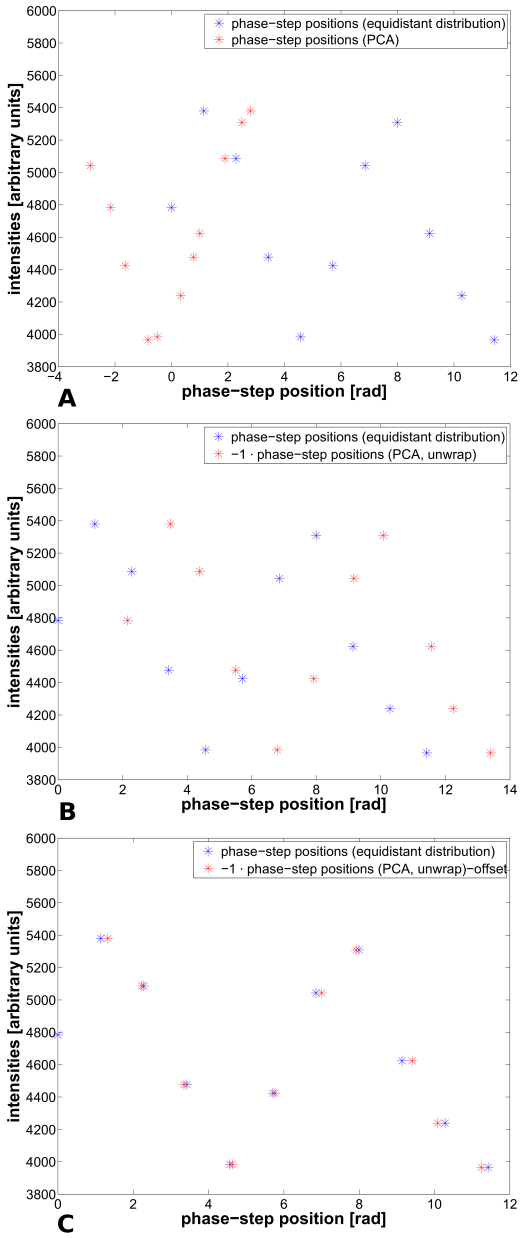

Figure 6.6: Measured intensity in arbitrary units in one pixel of the detector matrix of a reference measurement as function of the phase-step position. Predefined phase-step positions over 4π (blue), reconstructed phase-step positions from the PCA minimization algorithm (red). B: For better comparability the phase-step positions calculated using the PCA algorithm have been unwrapped and multiplied by -1. C: For better comparability the phase-step positions calculated using the PCA algorithm have been multiplied by -1 and corrected by the offset.

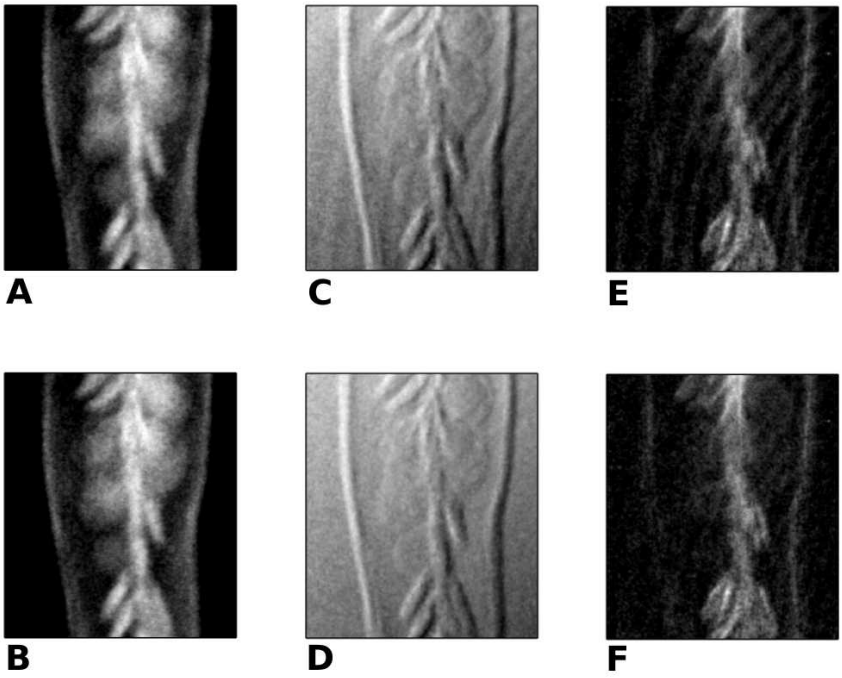

Figure 6.7: Attenuation image (A, B), differential phase-contrast image (C, D) and dark-field image (E, F) of a chili. Reconstruction with the help of the conventional sine-fitting algorithm (A, C, E), PCA minimization algorithm (B, D, F). (Measurement parameters: tube voltage: 60 kV, tube current: 50 mA)

Moiré pattern arises explained in the following. In the other tiles the Moiré pattern is due to the assumption of false phase-step positions. The Moiré pattern in the tile on the top right corner is caused by very short-term effects. The setup has not been stable during the acquisition of one phase-step. This effect cannot even be removed by the PCA minimization algorithm. But for all other tiles the image quality can be improved by applying the PCA minimization algorithm.

To analyse the Moiré pattern in the images of figure 6.8 a Fast-Fourier-Transformation of all images is performed (figure 6.9). The plots on top of figure 6.9 (A, C and E) show the frequencies of the three imaging modalities reconstructed with the conventional sine-fitting algorithm. The two peaks next to the central peak of the differential phase-contrast image and of the dark-field image around the y-frequency of about $1500\,\frac{1}{\text{pixel}}$ and $-1500\,\frac{1}{\text{pixel}}$ can be identified as the frequencies of the Moiré pattern. The plots on the bottom of figure 6.9 B, D and F show the frequencies represented in the images which are reconstructed with the help of the PCA minimization algorithm. Regarding the frequency spectra of the attenuation images, both images are completely the same. Thus, the PCA minimization algorithm does not affect the attenuation image and the information of the attenuation image is preserved. Furthermore, it can be seen that the frequency spectra of the differential phase-contrast images only differ considering the frequency peaks caused by the Moiré pattern. These peaks can be reduced by using the PCA without modifying the rest of the frequency spectrum. In the frequency spectrum of the dark-field image reconstructed with the help of the PCA minimization algorithm, the peaks of the Moiré pattern are almost removed. Like for the differential phase-contrast image the rest of the frequency spectrum is not affected by the PCA minimization algorithm. In the frequency spectra of the conventionally reconstructed images slight vertical lines can be observed. This can be most clearly seen in the frequency spectra of the differential phase-contrast image (figure 6.9 C) and of the dark-field image (figure 6.9 E). These lines can be explained by grating inhomogeneities as they are perpendicular to the grating bars. Due to the inaccurate phase-step positions, the positions of the inhomogeneities differ between the reference measurement and the measurement with the object in the beam-path. The resulting artifacts can be observed as lines in the frequency spectrum. Applying the PCA minimization algorithm these artifacts can be reduced as the phase-step positions are adjusted. Thus, the lines are less visible in the frequency spectrum of the image reconstructed using the PCA minimization algorithm (figure 6.9 D and F).

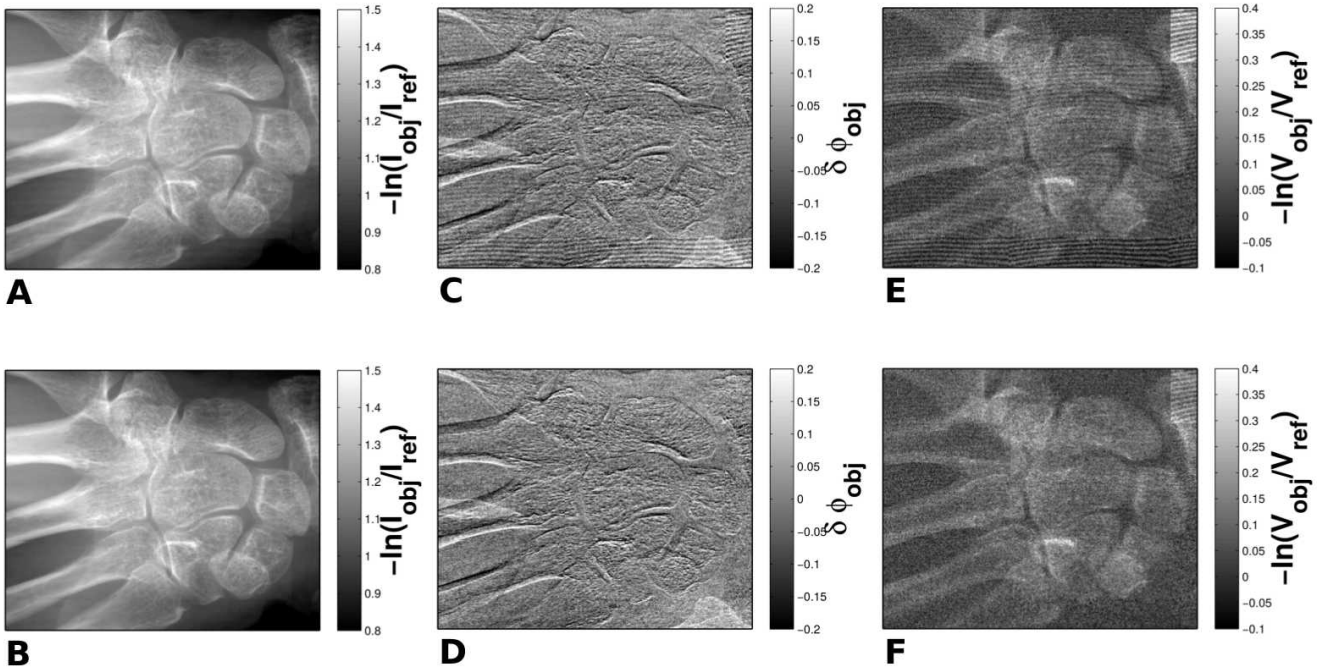

Figure 6.8: A&B: Attenuation images of the metacarpus of a human hand. C&D: Differential phase-contrast images of the metacarpus of a human hand. E&F: Dark-field images of the metacarpus of a human hand. Reconstruction with the help of the conventional sine-fitting reconstruction (top, A, C & E), PCA minimization algorithm (bottom, B, D & F). For all image reconstructions ten reference images were taken. Thus, the reference image has been always renewed after seven object tiles. (Measurement parameters: tube voltage: 75 kV, tube current: 15 mA, minimal dose in one tile: 0.17 mGy air kerma, maximal dose in one tile: 0.49 mGy air kerma)

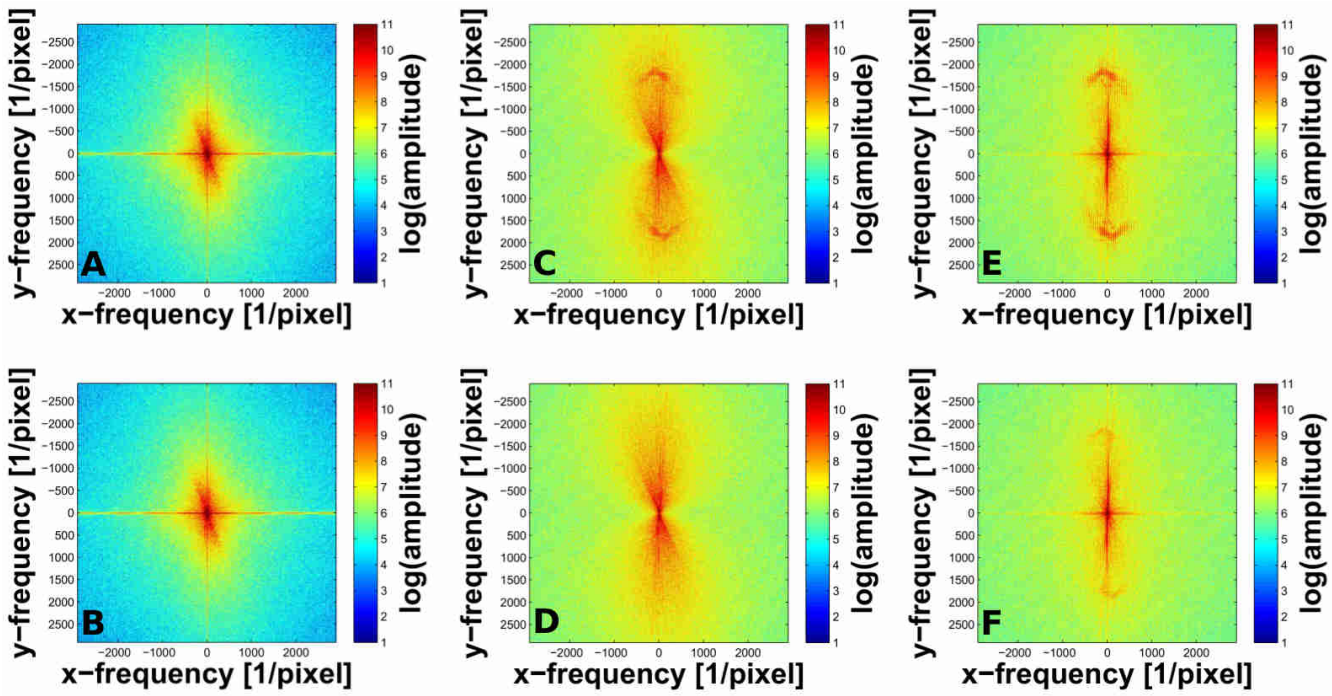

Figure 6.9: 2D FFT of the images of figure 6.8. A&B: 2D FFT of the attenuation images. C&D: 2D FFT of the differential phase-contrast images. E&F: 2D FFT of the dark-field images. Reconstruction with the help of the conventional sine-fitting reconstruction (top, A, C & E), PCA minimization algorithm (bottom, B, D & F).

6.2.2 Evaluation of the correction algorithm for high absorbing objects

To observe the influence of high absorbing objects on both reconstruction methods, images of a human knee (ex-vivo) were taken. As it is assumed that large differences in attenuation lead to a loss of correlation of the pixel, one image is taken with an aligned interferometer and a second image is taken with a misaligned interferometer. If the interferometer is misaligned the superimposed Moiré fringes are of higher frequency and are more dominant in the image. Thus the correlation of the pixel can be improved. The Moiré pattern of the aligned and of the misaligned interferometer are shown in figure 6.10. It can be seen that for the aligned interferometer nearly any Moiré fringes are visible. Whereas for the misaligned interferometer the Moiré pattern is of high frequency and homogeneous.

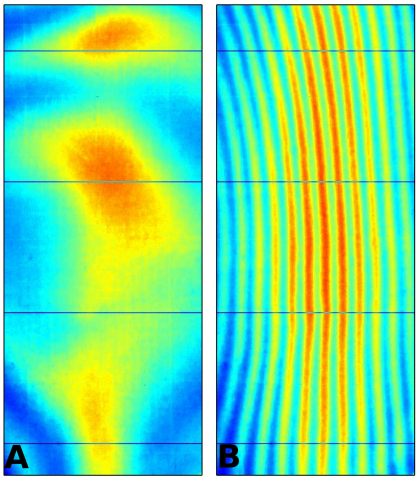

Figure 6.10: Moiré pattern of one phase-step of a reference measurement for the aligned interferometer (A) and for the misaligned interferometer (B).

The mean visibility is lowered by detuning the interferometer by about 2% (figure 6.11). Like for the reconstruction of the human vertebra it can be observed that for the aligned interferometer the Moiré frequency is not obvious enough to use the PCA minimization algorithm. As there is no periodic structure observable at all for the aligned interferometer even the free field images cannot be reconstructed using the PCA minimization algorithm. Therefore, the reference visibility reconstructed using the PCA minimization algorithm shows artifacts (figure 6.11 B). In contrast, the visibility taken with the misaligned interferometer and reconstructed using the PCA minimization algorithm shows no artifacts (figure 6.11 D).

Figure 6.12 shows the effect of large differences in attenuation of images taken with aligned and with misaligned interferometers and reconstructed using the PCA algorithm. It can be seen that the images taken with the aligned interferometer

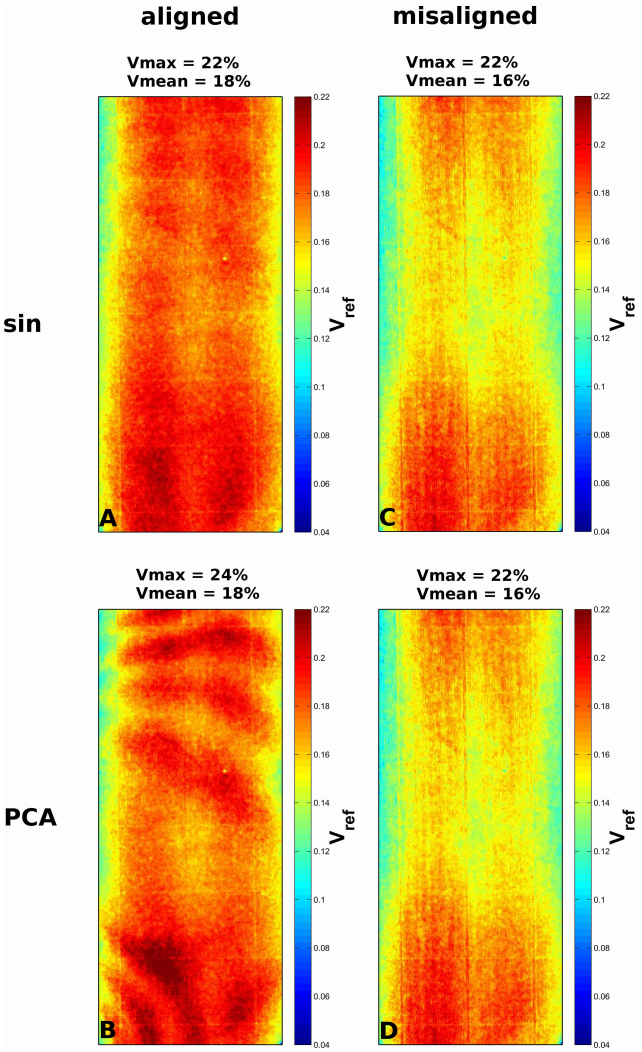

Figure 6.11: Visibility maps of a reference measurement of the human knee. The visibility maps are taken with an aligned interferometer (A, B) and with a misaligned interferometer (C, D). Each measurement is reconstructed with the conventional sine-fitting algorithm (A, C) and with the PCA minimization algorithm (B, D).

(figure 6.12 A, C, E) show serious artifacts. Especially in the attenuation and the dark-field image tiles with large differences of the attenuation coefficients are not reconstructed correctly. But also in the phase-contrast image of these tiles a more conspicuous Moiré pattern can be seen. By misaligning the interferometer (figure 6.12 B, D, F), these artifacts can be completely removed. Even tiles with large differences in attenuation can be reconstructed correctly with the help of the PCA algorithm.
It should be noted that for the images (A, C, E) the knee has been rotated by 90 degrees relative to the gratings, compared to images (B, D, F) in figure 6.12. This is due to imaging routines of other projects. Therefore, the sensitivity for the differential phase is also rotated by 90 degrees between image C and D in figure 6.12. Thus, in image C vertical edges are pronounced and in image D horizontal edges are pronounced. This is not due to the reconstruction algorithms or the alignment of the interferometer, but only due to the orientation of the knee relative to the grating bars. This explains the different impressions of the differential phase-contrast image but has no impact on the comparison of reconstruction of images taken with an aligned and with a misaligned interferometer.

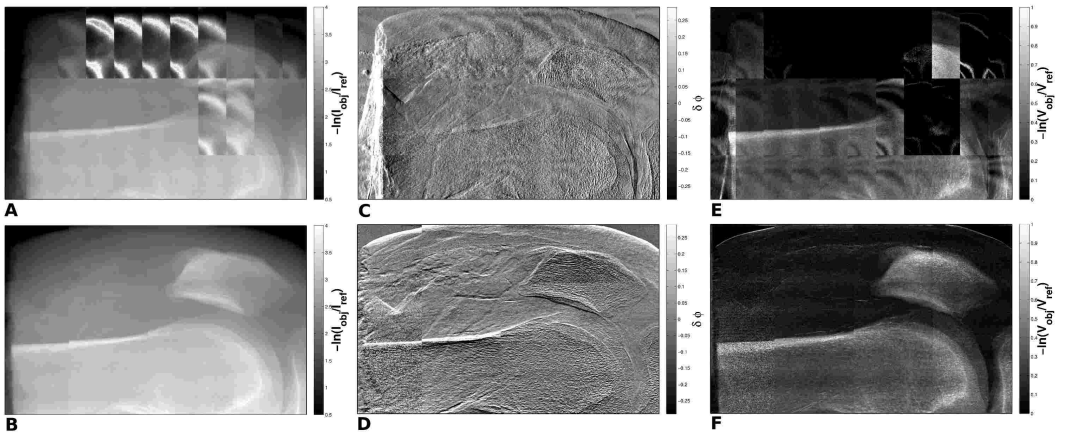

Figure 6.12: Attenuation image (A, B), differential phase-contrast image (C, D) and dark-field image (E, F) of a human knee (ex-vivo). The patella and the femur are depicted. A, C, E: Images are taken with an aligned interferometer. B, D, F: Images are taken with a misaligned interferometer. The images are reconstructed using the PCA algorithm. (Measurement parameters: A, C, E: tube voltage: 70 kV, tube current: 28 mA, minimal dose in one tile: 0.2 mGy air kerma, maximal dose in one tile: 4.2 mGy air kerma and B, D, F: Measurement parameters: tube voltage: 70 kV, tube current: 28 mA, minimal dose in one tile: 0.2 mGy air kerma, maximal dose in one tile: 4.1 mGy air kerma)

It can be seen that after misaligning the interferometer even the image of a human knee can be reconstructed without any artifacts. Thus, with the help of the PCA minimization algorithm it is possible to rearrange the phase-step positions for the

misaligned interferometer. Therefore, artifacts like they could be observed for the chili (figure 6.7) and for the human hand (figure 6.8) can be avoided. Additionally, no new artifacts occur due to edges in absorption. Consequently, it is possible to improve image quality for all objects, even for high absorbing objects by misaligning the interferometer and applying the PCA minimization algorithm.

Chapter 7

Discussion

7.1 Long-term drift effects

7.1.1 Temperature drift effects

It can be seen that it is possible to reconstruct a differential phase-contrast image with the knowledge of the temperature of G_2. Nevertheless, the image quality is not good and the images cannot be used for detection of very tiny lesions as severe artifacts occur in these images. The deviation between the calculated parameters of the least square fit and the parameters described by the temperature change of G_2 might be due to inaccurate temperature measurement. Thus, this reconstruction method possibly can be improved by using more sensitive temperature sensors which can be better mounted on the grating. Another reason can be the mechanical instability of the setup which is not considered in this reconstruction method. Additionally, systematic mistakes like different starting points of the phase-stepping are not taken into account. Vibrations or other external impacts on the setup are also not considered.
Hence, it is not usable to reconstruct differential phase-contrast images by just measuring the temperature of G_2, taking the mean of some parameters and considering it for generally valid. There are to many degrees of freedom to use just the G_2 temperature to describe the behavior of the reference phase-map over time. Perhaps it might be improved by considering more external impacts than the temperature and by improving the temperature measurement itself. But it will be a complex process to find all influencing variables and to measure them all with sufficient precision.

7.1.2 Compensation of long-term drift effects in general

It can be shown that it is possible to reconstruct an useful and meaningful image based on just one reference image. Relevant anatomic structures are visible (figures 6.2 and 6.3). The frequency spectra of the conventional sine-fitting reconstruction method and of the PPF method only differ concerning the Moiré frequency peaks. These can be reduced in amplitude by performing the PPF method. Thus, the image artifacts caused by the Moiré pattern can be slightly reduced by performing the PPF algorithm without further image processing (figure 6.4).
Slight artifacts occur because of the vibration of the residuals due to the vibration of the setup. This causes additional noise in the images. The additional noise does not lower the image quality as much as all structures are still visible and the frequency spectra are nearly similar.
All drift effects independent of their origin can be compensated by using the PPF method. It is not necessary to detect the origins of the drift effects and to measure the impacts separately like in the previously described attempt to describe the drift effects measuring the G_2 temperature. Thus, the PPF method is easier to handle and is independent of additional measurement inaccuracies.
The PPF methods has the advantage that instead of moving the object several times out of the setup, just one reference image is needed for a whole of 70 tiles. As an advantage, the object movement is minimized as it stays inside the setup during the whole time of the measurement. For a clinical workflow a reference image would be needed once per several hours only.
Further measurements on a C-arm setup have shown that it is possible to reconstruct even for this setup images with the help of the PPF method. Due to mechanical distortions of the C-arm the residuals are shifted by rotating the C-arm. Therefore, it is necessary to take the residuals for each rotation angle. These residuals show also a long-term stability like for all other setups. Thus, the PPF method is suitable independent of the setup.

7.2 Short-term drift effects

7.2.1 Correction algorithm for compensating short-term drift effects

Reconstructing images with the help of the PCA algorithm of Vargas et al. [53, 54] the knowledge of the phase-step positions is not necessary. As in clinical and other setups, which are integrated in work processes, it cannot be ensured that the setup is stable like on an optical stage. This is an important feature regarding the integration of phase-contrast imaging in work processes. Errors in the presumed phase-step

positions caused by vibrations and distortions of the setup can be corrected with the help of the PCA minimization algorithm. Figure 6.8 shows that the Moiré pattern is reduced by applying the PCA minimzation algorithm. The related artifacts in differential phase-contrast images and dark-field images can be significantly reduced or even removed. Especially in dark-field images this has a great impact on image quality. With the help of the PCA it is possible to reconstruct the three images of Talbot-Lau interferometry. In figure 6.9 the frequency spectra of the three imaging modalities shown in figure 6.8, reconstructed with the help of the PCA minimization algorithm of Vargas et al. [53,54] and reconstructed with the help of the conventional sine-fitting algorithm are shown. It can be seen that the frequency of the Moiré pattern can almost be removed in the differential phase-contrast image and in the dark-field image by applying the PCA minimization algorithm. The rest of the frequency spectrum is not affected by the PCA minimization algorithm. Thus, the imaged information is the same for both reconstruction techniques and just the image artifacts are removed.

7.2.2 Evaluation of the correction algorithm for high absorbing objects

It was observed that the image artifacts caused by the Moiré pattern can be removed by improving the preciseness of the phase-step positions using the PCA algorithm (e.g. figure 6.7). The Moiré pattern is caused by two different periodic pattern overlaying each other. As the accuracy of the phase-step positions is improved the differences between the Moiré pattern of the reference and of the object image data can be reduced. Thus, the periodic structures of both images are the same and any Moiré pattern can be observed in the reconstructed images.
Reconstructing images with large differences in attenuation using the PCA algorithm in figures 5.15, 5.16, 5.17 and 6.12 it is obvious that a high frequency Moiré pattern is needed to be able to reconstruct the attenuation and the dark-field images of tiles with large attenuation differences. The lineplots (figure 5.13, bottom) show that correlation in one detector row is lost for edges in the intensity if the Moiré frequency is too low. This is due to the fact that the period of the superimposed low frequency Moiré pattern is not apparent as the edge of the object superimposes all other structures in an intensity measurement. But the Moiré pattern is necessary to correlate the pixel. If the correlation is lost it is no longer possible to find a new coordinate system which is true for all pixels. Thus, the calculated principal components are false and therefore, the phase-step positions are not valid. This leads to artifacts which can most obviously be seen in figure 6.12 A and E. The mistakes calculating the differential phase-contrast image (figure 6.12 C and D) without a high pixel correlation are not as serious. The tiles with large differences in attenuation capacity show slight Moiré artifacts but the object information is still visible. Thus, missing

correlation leads to severe errors in offset and amplitude of the fitted sine. The phase of the sine is not affected as much as the other parameters.
Detuning the interferometer the frequency of the superimposed Moiré pattern increases. Thus, it is better detectable even if the objects causes edges in the attenuation. It has been shown that the sensitivity is not lowered too much by detuning the interferometer. Hence, it is possible to reconstruct artifact free images of object with large differences in attenuation with the help of the PCA minimization algorithm. Consequently, it is possible to remove artifacts which are caused by imprecise phase-step positions by using the PCA minimization algorithm and to avoid artifacts which are caused by edges in attenuation by misaligning the interferometer a bit. Thus, it is possible to remove all artifact caused by imprecise phase-step positions with the help of the PCA minimization algorithm.

Chapter 8

Conclusion

In this thesis it has been shown that it is possible to handle several drifting effects which occur when transferring a phase-contrast imaging system to a conventional medical setup. Therefore, feasibility of Talbot-Lau x-ray phase-contrast imaging can be significantly improved by applying the presented algorithms.
Imaging artifacts caused by short term drifting effects and mechanical inaccuracies can be removed by applying the algorithm proposed by Vargas et al. [53, 54]. In this thesis the algorithms presented in [53, 54] are combined and applied for x-ray phase-contrast imaging. In combination with the conventional reconstruction it is possible to reconstruct nearly artifact free images. It can be shown that the Moiré pattern overlaying the structures of the object in the images can be reduced or even removed applying the so called PCA minimization algorithm. Reconstructing thick, high absorbing objects which cause large differences in attenuation in one tile it is necessary to misalign the interferometer to improve correlation. This leads to a slight reduction in visibility but all artifacts caused by the instable setup can be removed in the images and artifacts due to large differences in absorbency can be avoided. Until now, many images of an object have been taken to minimize the artifacts by averaging the images. With the help of the PCA minimization algorithm this is not necessary anymore, as the artifacts can be reduced by the algorithm. Thus, the patient is exposed to a lower dose.
Additionally, long term drifting effects can be compensated by applying the PPF algorithm which is presented in this thesis. It is possible to shorten imaging time without lowering the image quality by performing the PPF algorithm, because calibration of the setup is only necessary once a day or even just once a week. At the moment it is necessary to renew the calibration image about every 10 minutes. Thus, the PPF method is a great advantage for the feasibility of x-ray phase-contrast imaging as it is possible to use just one calibration image for a long term measurement.
Both algorithms will be interesting features with regard to the implementation of

this imaging method in non-destructive testing and clinical processes. Tiny lesions can be detected with lower dose exposure and in less time than it has been the case so far as it is not necessary any more to take the mean of several images to reduce artifacts. As it is possible to reconstruct images without knowing the phase-step positions and using only one reference image, fluoroscopy might be possible provided by faster image acquisition. Additionally, in the future the algorithms might give the opportunity to perform x-ray Talbot-Lau CT imaging. Long imaging processes during CT imaging are nor problem due to the PPF method and the mechanical distortions of the CT setup during the acquisition can be compensated by applying the PCA minimization algorithm. Thus, further important clinical applications of x-ray Talbot-Lau imaging can be realized in the future due to the presented algorithms and x-ray Talbot-Lau interferometry becomes feasible in the daily workflows.

Chapter 9

Zusammenfassung

Diese Masterarbeit befasst sich mit der Korretur von Artefakten bei der Rekonstruktion von Bildern aus der Röntgen Talbot-Lau-Interferometrie.
In dem Kapitel zu den physikalischen Grundlagen wird zunächst die Enstehung von Röntgenstrahlung erläutert. Anschließend wird die Propagation der Röntgenstrahlung durch Materie mathematisch hergeleitet und zum Abschluss des Kapitels wird die Interaktion der Röntgenstrahlung mit Materie dargestellt. Im folgenden Kapitel zu der Röntgen Talbot-Lau-Interferometrie werden der Talbot- und der Lau-Effekt erklärt und anschließend die Funktionsweise eines Talbot-Lau-Interferometers aufgezeigt. Die Bildmodalitäten der Talbot-Lau-Interferometrie werden im vierten Kapitel vorgestellt. Dabei wird sowohl auf die Entstehung der Bilder als auch auf den Nutzen eingegangen.
In den anschließenden Kapiteln werden die im Zuge dieser Masterarbeit durchgeführten Weiterentwicklungen der Bildrekonstruktion erläutert und untersucht. Die Talbot-Lau-Interferometrie ist sehr stark abhängig von äußeren Einflüssen wie beispielsweise Temperaturschwankungen und Vibrationen. Diese führen zu starken Artefakten in den Bildern. Im Zuge dieser Arbeit sollten Möglichkeiten gefunden werden, um diese Störungen bereits bei der Rekonstruktion zu berücksichtigen und so die resultierenden Artefakte zu vermeiden. Die entwickelten Methoden werden getestet und die resultierende Verbesserung der Bildqualität wird untersucht. Dafür werden die Störeinflüsse in verschiedene drei Zeitskalen unterteilt, in die Langzeit-Effekte, die Kurzzeit-Effekte und die Ultra-Kurzzeit-Effekte.
Als erstes werden die Langzeit-Effekte betrachtet. Diese resultieren beispielsweise aus Temperaturschwankungen. In einem ersten Schritt wurde versucht, diese Art von Drift-Effekten allein durch Temperaturmessungen der verschiedenen Komponenten des Aufbaus zu beschreiben. Dies hat allerdings zu keinen brauchbaren Ergebnissen geführt. Scheinbar gibt es weitere Einflussfaktoren, die nicht quantifiziert und erkannt werden können. In einem zweiten Schritt wurden alle Langzeit-

Drift-Effekte durch die sogenannte Plane-Phase-Fit (PPF) Methode gemeinsam beschrieben. Dafür wird in die gemessene Objektphase ein Polynom gefittet, welches gemeinsam mit zeitlich konstanten Residuen, die aus einer vorherigen Kalibrationsmessung bestimmt werden, die Referenzphase beschreiben. Damit kann ein nahezu artefaktfreies differentielles Phasenbild rekonstruiert werden. Außerdem kann der Aufnahmeprozess beschleunigt werden, da es nicht mehr nötig ist, das Referenzphasenbild in kurzen Zeitabständen zu erneuern. Die Residuen, die durch Messung einer Kalibrationsaufnahme bestimmt werden, sind über eine längere Zeitdauer gültig.
Zweitens werden in dieser Arbeit Kurzzeit-Effekte, wie Vibrationen und Verformungen des Aufbaus untersucht. Die Bilder werden mit der sogenannten Phase-Stepping Methode aufgenommen. Dabei werden für ein Bild mehrere Aufnahmen bei verschiedenen Gitterpositionen gemacht und so das Interferenzmuster des Aufbaus abgetastet. Für die Rekonstruktion ist es dabei notwendig, die exakten Gitterpositionen für jede Aufnahme sehr präzise zu kennen. Dafür wird normalerweise das Gitter mit Hilfe eines Motors in äquidistanten Schritten bewegt. Allerdings kann es sein, dass die Schritte auf Grund der Ungenauigkeit des Motors oder wegen äußerer Einflüsse nicht exakt äquidistant sind. Dies führt zu Moiré-Mustern in den rekonstruierten Bildern. Im Zuge dieser Arbeit wurde ein Algorithmus aus der Optik, der bereits für die Rekonstruktion von Phasenbildern in die interferometrische Röntgenbildgeung übertragen wurde, erweitert und für alle drei Bildmodalitäten angepasst und angewendet. Er wird als PCA-minimization Algorithmus bezeichnet. Damit können die Moiré Artefakte in den Bildern nahezu komplett entfernt werden. Auch wird es mit diesem Algorithmus möglich, „Live“-Bildgebungen durchzuführen. In einem weiteren Schritt wird der PCA-minimization Algorithmus auch für Objekte mit großen Unterschieden in der Absorption evaluiert. Auch hier ist eine nahzu artefaktfreie Rekonstruktion möglich. Allerdings muss hierfür das Interferometer während des Aufnahmeprozesses leicht dejustiert sein, um ein möglichst regelmäßiges, überlagertes Moiré-Muster zu erhalten. Dieses Vorgehen wird in der vorliegenden Arbeit untersucht und quantifiziert.
Der dritte Drift-Effekt findet auf sehr kurzen Zeitskalen statt. Dabei führen Vibrationen während der Aufnahme eines einzelnen Phase-Steps zu Artefakten im Bild. Zur Korrektur dieser Artefakte wurden im Zusammenhang mit dieser Masterarbeit keine weiteren Untersuchungen vorgenommen.
In dieser Arbeit wurde somit gezeigt, dass unterschiedlich verursachte Artefakte mit angepassten Rekonstruktionsalgorithmen vermindert oder sogar komplett entfernt werden können. Dies ist ein großer Vorteil für die Anwendbarkeit der Röntgen Talbot-Lau-Interferometrie in der Medizin und in der zerstörungsfreien Materialprüfung. Die Bildqualität kann stark verbessert werden und die Aufnahmezeiten reduziert werden. Durch die verbesserte Bildqualität ist es zudem möglich, die

Dosis zu verringern und die Anwendbarkeit in konventionellen medizinischen Bildgebungsprozessen, wie CT-Bildgebung und „Live“-Bildgebung zu ermöglichen.

Bibliography

[1] *Australian Government - Australian Radiation Protection and Nuclear Safety Agency, Radiation Protection*. – http://www.arpansa.gov.au/radiationprotection/basics/xrays.cfm, 10.02.2016

[2] *EMF RF Electric Field Radiation Sound Safety Levels: PART 2*. – http://www.scantech7.com/wp-content/uploads/2015/01/EMF-Spectrum-by-ScanTech-www.scantech7.com$_$.jpg, 09.02.2016

[3] *Entdecken und Verstehen*. – http://www.ph2.physik.uni-goettingen.de/Entdecken_und_Verstehen2.php, 05.02.2016

[4] *N*. – http://www.nuclear-power.net/nuclear-power/reactor-physics/interaction-radiation-matter/interaction-gamma-radiation-matter/#prettyPhoto, 06.04.2016

[5] *Northern Arizona University - Electron Microprobe Laboratory*. – http://nau.edu/cefns/labs/electron-microprobe/glg-510-class-notes/signals/, 09.02.2016

[6] *The use of infrared*. – http://elte.prompt.hu/sites/default/files/tananyagok/InfraredAstronomy/ch01s05.html, 09.02.2016

[7] *Spektrum Akademischer Verlag, Lexikon der Physik, Bremsstrahlung*. 1998. – http://www.spektrum.de/lexikon/physik/bremsstrahlung/1974, 09.02.2016

[8] ACKERMANN, L. : *Entwicklung eines Phantoms für die interferometrische Röntgenbildgebung*, Friedrich-Alexander Universität Erlangen-Nürnberg, Bachelorarbeit der Physik, 2015

[9] ANTON, G. ; BAYER, F. ; BECKMANN, M. W. ; DURST, J. ; FASCHING, P. A. ; HAAS, W. ; HERTMANN, A. ; MICHEL, T. : Grating based darkfield imaging of human breast tissue. In: *Zeitschrift für medizinische Physik* 23 (2013), Nr. 3, S. 228–235

[10] BARTELT, H. ; JAHNS, J. : Interferometry based on the Lau effect. In: *Optics Communications* 30 (1979), Nr. 3, S. 268–274

[11] BECH, M. ; TAPFER, A. ; VELROYEN, A. ; YAROSHENKO, A. ; PAUWELS, B. ; HOSTENS, J. ; BRUYNDONCKX, P. ; SASOV, A. ; PFEIFFER, F. : In-vivo dark-field and phase-contrast imaging. In: *Scientific Reports* 3 (2013), Nr. 3209

[12] BERRY, M. V. ; KLEIN, S. : Integer, fractional and fractal Talbot effects. In: *Journal of modern optics* 43 (1996), Nr. 10, S. 2139–2164

[13] BORN, M. ; WOLF, E. : *Principles of optics*. Cambridge University Press, 1999. – ISBN 978–0–521–64222–4

[14] BUSHBERG, J. T. ; SEIBERT, J. A. ; LEIDHOLDT, E. M. ; BOONE, J. M.: *The essential physics of medical imaging*. Williams and Wilkins, 1994. – ISBN 0–683–01140–5

[15] CASE, W. B. ; TOMANDL, M. ; DEACHAPUNYA, S. ; ARNDT, M. : Realization of optical carpets in the Talbot and Talbot-Lau configurations. In: *Optics Express* 17 (2009), Nr. 23, 20966-20974. http://dx.doi.org/10.1364/OE.17.020966. – DOI 10.1364/OE.17.020966

[16] CASTA, R. ; CHAMPEAUX, J.-P. ; SENCE, M. ; MORETTO-CAPELLE, P. ; CARAFELLI, P. : Nanop: An x-ray to gold nanoparticle electron and photon emission software. In: *Materials Research Express* 2 (2015), Nr. 8, 085002. http://stacks.iop.org/2053-1591/2/i=8/a=085002

[17] CATTIN, P. : *University of Basel - Imaging Modalities: X-ray, CT - Biomedical Image Analysis*. 2015. – https://miac.unibas.ch/BIA/08-Xray-media/figs/Characteristic_Spectrum.png, 09.02.2016

[18] CATTIN, P. : *University of Basel - Imaging Modalities: X-ray, CT - Biomedical Image Analysis*. 2015. – https://miac.unibas.ch/BIA/08-Xray-media/figs/Bremsstrahlung_Spectrum.png, 09.02.2016

[19] CLAUSER, J. ; REINSCH, M. : New theoretical and experimental results in fresnel optics with applications to matter-wave and X-ray interferometry. In: *Applied Physics B Photophysics and Laser Chemistry* 54 (1992), Nr. 5, S. 380–395

[20] ENGELHARDT, M. ; KOTTLER, C. ; BUNK, O. ; DAVID, C. ; SCHROER, C. ; BAUMANN, J. ; SCHUSTER, M. ; PFEIFFER, F. : The fractional Talbot effect in differential x-ray phase-contrast imaging for extended and polychromatic x-ray sources. In: *Journal of Microscopy* 232 (2008), Nr. 1, S. 145 – 157

[21] EWEN, K. (Hrsg.): *Moderne Bildgebung - Physik, Gerätetechnik, Bildbearbeitung und -kommunikation, Strahlenschutz, Qualitätskontrolle*. Georg Thieme Verlag Stuttgart, New York, 1998. – ISBN 3–13–108861–3

[22] FINKLER, A. : *Phasenrekonstruktion ohne Kenntnis der Abtastpositionen des Talbot-Lau-Gitterinterferometers*, Friedrich-Alexander Universität Erlangen-Nürnberg, Diplomarbeit, 2015

[23] FITZGERALD, R. : Phase-sensitive x-ray imaging. In: *Physics Today* 53 (2000), Nr. 7, S. 23–26

[24] GRANDL, S. ; SCHERER, K. ; SZTROKAY-GAUL, A. ; BIRNBACHER, L. ; WILLER, K. ; CHABIOR, M. ; HERZEN, J. ; MAYR, D. ; AUWETER, S. D. ; PFEIFFER, F. ; BAMBERG, F. ; HELLERHOFF, K. : Improved visualization of breast cancer features in multifocal carciboma using phase-contrast and dark-field mammography: an ex vivo study. In: *European Radiology* 25 (2015), Nr. 2, S. 3659–3668. http://dx.doi.org/10.1007/s00330-015-3773-5. – DOI 10.1007/s00330–015–3773–5

[25] GRIFFITHS, D. J.: *Elektrodynamik*. Pearson Studium, 2011. – ISBN 978–3–86894–057–2

[26] HAUKE, C. : *Aufbau und Charakterisierung eines Hochenergie-Interferometers für die gitterbasierte Phasenkontrast-Röntgenbildgebung*, Friedrich-Alexander Universität Erlangen-Nürnberg, Masterarbeit der Physik, 2015

[27] HECHT, E. : *Optik*. de Gruyter, 2014. – ISBN 978–3–11–034796–8

[28] JAHNS, J. ; LOHMANN, A. : The Lau effect (a diffraction experiment with incoherent illumination). In: *Optics Communications* 28 (1979), Nr. 3, S. 263–267

[29] KOEHLER, T. ; DAERR, H. ; MARTENS, G. ; KUHN, N. ; LÖSCHER, S. ; STEVENDAAL, U. van ; ROESSL, E. : Slit-scanning differential x-ray phase-contrast mammography: Proof-of-concept experimental studies. In: *Medical Physics* 42 (2015), Nr. 4, S. 1959

[30] KOPITZKI, K. ; HERZOG, P. : *Einführung in die Festkörperphysik*. Teubner, 2007. – ISBN 978–3–8351–0144–9

[31] KRIEGER, H. : *Grundlagen der Strahlungsphysik und des Strahlenschutzes*. Vieweg und Teubner, 2009. – ISBN 978–3–8348–0801–1

[32] LAU, E. : Beugungserscheinungen an Doppelrastern. In: *Annalen der Physik* 437 (1948), Nr. 7-8, S. 417–423

[33] LI, K. ; GE, Y. ; GARRETT, J. ; BEVINS, N. ; ZAMBELLI, J. ; CHEN, G.-H. : Grating-based phase contrast tomosynthesis imaging: Proof-of-concept experimental studies. In: *Medical Physics* 41 (2014), Nr. 011903

[34] LOHMANN, A. ; SILVA, D. : An interferometer based on the Talbot effect. In: *Philosophical Magazine Series 3* 2 (1971), Nr. 9, S. 413–415

[35] LOHMANN, A. ; THOMAS, J. : Making an array illuminator based on the Talbot effect. In: *Applied Optics* 29 (1990), Nr. 29, S. 4337–4340

[36] LYNCH, S. K. ; PAI, V. ; AUXIER, J. ; STEIN, A. F. ; BENNETT, E. E. ; KEMBLE, C. K. ; XIAO, X. ; LEE, W.-K. ; MORGAN, N. Y. ; WEN, H. H.: Interpretation of dark-field contrast and particle-size selectivity in grating interferometers. In: *Applied Optics* 50 (2011), Nr. 50, S. 4310–4319

[37] MESCHEDE, D. : *Optik, Licht und Laser*. Teubner, 2008. – ISBN 978–3–8351–0143–2

[38] MICHEL, T. ; RIEGER, J. ; ANTON, G. ; BAYER, F. ; BECKMANN, M. W. ; DURST, J. ; FASCHING, P. A. ; HAAS, W. ; HARTMANN, A. ; PELZER, G. ; RADICKE, M. : On a dark-field signal generated by micrometer-sized calcifications in phase-contrast mammography. In: *Physics in Medicine and Biology* 58 (2013), S. 2713–2732

[39] MOMOSE, A. ; TAKEDA, T. ; ITAI, Y. ; HIRANO, K. : Phase-contrast X-ray computed tomography for observing biological soft tissues. In: *Nature Medicine* 2 (1996), Nr. 4, S. 473–475

[40] MOMOSE, A. ; TAKEDA, T. ; YONEYAMA, A. ; KOYAMA, I. ; ITAI, Y. : Phase-contrast x-ray imaging using an x-ray interferometer for biological imaging. In: *Analytical Sciences* 17 (2001), S. 527–530

[41] MOMOSE, A. ; YASHIRO, W. ; TAKEDA, Y. : Sensitivity of X-ray Phase Imaging Based on Talbot Interferometry. In: *Japanese Journal of Applied Physics* 47 (2008), Nr. 10, S. 8077–8080

[42] PATORSKI, K. : Incoherent Superposition of Multiple Self-imaging Lau Effect and Moire Fringe Explanation. In: *Optica Acta: International Journal of Optics* 30 (1983), Nr. 6, S. 745–758

[43] PELZER, G. ; RIEGER, J. ; HAUKE, C. ; HORN, F. ; MICHEL, T. ; SEIFERT, M. ; ANTON, G. : Reconstruction method for grating-based x-ray phase-contrast images without knowledge of the grating positions. In: *Journal of Instrumentation* 10 (2015), Nr. 12, S. P12017

[44] PFEIFFER, F. ; BECH, M. ; BUNK, O. ; KRAFT, P. ; EIKENBERRY, E. ; BRÖNNIMANN, C. ; GRÜNZWEIG, C. ; DAVID, C. : Hard-X-ray dark-field imaging using a grating interferometer. In: *Nature Materials* 7 (2008), Nr. 2, S. 134–137

[45] PFEIFFER, F. ; WEITKAMP, T. ; BUNK, O. ; DAVID, C. : Phase retrieval and differential phase-contrast imaging with low-brilliance X-ray sources. In: *Nature Physics* 2 (2006), Nr. 4, S. 258–261

[46] *Kapitel* Generalized Path Integral Technique: Nanoparticles Incident on a Slit Grating, Matter Wave Interference. In: SBITNEV, V. I.: *Advances in Quantum Mechanics*. INTECH. 2013. – ISBN 978–953–51–1089–7, S. 183–211. – http://www.intechopen.com/books/advances-in-quantum-mechanics/generalized-path-integral-technique-nanoparticles-incident-on-a-slit-grating-matter-wave-interferenc, 11.02.2016

[47] SEIBERT, J. A. ; BOONE, J. M.: X-Ray Imaging Physics for Nuclear Medicine Technologists. Part 2: X-Ray Interactions and Image Formation. In: *Journal of Nuclear Medicine Technology* 33 (2005), Nr. 1, S. 3–18

[48] STAMPANONI, M. ; WANG, Z. ; THÜRING, T. ; DAVID, C. ; ROESSEL, E. ; TRIPPEL, M. ; KUBIK-HUCH, R. A. ; SINGER, G. ; HOHL, M. K. ; HAUSER, N. : The First Analysis and Clinical Evaluation of Native Breast Tissue Using Differential Phase-Contrast Mammography. In: *Investigative Radiology* 46 (2011), Nr. 12, S. 801–806

[49] SULESKI, T. J.: Generation of Lohmann images from binary-phase Talbot array illuminators. In: *Applied optics* 36 (1997), Nr. 20, S. 4686–4691

[50] TALBOT, H. : LXXVI. Facts relating to optical science. No. IV. In: *Optics Communications* 9 (1836), Nr. 56, S. 401–407

[51] TAPFER, A. ; BECH, M. ; VELROYEN, A. ; MEISER, J. ; MOHR, J. ; WALTER, M. ; SCHULZ, J. ; PAUWELS, B. ; BRUYNDONCKX, P. ; LIU, X. ; SASOV, A. ; PFEIFFER, F. : Experimental results from a preclinical X-ray phase-contrast CT scanner. In: *Medical Physics* 109 (2012), Nr. 39, S. 15691–15696

[52] TAVASSOLY, M. T. ; SAMAVATI, K. : Formulation of the moire fringes formed by superimposing linear gratings with slowly varying parameters. In: *Applied Optics* 53 (2014), Nr. 28, S. 6612–6618

[53] VARGAS, J. ; QUIROGA, J. A. ; BELENGUER, T. : Analysis of the principal component algorithm in phase-shifting interferometry. In: *Optics Letters* 36 (2011), Nr. 12, S. 2215 – 2217

[54] VARGAS, J. ; SORZANO, C. ; ESTRADA, J. ; CARAZO, J. : Generalization of the Principal Component Analysis algorithm for interferometry. In: *Optics Communications* 286 (2013), S. 130–134

[55] WEBER, T. : *Untersuchung zur gitterbasierten Phasenkontrast-Röntgenbildgebung in polychromatischen Strahlungsfeldern*, Friedrich-Alexander-Universität Erlangen-Nürnberg, Diss., 2013

[56] WEITKAMP, T. ; DIAZ, A. ; DAVID, C. ; PFEIFFER, F. ; STAMPANONI, M. ; CLOETENS, P. ; ZIEGLER, E. : X-ray phase imaging with a grating interferometer. In: *Optics Express* 13 (2005), Nr. 16, S. 6296–6304

[57] YASHIRO, W. ; TERUI, Y. ; KAWABATA, K. ; MOMOSE, A. : On the origin of visibility contrast in x-ray Talbot interferometry. In: *Optics Express* 18 (2010), Nr. 16, S. 16890–16901

[58] YASHIRO, W. ; MOMOSE, A. : Effects of unresolvable edges in grating-based X-ray differential phase imaging. In: *Optics Express* 23 (2015), Nr. 7, 9233-9251. http://dx.doi.org/10.1364/OE.23.009233. – DOI 10.1364/OE.23.009233

[59] YASHIRO, W. ; VAGOVIC, P. ; MOMOSE, A. : Effect of beam hardening on a visibility-contrast image obtained by X-ray grating interferometry. In: *Optics Express* 23 (2015), Nr. 18, 23462-23471. http://dx.doi.org/10.1364/OE.23.023462. – DOI 10.1364/OE.23.023462

[60] ZANG, A. : *Über die Erkennbarkeit fein verteilten Mikrokalks in der interferometrischen Mammographie*, Friedrich-Alexander Universität Erlangen-Nürnberg, Masterarbeit der Physik, 2013

[61] ZERNIKE, F. : Phase contrast, a new method for the microscopic observation of transparent objects. In: *Physica* 9 (1942), Nr. 7, S. 686–698

Acknowledgments

First of all I would like to thank Prof. Dr. Gisela Anton for giving me the opportunity to work on this very interesting subject and for her great support.
Thank you very much to Florian Horn for the great supervision and for the helpful comments and ideas during the whole year of my work.
Lisa Ackermann, Cairatu Indjai, Theresa Palm and Christian Hauke, thank you for your professional help, advises and discussions and for the relaxing breaks.
Thank you to all my room mates during the year and to the whole MedPhys group for the relaxing and friendly atmosphere.
Big thanks to Georg Pelzer and Jens Rieger for helping me with technical questions and for the helpful support writing and correcting the paper.
Last but not least I would like to thank my whole family. I can always count on you and you always support me. Thank you!

Erklärung

Hiermit bestätige ich, dass ich diese Arbeit selbstständig und nur unter Verwendung der angegebenen Hilfsmittel angefertigt habe.

Erlangen, 25. Mai 2016

Maria Seifert